MODELING OF COUPLED BEHAVIOR OF MULTIFUNCTIONAL COMPOSITE STRUCTURES FOR ENERGY STORAGE

A THESIS SUBMITTED TO
THE GRADUATE SCHOOL OF NATURAL AND APPLIED SCIENCES
OF
MIDDLE EAST TECHNICAL UNIVERSITY

BY

İMREN UYAR YAZICI

IN PARTIAL FULFILLMENT OF THE REQUIREMENTS
FOR
THE DEGREE OF DOCTOR OF PHILOSOPHY
IN
AEROSPACE ENGINEERING

JULY 2024

Approval of the thesis:

MODELING OF COUPLED BEHAVIOR OF MULTIFUNCTIONAL COMPOSITE STRUCTURES FOR ENERGY STORAGE

submitted by **İMREN UYAR YAZICI** in partial fulfillment of the requirements for the degree of **Doctor of Philosophy** i**n Aerospace Engineering, Middle East Technical University** by,

Prof. Dr. Naci Emre Altun
Dean, **Graduate School of Natural and Applied Sciences** _____

Prof. Dr. Serkan Özgen
Head of the Department, **Aerospace Engineering** _____

Assoc. Prof. Dr. Ercan Gürses
Supervisor, **Aerospace Engineering, METU** _____

Examining Committee Members:

Prof. Dr. Demirkan Çöker
Aerospace Engineering, METU _____

Assoc. Prof. Dr. Ercan Gürses
Aerospace Engineering, METU _____

Prof. Dr. Hüsnü Dal
Mechanical Engineering, METU _____

Assoc. Prof. Dr. Cihan Tekoğlu
Mechanical Engineering, TOBB _____

Assist. Prof. Dr. Ferit Sait
Mechanical Engineering, Çankaya Üniversitesi _____

Date: 24.07.2024

I hereby declare that all information in this document has been obtained and presented in accordance with academic rules and ethical conduct. I also declare that, as required by these rules and conduct, I have fully cited and referenced all material and results that are not original to this work.

Name Last name: Uyar Yazıcı, İmren

Signature:

ABSTRACT

MODELING OF COUPLED BEHAVIOR OF MULTIFUNCTIONAL COMPOSITE STRUCTURES FOR ENERGY STORAGE

Uyar Yazıcı, İmren
Doctor of Philosophy, Aerospace Engineering
Supervisor: Assoc. Prof. Dr. Ercan Gürses

July 2024, 135 pages

This work presents a framework for multiphysics modeling of a multifunctional composite material, structured on the microscale, with the ability to function as a battery cell and carry mechanical load. The microstructure consists of a single carbon fiber surrounded by a very thin solid electrolyte coating and embedded in a polymer matrix, a porous material containing active particles able to intercalate lithium. Therefore, the composite structure simulates the electro-chemo-elastic behavior under different electrochemical states (charging-discharging). At these states, a volume swelling caused by lithium-ion movement is observed, similar to heat expansion, where pure volume expansion is produced under thermal load.

The first step investigates the monolithically coupled finite element simulation of electro-chemo-mechanical media. After simulating the coupled behavior of the fiber region of a structural battery, the analysis is combined with the crack formation in the fiber region. Due to the high concentration gradient at the fiber surface, mechanical stresses are developed, which may lead to the initiation and growth of cracks in the fiber. Crack evolution in the structure causes a decrease in the mechanical properties of fibers and a reduction in the charging properties of the

battery by decreasing the diffusivity of lithium ions. To understand the damage mechanisms of the coupled system, a phase-field fracture model is implemented in the coupled system to model three different crack mechanisms (Central Crack, Arc Crack, and T-Crack). The stress distribution and crack growth behavior are investigated for each configuration, highlighting each crack type's unique characteristics and propagation mechanisms. The open-source finite element software FENICS [61, 62] is used for the FE procedure.

Keywords: Fracture of Composites; Structural Batteries; Electro-Chemo-Mechanical Coupling, Phase Field Approach, Multifunctional Materials

ÖZ

ENERJİ DEPOLAMA İÇİN ÇOK FONKSİYONLU KOMPOZİT YAPILARIN AKUPLE DAVRANIŞ MODELLEMESİ

Uyar Yazıcı, İmren
Doktora, Havacılık ve Uzay Mühendisliği
Tez Yöneticisi: Doç. Dr. Ercan Gürses

Temmuz 2024, 135 sayfa

Bu çalışma, mekanik yük taşımanın yanı sıra bir pil hücresi olarak işlev görebilen, mikro ölçekte yapılandırılmış çok işlevli bir kompozit malzemenin çoklu fizik modellemesi için bir çerçeve sunmaktadır. Mikroyapı, çok ince bir katı elektrolit kaplaması ile çevrili tek bir karbon lifinden oluşmakta ve lityumu enterkale edebilen aktif parçacıklar içeren gözenekli bir polimer matris içine gömülmüştür. Dolayısıyla, kompozit yapı farklı elektrokimyasal durumlar (şarj-deşarj) altında elektro-kemo-elastik davranışı taklit etmektedir. Bu durumlarda, lityum iyon hareketi nedeniyle hacimde bir şişme gözlemlenir ki bu, termal yük altında saf hacim genleşmesinin üretildiği ısı genleşmesine çok benzer.

İlk adım, elektrokimyasal ve elastik ortamların birleştirilmiş sonlu eleman simülasyonunu araştırmaya odaklanmaktadır. Yapısal bir bataryanın fiber bölgesinin birleştirilmiş davranışını simüle ettikten sonra, analiz lif bölgesindeki çatlak oluşumu ile birleştirilmiştir. Fiber yüzeyinde yüksek konsantrasyon gradyanı nedeniyle mekanik gerilmeler gelişir ve bu da fiberde çatlakların başlamasına ve büyümesine yol açabilir. Yapıdaki çatlak gelişimi, fiberlerin mekanik özelliklerinde azalmaya ve lityum iyonlarının difüzyonunu azaltarak bataryanın şarj özelliklerinde düşüşe neden olur. Bağlı sistemin hasar mekanizmalarını anlamak için, üç farklı çatlak mekanizmasını (Merkezi Çatlak, Yay Çatlağı ve T-

Çatlağı) modellemek amacıyla bağlı sisteme bir faz alanı kırılma modeli uygulanmıştır. Her yapılandırma için gerilme dağılımı ve çatlak büyüme davranışı incelenmiş, her bir çatlak tipinin kendine özgü özellikleri ve yayılma mekanizmaları vurgulanmıştır.

Sonlu eleman prosedürü için açık kaynaklı bir sonlu eleman yazılımı olan FENICS [61, 62] kullanılmıştır.

Anahtar Kelimeler: Kompozitlerin Kırılması, Yapısal Bataryalar, Elektrokimyasal-Mekanik Bağlantı, Faz Alanı Yaklaşımı, Çok Fonksiyonlu Malzemeler

To my loving Mom and Dad…

ACKNOWLEDGMENTS

First and foremost, I would like to express my sincere gratitude to my supervisor, Assoc. Prof. Dr. Ercan Gürses, for his continuous support of my Ph.D. study and research, his guidance, patience, motivation, advice, criticism, encouragement, and insight throughout the research. I could not have imagined having a better advisor and mentor for my Ph.D. study.

Besides my advisor, I would like to thank the thesis monitoring committee: Prof. Dr. Hüsnü Dal for his immense knowledge and willingness to share his expertise, and Prof. Dr. Demirkan Çöker for always being supportive and providing visionary guidance. I feel incredibly fortunate to have had the opportunity to continue this journey with such an exceptional committee.

I would also like to sincerely thank the remaining members of my thesis committee, Assoc. Prof. Dr. Cihan Tekoğlu and Assist. Prof. Dr. Ferit Sait, for their support, insightful feedback, and challenging questions, all of which significantly contributed to the depth and rigor of my work.

I would like to thank ASELSAN company for their unwavering support of my academic progress. They granted me the necessary time off, encouraged the continuation of my academic journey alongside my professional life, and always respected and valued this balance.

I would also like to extend my heartfelt thanks to the METU Aerospace Engineering Department. I entered its doors as a high school graduate and am now leaving with three diplomas, an unmatched depth of knowledge, and a well-rounded personality. Over almost 18 years, I have accumulated countless memories, forged lifelong friendships, and gained invaluable experiences. The department has been more than just an academic home; it has been a place that shaped who I am today, both personally and professionally.

My sincere thanks also go to my husband, Orcan Yazıcı, for always being supportive and positive, for never letting me feel alone, and for enduring the long journey of this work with me, including all its ups and downs. I am deeply grateful for his constant encouragement and for being my rock throughout this journey.

I want to thank my genius friend Gökhan Saygın, who is always willing to help, give his best suggestions, cheer me up, and stand by me through the good times and the bad.

In particular, I am deeply grateful to each member of the METU Swimming Team, my chosen family, for making difficult times more manageable and easier to navigate. I also owe a great deal to my home mates, Sena and Görkem, my dear little brother Deniz, and my wonderful friends Günce, Miray, Selma, Cansu, and Senem Ayşe, who have been by my side and offered invaluable support throughout this journey.

Last but not least, I would like to thank my family: my parents, Münevver Uyar and İsmail Mazhar Uyar, for bringing me into this world and their unwavering support throughout my life. My father, with his never-give-up attitude and constant support, has been a pillar of strength for me. My beloved mother held my hand just as tightly on the last day of my education as she did on the first. Without her presence and encouragement, I would never have succeeded. I am incredibly fortunate to be their daughter.

.

TABLE OF CONTENTS

ABSTRACT v

ÖZ vii

ACKNOWLEDGMENTS x

TABLE OF CONTENTS xii

LIST OF TABLES xv

LIST OF FIGURES xvi

LIST OF ABBREVIATIONS xx

LIST OF SYMBOLS xxi

CHAPTERS

1 INTRODUCTION 1

1.1 Polymer Composite Materials 1

1.2 Damage Modes in Polymer Composites 4

1.3 Lithium-ion Battery 6

1.4 Structural Composite Material Battery 8

1.4.1 Laminated Battery 10

1.4.2 3D Battery 11

1.5 Distinct Regions in 3D Battery 13

1.6 Electro-Chemo-Mechanical Coupling 16

1.7 Crack Formation Due to Electrochemical Loading 17

2 MATHEMATICAL MODELING 21

2.1 Mathematical Models of Electrochemical and Mechanical Processes in the Lithium-ion Battery 21
2.2 Simplified Mathematical Modeling 23
2.2.1 Governing Equations of the Field 24
2.2.2 Free Energy and Constitutive Laws 24
2.2.3 Linear and Nonlinear Chemical Field Equations 28
2.3 Phase Field Implementation to Solution of Coupled System 32
2.4 Weak Forms and Solution Algorithms 36
3 ELECTROCHEMICAL MECHANICAL COUPLING RESULTS 43
3.1 Numerical Examples 43
3.1.1 Electrochemical-Mechanical Coupling: Example 1 43
3.1.2 Electrochemical-Mechanical Coupling: Example 2 46
4 ELECTROCHEMICAL MECHANICAL PHASE FIELD COUPLING RESULTS 53
4.1 Mechanical Phase Field Coupling: Single Edge Notched Specimen 53
4.1.1 Geometry, Boundary Conditions, and Study Parameters 54
4.1.2 Mechanical-Phase Field Coupling Results 55
4.2 Electrochemical Mechanical Phase Field Coupling: Single-Edge Notched Specimen 59
4.2.1 Geometry, Boundary Conditions, and Study Parameters 59
4.2.2 Electrochemical-Mechanical-Phase Field Coupling Results 60
4.3 Electrochemical-Mechanical-Phase Field Coupling: Crack Propagation in Circular Fiber 62
4.3.1 Circular Fiber with Central Crack 62
4.3.2 Circular Fiber with Arc Crack 78

4.3.3 Circular Fiber with T-Crack 89
5 CONCLUSION 97
REFERENCES 107
APPENDICES 117
A. CRACK TIP SPEED CALCULATIONS 117
B. CRACK PROPAGATION RESULTS 119
Center Crack Results 119
Arc Crack Results 124
T- Crack Results 129
CURRICULUM VITAE 133

LIST OF TABLES

TABLES

Table 2.1 The set of Equations with Boundary Conditions of the Coupled System31
Table 3.1 Material Parameters [34]..... 44
Table 3.2 The material parameters..... 47
Table 4.1 The material parameters used in single-edge-notched specimen. (Miehe et al. [38])..... 55
Table 4.2 The material parameters used in the center crack numerical examples.. 63
Table 4.3 The test case details and crack conditions in numerical examples. 68
Table 4.4 The maximum radial and circumferential stresses at the onset of crack propagation 69
Table 4.5 Crack branching location comparison 71
Table 4.6 The material parameters used in numerical examples. 79
Table 4.7 Maximum Crack Tip Speeds for $\rho = 0.8$ m 85
Table 4.8 The maximum radial and circumferential stresses at the onset of crack propagation 87
Table 4.9 The material parameters used in numerical examples. 90

LIST OF FIGURES

FIGURES

Figure 1.1. The damage mechanisms in an example laminate composite in order of matrix crack, delamination, and fiber fracture [10] 5
Figure 1.2. The fiber /matrix debonding example in a glass fiber composite lamina [11] 5
Figure 1.3. Schematic illustrations of the two main structural battery composite models: (a) the laminated battery and (b) the 3D battery [24]. 9
Figure 1.4. Schematic illustration of the 3D battery structural composite model [24]. 12
Figure 1.5. Schematic figure of the cross-section of the 3D battery [73] 16
Figure 1.6. Axisymmetric schematic of the cell components Carbon Fiber, Coating, and Matrix) of 3D battery [4] 16
Figure 2.1. Schematic of the 3D-battery computational domains [31] 23
Figure 2.2. A phase field approximation of the discrete discontinuities 33
Figure 2.3. Proposed solution scheme for coupled phase field algorithm..... 41
Figure 3.1. Numerical Example-1 Geometry and Boundary Condition. (Yang et al.) [34]. 44
Figure 3.2. (a) The y-displacement results of the present study on the deformed shape of the body (b) Ionic concentration distribution on the undeformed shape of the body 46
Figure 3.3. Numerical Example-2 geometry and Boundary conditions (Klinsmann et al. [35]..... 47
Figure 3.4. (a) Loading condition and concentration difference Δc (b) The highest value of the radial stress and the highest values of circumferential stress for time 49
Figure 4.1. Single-edge-notched specimen: (a) Geometry and boundary conditions (Miehe et al. [38]), (b) Mesh structure 54
Figure 4.2. The comparison of load-deflection curves with Miehe [48] results in a length scale l=0.015 mm 57

Figure 4.3. The comparison of load-deflection curves of monolithic and staggered solutions 57
Figure 4.4. The comparison of phase field variation through the crack surface and crack pattern at the final state of simulation for (a) monolithic solution and (b) staggered solution. 58
Figure 4.5. Single-edge-notched specimen geometry and boundary conditions. ... 60
Figure 4.6. The crack propagation with respect to phase field distribution on the crack surface for different time intervals 61
Figure 4.7. (a) Geometry and boundary conditions for the Li intercalation fiber with a central crack, (b) Mesh structure of fiber with a crack length $a = 0.6\,m$ ... 63
Figure 4.8. (a) Loading condition and maximum concentration difference Δc. (b) The maximum values of the radial and circumferential stress components with time. (c) Ionic concentration distribution at three different time steps: A at $t = 0.3tmax$, B at $t = 0.5tmax$, and C at $t = 1.5tmax$ 66
Figure 4.9. (a) Radial stress distribution corresponding to maximum concentration difference (point B) (b) Circumferential stress distribution corresponding to maximum concentration difference (point B) 67
Figure 4.10. Circumferential stress distribution ($\sigma\theta\theta$) for the test case B2 along y=0 (from x=0.11 (very close to crack tip) to x=1 (outer surface) for different time steps..... 71
Figure 4.11. Maximum crack tip speeds of cracks $a = 0.4$ m and $a = 0.6$ m..... 74
Figure 4.12. Phase field distributions during crack growth and propagation for the test case D2 (a=0.6 m and $c = 0.0005$ (mol/Ls) 75
Figure 4.13. Ionic concentration distributions during crack growth and propagation for the test case D2 (a=0.6 m and $c = 0.0005$ (mol/Ls) 75
Figure 4.14 Crack tip speed comparison of two different crack lengths in the same loading rate ($c = 0.0005$ (mol/Ls) 76
Figure 4.15. Maximum crack tip speed of the fiber for different phase field viscosity parameters (η) crack length for $c = 0.0007$ mol/Ls (a) $a = 0.6\,m$..... 77

Figure 4.16 Phase field distribution after crack propagates in a one-time step for $c = 0.004$ mol/Ls (a) $a = 0.2\ m$ (b) $a = 0.6\ m$ 78
Figure 4.17. (a) Geometry and boundary conditions of fiber with an arc crack, (b) Mesh structure of fiber with a crack length $\rho = 0.9\ m$ and $\theta = 19°$ 80
Figure 4.18. The maximum concentration difference compared with fiber without arc and center cracks. 81
Figure 4.19. Concentration distribution of fiber at time = 0.5 for (a) fiber without crack, (b) central crack ($r = 0.6$ m), (c) arc crack ($\rho = 0.8$ m and $\theta = 50°$) 82
Figure 4.20. (a) Radial stress distribution (b) Circumferential stress distribution corresponding to onset of crack growth ($\rho = 0.8$ m and $\theta = 45°$) 83
Figure 4.21. Phase field distributions during crack growth for the arc crack with the parameters θ= 45º, ρ=0.8 m and $c = 0.0001$ mol/Ls 84
Figure 4.22. Crack tip speed comparison of two different arc cracks for $\rho = 0.8$ m and charging rate $c = 0.0001$ mol/Ls 85
Figure 4.23. Crack tip speed comparison of three different arc cracks for $\rho = 0.8$ m and charging rate $c = 0.00008$ mol/Ls 86
Figure 4.24. Concentration distribution of fiber with an arc crack (θ= 45º m, ρ=0.8 m and $c = 0.0001$ mol/Ls) (a) before crack growth (b) after crack growth 88
Figure 4.25. (a) Geometry and boundary conditions for the Li intercalation fiber with a T-crack (b) (b) Mesh structure of fiber with a crack length $\rho = 0.9\ mm$ and $xa = 0.3$m 91
Figure 4.26. Radial stress distribution corresponding to the onset of crack growth (a) Radial Crack (b) T-crack for c=0.0005 mol/Ls. Note that the positions and sizes of the arc cracks are the same in both cases. 92
Figure 4.27. Circumferential stress distribution corresponding to the onset of crack growth (a) Radial Crack (b) T-Crack for c=0.0005 mol/Ls. Note that the positions and sizes of the arc cracks are the same in both cases. 93
Figure 4.28. Phase field distribution (a) arc crack (b) T-crack for c=0.0005 mol/Ls 93

Figure 4.29. Phase field distributions during crack growth for the T-crack with the parameters $xa = 0.25$, $\rho = 0.9$ m and for c=0.0005 mol/Ls 95

LIST OF ABBREVIATIONS

ABBREVIATIONS

CF	Carbon Fiber
SPE	Solid Polymer Electrolyte
SBE	Structural Battery Electrolyte
SEI	Solid-Electrolyte Interphase
UD	Unidirectional
CCCV	Constant Current Constant Voltage

LIST OF SYMBOLS

SYMBOLS

c	Li concentration per unit volume
$\dot{c}$	Time Rate of Change of Li Ions
$\mathbf{J}$	Flux of Li Ions
$\boldsymbol{\sigma}$	Cauchy Stress Tensor
g	Extended Gibbs Free Energy Density
u	Internal Energy Density
σ_{ij}	Stress Tensor
ε_{ij}	Strain Tensor
λ	Lamé Parameters
μ	Lamé Parameters
ε_{ii}	The Sum of Normal Strains (volumetric strain)
δ_{ij}	Kronecker Delta
K	Material's Bulk Modulus
G	Shear Modulus
$\boldsymbol{\varepsilon}^e$	Elastic Strain
$\boldsymbol{\varepsilon}$	Total Strain
$\boldsymbol{\varepsilon}^{ch}$	Chemical Strain
Ω_c	Lithium Partial Molar Volume
c_0	Reference Concentration
$u_{chemical}$	Chemical Energy Density
R	The Gas Constant
T	Temperature
μ_0	Reference Chemical Potential
μ	Chemical Potential
$\mathbf{u}$	Displacement
S	Proportional Coefficients of Chemical Potential and

	Concentration
D_0	Diffusion Coefficients of Anions and Cations
c_{max}	Maximum Ionic Concentration
σ_h	Hydrostatic Stress
$\bar{\boldsymbol{u}}_{\boldsymbol{i}}$	Prescribed Displacements
t	Tractions
$\bar{c}_0$	Concentration
$\bar{\mathbf{J}}_{\mathbf{n}}$	Surface Flux
ϕ	Phase field variable
l	length scale parameter
Γ_l	Regularized crack density functional
Ψ	Total Potential Energy
η	Viscous Term
H^+	History Variable Field
k	Numerical Parameter
Δc	Maximum Concentration Difference
E	Young's Modulus
ν	Poisson's Ratio
φ	Diffusion Coefficient
ρ	Density
j	Current Density
j_0	Exchange current density
α_a, α_c	Anodic and cathodic charge transfer coefficients
F	Faraday Constant
η	Overpotential (in Butler-Volmer Equation)
G_c	Critical Energy release rate
v	Displacement field test function
q	Phase field test function
$\hat{c}$	Concentration field test function

η	Viscosity parameter
a	Crack length
V_p	Dilatational Wave Speed
V_S	Shear Wave Speed
V_R	Rayleigh Wave Speed
c_s	Critical Wave Speed

CHAPTER 1

INTRODUCTION

This chapter presents an in-depth exploration of polymer composite materials and lithium-ion batteries. It begins by defining polymer composite materials and discussing their significance across various industries. The chapter then examines the different types of damage observed in polymer composites and their impact on structural integrity. It then discusses lithium-ion batteries, explaining their fundamental working principles. The focus shifts to structural composite material batteries, specifically laminated and 3D batteries. For 3D batteries, the chapter outlines the various regions and essential components, offering a detailed understanding of their structure. Finally, the chapter discusses the formation of cracks in structural batteries due to electrochemical loading, exploring the mechanisms behind this phenomenon and its implications. The chapter includes definitions and summaries from relevant literature to aid comprehension.

1.1 Polymer Composite Materials

The convergence of innovation and engineering in materials science creates remarkable materials with unique properties. Composites are an ideal material class that has revolutionized numerous industries. Composites are distinguished by their clever combination of a matrix material, which can be polymeric, metallic, or ceramic, with a secondary, physically separable phase strategically distributed within the matrix. This second phase reinforces, effectively enhancing the composite's strength, stiffness, and toughness.

In load-bearing applications, fiber composite materials are used extensively in laminates composed of laminae (thin sheets or layers) reinforced with continuous and oriented fibers. These advanced materials have proven their worth across various industries and applications. For instance, in the aerospace industry, composite laminates have become instrumental in constructing lightweight yet durable aircraft structures, contributing to fuel efficiency and improved performance. In automotive engineering, they fabricate lightweight, high-strength components that enhance fuel economy and safety. Furthermore, within the construction industry, these materials find their place in creating robust and long-lasting infrastructure elements like bridges and building facades, ensuring structural integrity while reducing maintenance costs. Most structural composites are composed of laminates with layers oriented in multiple directions. Multidirectional laminates refer to composite materials where the reinforcing fibers are oriented in multiple directions within the matrix. This arrangement offers improved mechanical properties in multiple axes, making them highly adaptable for applications requiring strength and stiffness in different directions. In contrast, unidirectional laminates consist of reinforcing fibers aligned primarily in a single direction within the matrix. This configuration maximizes the material's strength and stiffness in that specific direction, making unidirectional laminates ideal for applications with critical load-bearing capabilities in one primary direction.

Polymer carbon fiber composites represent a distinctive subset within the big family of composite materials. These composites are engineered by combining two primary constituents: polymer matrices and carbon fiber reinforcement. Polymer matrices typically include thermosetting materials like epoxy, vinyl ester, and unsaturated polyester, which remain liquid before curing. This liquid state facilitates effective fiber impregnation before the composite material undergoes chemical cross-linking during curing [1]. Carbon fibers, on the other hand, are solid and lightweight filaments composed predominantly of carbon atoms. When embedded within the polymer matrix, these carbon fibers lend exceptional

mechanical properties to the composite, such as high tensile strength, stiffness, and low weight.

One of the critical attributes of carbon fibers is their high anisotropy, a characteristic resulting from crystallites mainly oriented along the fiber axis, giving them exceptional stiffness and strength in the axial direction [2]. Beyond their mechanical strength, carbon fibers exhibit commendable electrical conductivity, opening doors to innovative electronics and electrical systems applications. Recent studies have also investigated their lithium intercalation properties, exploring the possibility of carbon fibers as a host material for lithium insertion [3]. This investigation can potentially revolutionize energy storage technologies and pave the way for advanced lithium-ion batteries with enhanced performance and efficiency. The remarkable properties of carbon fibers, from their superior mechanical strength to their promising role in energy storage, continue to drive advancements and inspire novel solutions referring to a wide range of industries [5].

This subsection aims to describe the properties of the constituents in a structural composite to illustrate what might be affected by introducing battery function. In general, the elastic behavior of composite materials is described through the elastic properties of their constituents, which include the modulus of elasticity, shear modulus, and Poisson's ratio. These properties define how the composite responds to mechanical loading and deformation, considering the behavior of both the matrix and the reinforcing fibers [4].

Performance parameters for a unidirectional isotropic composite plate typically include tensile strength, compressive strength, shear strength, modulus of elasticity, and Poisson's ratio. These parameters describe how strong a material is and its ability to handle different types of physical forces which is important for design and engineering applications.

1.2 Damage Modes in Polymer Composites

The primarily used composite structures are multidirectional laminates composed of unidirectional piles with varying fiber orientations relative to the specimen axis. Depending on the application, laminated composites can be susceptible to various damage mechanisms. Common damage mechanisms in laminated composites are listed below.

Delamination: Delamination separates or splits the layers within a laminate (Figure 1.1). It often occurs due to shear or tensile stresses, impact, or thermal cycling. Delamination weakens the composite's structural integrity and can lead to catastrophic failure [6].

Fiber Breakage: The fibers provide strength in composite materials. Fiber breakage can occur under excessive tensile or compressive loads (Figure 1.1), leading to a loss of load-carrying capacity [7].

Matrix Cracking: The matrix material in laminated composites can develop cracks, especially under tensile or compressive loads (Figure 1.1). These cracks may compromise the composite's load-carrying capacity and stiffness [8].

Fiber-Matrix Debonding: Weak adhesion between the fibers and the matrix can result in fiber-matrix debonding (Figure 1.2). This damage mechanism can reduce the load transfer between the fibers and the matrix, reducing strength and stiffness [9].

Microcracking: Microcracking occurs at the microscale within the layers of laminated composite materials. These cracks can develop due to various factors, including cyclic loading, thermal stresses, or defects within the material [12]. Unlike more extensive, more visible cracks, microcracks are not readily detectable without specialized equipment.

What makes microcracking significant is microcracks develop slowly and quietly within the material, and their effects on the composite's strength and integrity may

not be immediately apparent. However, over time, these microcracks can lead to significant damage and compromise the composite's overall performance. Microcracks within the composite material serve as stress concentrators, significantly amplifying the effects of external loads and environmental factors [13]. They diminish the material's capacity to withstand stress, posing a substantial risk of structural failure if these microcracks are not effectively addressed and managed. Understanding and mitigating these damage mechanisms is crucial for ensuring laminated composite structures' long-term reliability and performance, especially in applications with critical strength, stiffness, and durability.

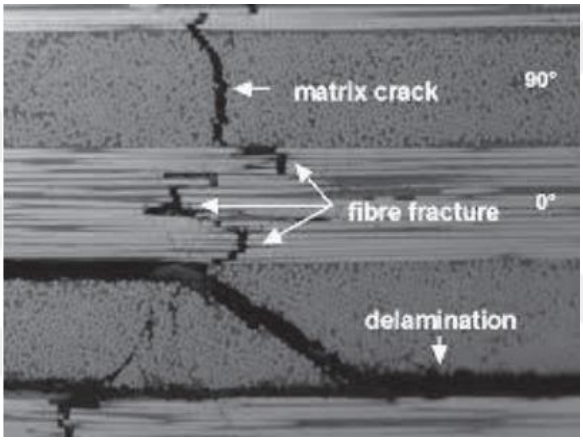


Figure 1.1. The damage mechanisms in an example laminate composite in order of matrix crack, delamination, and fiber fracture [10]

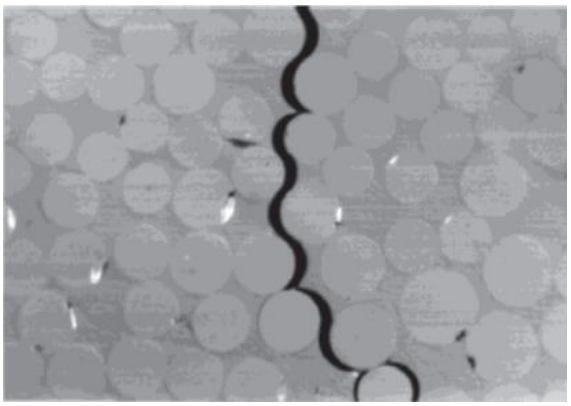


Figure 1.2. The fiber /matrix debonding example in a glass fiber composite lamina [11]

1.3 Lithium-ion Battery

The lithium-ion battery is a type of rechargeable battery that is commonly used. These clever power sources utilize the principles of oxidation-reduction (redox) reactions to convert chemical energy into a readily usable electrical form effectively. The fundamental structure of a conventional lithium-ion battery is a testament to its elegant simplicity. It comprises two essential electrodes: the negative and positive terminals, separated by a specialized separator impregnated with a liquid electrolyte solution. These electrodes are designed and characterized by their porous nature and detailed composition. Many active electrode material particles reside within their porous frameworks, varying in size from the nanoscale to micrometers. These active particles, known as intercalating materials, are blended with conductive additives and binder materials to optimize performance [1]. The intercalation process, involving the insertion of ions between the layers of a material's crystal lattice, plays a pivotal role in the functioning of lithium-ion batteries, facilitating efficient energy storage.

Redox, short for oxidation-reduction, reactions represent a fundamental chemical process that underlies the conversion of chemical energy into electrical energy. These reactions involve the transfer of electrons between chemical species, leading to changes in their oxidation states.

During discharge, the negative electrode (typically made of graphite) undergoes oxidation, releasing electrons and lithium ions into the electrolyte. Meanwhile, the positive electrode (e.g., lithium iron phosphate) undergoes reduction, accepting electrons and lithium ions from the electrolyte. The movement of these electrons through an external circuit to balance the charge difference between the two electrodes generates an electrical current that can power devices or recharge other batteries. This process is reversed when the battery is charged and lithium ions are transferred to the negative electrode. An example of redox reactions is shown below,

At the negative electrode, oxidation

$$LiC_6 \underset{charge}{\overset{discharge}{\rightleftharpoons}} Li_{1-x}C_6 + xLi^+ + xe^- \quad (1\text{-}1)$$

and the positive electrode, reduction

$$Li_{1-x}FePO_4 + xLi^+ + xe^- \underset{charge}{\overset{discharge}{\rightleftharpoons}} LiFePO_4 \quad (1\text{-}2)$$

The electrolyte's significance in a battery lies in its ability to facilitate the movement of ions between the electrodes. This ion transfer process is paramount to the battery's overall performance and efficiency, as it directly influences the speed at which electrical energy can be stored and released. From an electrochemical perspective, a battery with shorter ion percolation distances is highly desirable, as it allows for more rapid ion movement, ultimately enhancing the battery's responsiveness and effectiveness [17].

When examining the variety of electrolyte options, it becomes evident that four primary types exist, each with unique characteristics and applications. First, organic liquids are commonly used electrolyte types, offering good conductivity and versatility in various battery chemistries [14]. Second, ionic liquids, known for their low volatility and expansive electrochemical windows, have gained attention as potential candidates for advanced battery technologies [15]. Third, solid polymer electrolytes have emerged as a promising alternative, featuring enhanced safety, reduced leakage risk, and compatibility with solid-state battery designs [16]. Lastly, gel electrolytes, with their semi-solid consistency, find applications in specific battery configurations, compromising liquid and solid electrolyte properties [1]. This variety of electrolyte options underscores the importance of selecting the most suitable type for a given battery application, as it can significantly impact the battery's overall performance, safety, and longevity.

Galvanostatic and potentiostatic charging are commonly used to describe a battery's charging state. In galvanostatic charging, a constant current is maintained as the electrochemical cell charges or discharges. This method is widely used to measure battery capacity and control charge/discharge rates and cycle life by applying a fixed current to the cell and monitoring the voltage over time [75].

On the other hand, potentiostatic charging, the working electrode's potential (voltage) is held constant over time. The electrode potential is set to a fixed value, and the current is monitored as the system responds. This method is used to study the behavior of batteries under constant voltage conditions, often in the final stages of charging [74].

1.4 Structural Composite Material Battery

The concept of a structural composite battery represents an innovative breakthrough in materials science and energy storage technology. It refers to a composite material with a dual capability: it can store electrical energy, essentially functioning as a battery, while simultaneously providing crucial mechanical integrity within a structural system. This multifunctional material is an energy storage solution and a load-bearing component, pioneering a new era of efficient and integrated design.

To qualify as a successful energy storage structure, a structural composite battery must meet two fundamental criteria, as outlined by Pereira and colleagues in their research [52]. Firstly, the embedded energy cell within the composite must retain its ability to charge and discharge electrical energy, maintaining its prior functionality and doing so even when subjected to mechanical loading. This means that the energy storage capabilities remain intact despite the structural demands placed upon the material. Secondly, the energy storage structure should exhibit no degradation in its mechanical performance. In other words, its load-bearing

capacity and structural integrity should remain unaffected, ensuring the safety and reliability of the overall system.

Previous literature has introduced two distinctive architectural approaches to structural battery composites. The first of these, known as the laminated battery architecture, was initially proposed by Wong and colleagues [72] and later demonstrated by Carlson in 2013 [21]. The laminated battery design has individual layers that serve different purposes, such as an electrode, separator, and current collector. This makes it a flexible and adaptable concept in architecture.

The second architectural innovation, which emerged more recently and was developed by Carlstedt, Marklund, and Asp in 2019 [23], is often referred to as the 3D battery or Micro battery architecture. In this cutting-edge design, carbon fibers assume a central role. Each carbon fiber is coated with a thin polymer electrolyte layer, transforming them into autonomous battery cells within the composite lamina. This 3D battery design is a significant change in the field because it uses the unique qualities of carbon fibers to store energy in the detailed structural material. These two architectural approaches are promising for combining energy storage and strong materials. They show how structural battery composites are getting better and more creative in finding ways to use energy effectively. The latest and most advanced models of the two battery designs are depicted in Figure 1.3.

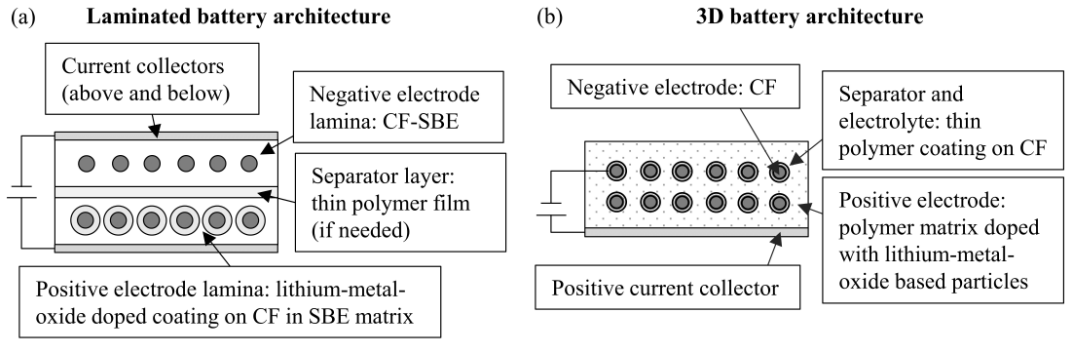


Figure 1.3. Schematic illustrations of the two main structural battery composite models: (a) the laminated battery and (b) the 3D battery [24].

1.4.1 Laminated Battery

Figure 1.3 (a) depicts one of the conceptual examples of a laminated battery [24], illustrating the structural arrangement within this innovative energy storage device. In this schematic, one of the laminas takes on the role of the negative electrode within the battery cell. This lamina comprises a structural battery electrolyte (SBE) reinforced with carbon fibers (CF). On the other hand, the other specific lamina, corresponding to the positive electrode, also consists of a Solid Battery Electrolyte (SBE). Still, it is reinforced with carbon fibers coated with lithium metal oxide-based particles, such as $LiFePO_4$. These particles within the coating and the carbon fibers in the negative electrode lamina are the active electrode materials responsible for storing and releasing energy within the battery cell.

A layer of separator between the two laminae might be required to prevent any potential short-circuiting caused by the contact between the positive and negative electrodes [53]. The separator layer needs to have two critical features. It should be electrically insulating, i.e., it should not conduct electrons, but at the same time, it should allow the ions to move between the electrodes. Furthermore, it should be thin to minimize ohmic losses (resistance to the flow of electricity) and yet be rigid enough to prevent penetration and enable the transfer of mechanical loads. Suppose the SBE material is strong and evenly distributed. In that case, it may not be necessary to have a separator layer to keep the active electrode materials separate and prevent them from contacting [24]. This complex arrangement of materials and layers is essential for the proper functioning of the battery cell.

As explored in previous research [17], structural batteries present a unique approach to integrating energy storage within structural components. However, it comes with distinct advantages and disadvantages:

Advantages:

The concept of laminated structural batteries offers the potential for seamless integration of energy storage into structural components, which can reduce overall device weight and volume.

Challenges:

The performance of structural batteries has been hindered by the low ionic conductivity of the structural battery electrolyte (SBE). This limitation is primarily attributed to the considerable distances between the negative and positive terminals, which hinder ion movement and consequently affect the charging and discharging capabilities of the battery [17]. Successful implementation of this concept requires addressing substantial technical difficulties related to ionic conductivity and overall battery efficiency that need to be overcome, necessitating extensive research and development efforts. The observed poor performance of structural batteries raises concerns about their efficiency in meeting the energy storage demands of various applications.

1.4.2 3D Battery

Within the innovative 3D battery design concept, as illustrated in Figure 1.3 (b), every individual fiber assumes the role of an independent battery cell. In this arrangement, carbon fibers have a dual function - they act both as negative electrodes in each battery cell and as current collectors on the negative side. Each fiber is covered with a thin solid polymer electrolyte (SPE) that works as both an electrolyte and a separator layer, enhancing the performance of every cell. The polymer matrix is doped with positive electrode particles (e.g., LiFePO4) to function as the positive electrode in the battery cell. An electrically conductive material, such as carbon black, is introduced into the matrix through doping to facilitate electrical conduction within the matrix. This cell design facilitates parallel operation of the single fiber battery cells, as depicted in Figure 1.4. The key

advantage of this design concept lies in the dramatic reduction of the distance between electrodes, resulting in enhanced performance and efficiency [24].

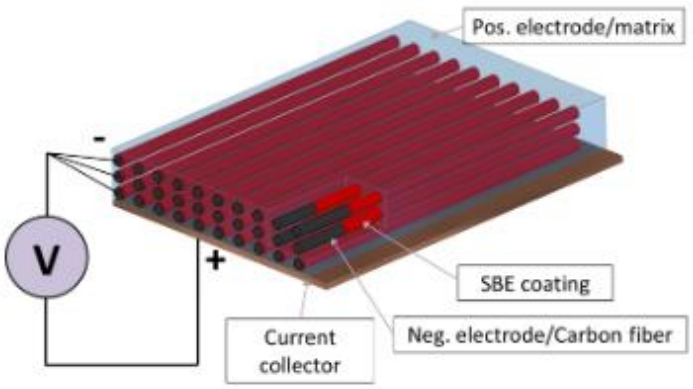


Figure 1.4. Schematic illustration of the 3D battery structural composite model [24].

The 3D battery concept offers several benefits and presents some potential challenges:

Advantages:

Enhanced Energy Density: The 3D design allows for a more compact and efficient use of space, potentially leading to higher energy density in the battery. This means the battery can store more energy for its size [18].

Reduced Electrode Distance: The concept significantly reduces the distance between electrodes, which can result in faster ion transport and improved battery performance. This can lead to quicker charging and discharging times. 3D batteries may exhibit higher energy conversion efficiency with a more direct path for ion movement, minimizing energy loss during charge and discharge cycles [24].

Flexibility in Design: The 3D battery concept offers design flexibility, allowing for the integration of battery functionality into various structures, which can be particularly valuable in applications where space is limited [19].

Challenges:

Manufacturing Complexity: Implementing the 3D battery design can be technically challenging and may require advanced manufacturing processes. The precision needed for coating individual fibers and ensuring uniform doping of the polymer matrix can be complex and costly [20].

Cost: The complex manufacturing process and materials used in 3D batteries may lead to higher production costs than traditional battery designs, which could impact the technology's cost-effectiveness [20].

Scaling Up: Transitioning from lab-scale prototypes to large-scale production can be challenging. Ensuring consistent quality and performance across a broader scale may require substantial research and development efforts [21, 22].

Safety Concerns: As with any battery technology, safety is paramount. Ensuring the safety of 3D batteries, especially when integrated into structural components, requires thorough testing and design considerations [1].

Long-Term Durability: The long-term durability and lifespan of 3D batteries need to be carefully studied and verified. The individual fiber cells should remain stable and functional over many charge-discharge cycles [23].

In summary, while the 3D battery concept offers promising benefits, including enhanced energy density and reduced electrode distance, it also faces challenges related to manufacturing complexity, cost, scaling up, safety, and long-term durability. Overcoming these challenges will be essential for realizing this innovative battery design's full potential in practical applications.

1.5 Distinct Regions in 3D Battery

3D battery design consists of three distinct components: a single carbon fiber serving as the negative electrode, a robust solid battery electrolyte (SBE) coating

that enhances performance and safety, and an integral positive electrode material, which also acts as a matrix (Figure 1.5).

The Electrochemical Capacity of Carbon Fibers

Carbon fibers exhibit a high specific capacity for lithium-ion storage, which means they can store a significant amount of lithium ions per unit mass. Various graphitized carbons have been employed as negative electrodes in rechargeable lithium-ion batteries. The carbon fibers' particular structure allows lithium ions' reversible intercalation and de-intercalation during charge and discharge cycles. This reversibility is essential for a battery's long-term stability and cycle life [25].

In the field of research, several studies [5, 26] have focused on the electrochemical properties of different types of carbon fibers. Researchers evaluated the electrochemical capacity of these carbon fibers by employing specially designed batteries [27]. They compared the lithium storage capacity during the initial cycle and after the tenth cycle. During their study, Kjell and his team noticed a decline in the electrochemical capacity, which eventually stabilized to a consistent reversible capacity following the first charge and discharge cycle [27]. This reduction in capacity after the initial charging cycle is typical in all lithium-ion batteries and results from forming an extremely thin protective layer known as the solid-electrolyte interphase (SEI).

The Role of Coating Region

In structural batteries, the coating region refers to a protective layer or coating applied to the fiber electrodes of the battery. This coating serves several important purposes within the context of structural batteries:

The coating region is a protective barrier encompassing the electrode materials, including positive and negative electrodes. Depending on the materials chosen, this coating may also function as an electrical insulator. In addition, the coating area performs the function of an electrolyte by assisting the transfer of lithium ions

between the two electrodes as the battery undergoes its charging and discharging cycles.

One of the critical parameters influencing battery performance is closely associated with the movement rate of ions. Lithium ions move from the negative electrode to the positive electrode when the battery generates electricity. The conductivity of the electrolyte material plays a critical role in determining the speed at which these ions move and, therefore, the strength of the resulting electric current [50]. Liquid electrolytes can achieve relatively high ion conductivity, reaching 10^{-2} S/cm [28]. In contrast, the best solid polymer electrolytes (SPE) exhibit conductivities of up to 10^{-5} S/cm [29]. However, they are chosen as an alternative due to their ability to support mechanical loads that liquid electrolytes cannot. Consequently, there is a trade-off between lower lithium-ion conductivity and the need for structural integrity in structural battery applications. Researchers in this field actively identify polymer systems with high mechanical stiffness and lithium-ion conductivity. [30].

Multifunctional Matrix region

Structural batteries utilize a matrix material that acts as a porous electrode. This material comprises a combination of solids such as electrolytes, electrochemically active material, electronic conductors, and polymer binder substances [31]. Creating this multifunctional matrix is often the most challenging part of developing structural batteries. This matrix must be strong enough to handle mechanical stress and allow ions to move. [4]. This balance is achieved by introducing electrochemically active materials (such as lithium iron phosphate, $LiFePO_4$) into the matrix. These host materials enable the extraction and insertion of lithium ions. Additionally, conductive additives are mixed into the electrolyte and polymer binder combination to facilitate ion movement. In this context, the active material constitutes the particle phase, while the other components (SBE, carbon black, and additional binder material) (Figure 1.6) collectively comprise the matrix material's binder phase [31].

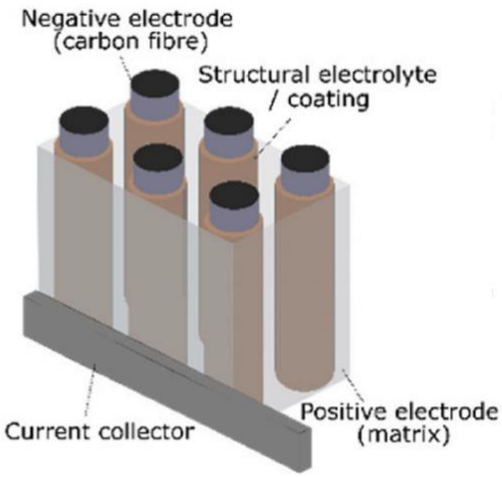


Figure 1.5. Schematic figure of the cross-section of the 3D battery [73]

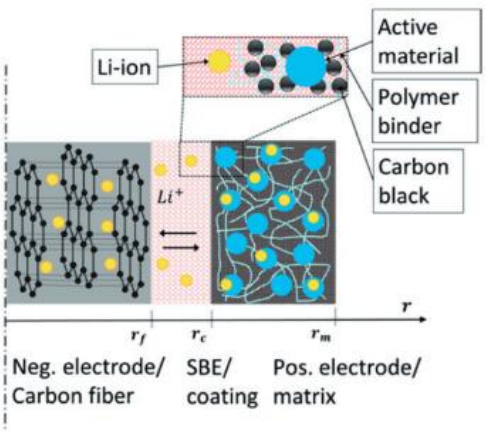


Figure 1.6. Axisymmetric schematic of the cell components Carbon Fiber, Coating, and Matrix) of 3D battery [4]

1.6 Electro-Chemo-Mechanical Coupling

To add the ability to store electricity in composite materials, a comprehensive understanding and mathematical representation of the electrochemical and mechanical properties and the reasons behind the failure of composite batteries are essential. The primary objective is to investigate mechanical stresses and strains induced by dimensional changes during the intercalation and deintercalation of Li

ions into and out of conductive materials. It is important to investigate crack formation on the surface of active materials to anticipate a decrease in cycling performance and reduced capacity. The commonly used method combines diffusion and continuum mechanics models [35, 36, 37].

The governing equations that describe the chemical field resemble those that govern heat conduction, suggesting an analogous relationship between ionic diffusion and heat conduction [34]. This similarity is also observed in material response, as the diffusion of lithium intercalation into the body leads to chemical swelling similar to the volume expansion produced under thermal load [34].

The method proposed by Dal and Miehe [54] enables the investigation of Li-ion diffusion during intercalation and deintercalation processes within electrode particles. They developed a semi-implicit finite element approach specifically tailored for electrode materials experiencing significant volume variations during charge-discharge cycles.

1.7 Crack Formation Due to Electrochemical Loading

In a phase field fracture framework, multiphysics coupling allows for simulating fiber failure due to diffusion-induced stresses while examining their susceptibility to cracking. Throughout a rechargeable battery's functional life, the individual fibers within it experience numerous cycles of ion intercalation and deintercalation (corresponding to charging and discharging). These repeated cycles result in uneven expansion of the fibers. This irregular expansion during each cycle of ion intercalation and deintercalation can give rise to the formation of mechanical stresses, which, in turn, may have the potential to create micro-damage within the fibers.

By drawing an analogy between thermo-mechanical effects and ion diffusion and employing finite element method (FEM)-based elastic stress analysis, Varna et al. [33] provide insights into the stress distributions and resultant crack behaviors

within the fiber. The study identifies two primary types of cracks in carbon fibers: radial cracks, caused by high hoop stresses during deintercalation, and arc cracks, which can deflect from radial cracks during subsequent intercalation cycles. Radial cracks grow initially but stop as the ion concentration gradient changes. Arc cracks exhibit unstable growth, influenced by the length of the originating radial crack. These arc-shaped cracks impact the diffusion process by acting as a barrier that obstructs the movement of ions through their exposed surfaces [33]. The study reveals the complex relationship between mechanical stresses and ion diffusion in affecting the structural integrity of carbon fibers. Stress analysis and ion concentration distribution with pre-defined cracks in the study of Varna et al. [33] supported these observations, indicating crack growth was not observed.

Varna and Xu (2019) studied the development of radial matrix and debond cracks at the coating/matrix interface in carbon fiber structural micro-battery composites. The numerical stress analysis reveals high hoop stress in the matrix during charging initiates radial matrix cracks at the coating/matrix interface [55]. The study uses 2-D finite element models to examine pre-defined radial matrix crack geometries and their growth from the coating/matrix interface, calculating energy release rates (ERR) under pure electrochemical loading. The results indicate that radial cracks significantly alter stress distribution, making debonding critical [55]. The presence of radial cracks leads to large tensile radial and shear stresses at the coating/matrix interface, emphasizing the importance of debonding. Furthermore, the study suggests that debond crack growth is governed by mode II, with lower ERR values for interface crack growth than radial matrix crack growth.

Varna and Xu (2020) performed a numerical analysis on developing matrix cracks under pure electrochemical loading and combined thermomechanical and electrochemical loading at the coating/matrix interface in the 90° layer of a cross-ply structural composite battery [56]. In cross-ply laminates, the likely failure sequence begins with the initiation and unstable growth of vertical radial matrix cracks, followed by the initiation of debonding at a certain matrix crack length,

propagating in a mixed mode. In unidirectional laminates, debonding typically does not occur without radial cracks [55]. However, debonds can form independently at the coating/matrix interface in cross-ply laminates. The study indicates that combined thermomechanical loading is a significant driving force for debonding crack growth [56].

Klinsmann et al. [35], who employed a crack growth model in idealized particles, modeled crack formation and growth using the phase field method. This model enables the simultaneous study of lithium concentration evolution and crack growth without restrictions on geometry, simulation dimensions, or predefined crack paths. They also discussed the effect of particle sizes and the charging rate on the stability of crack growth. The focus is on the lithium insertion process, revealing complex fracture phenomena like crack branching and complete breakage within a single half-cycle of lithium insertion. The phase field method allows for the simultaneous study of lithium diffusion and crack growth, revealing their mutual interaction. The growth of an initial interior crack can cause particle breakage in one insertion half-cycle, especially noticeable in large particles, at high diffusion rates, and with small initial cracks. Large initial cracks tend to stabilize after initial growth, but thin remaining ligaments are likely to fail during subsequent extraction cycles, as demonstrated by Klinsmann et al. [35].

Klinsmann et al. focus on lithium extraction [57], examining conditions that lead to unstable crack growth and particle breakage. Two horizontal cracks are replaced on opposite sides. Findings in this paper show that initial surface crack growth during extraction occurs under less severe conditions than during insertion, such as in smaller particles or with slower lithium extraction rates. Cracks generally grow stably towards the particle interior, stopping at some distance from the center. Depending on the diffusion rate, particle radius, and initial crack size, a phase of unstable growth may precede this stable regime. Particle breakage during a single extraction cycle is not observed. However, simulations show that the final crack tip location is at a radius likely to experience tensile stress in subsequent lithium

insertion cycles, suggesting that particle breakage may occur in a multi-step process [57].

Miehe et al. [76] have introduced a new finite strain theory for chemo-elasticity combined with phase-field modeling to simulate the multi-physics response of electrode particles in Li-ion batteries. The model connects crack evolution to the chemo-elastic response of the bulk material, utilizing both standard and gradient-extended Cahn–Hilliard-type diffusion for Li-ions [76]. The gradient-extended Cahn–Hilliard model considers potential phase segregation, providing a more realistic simulation of lithium diffusion.

Potentiostatic and potentiodynamic boundary conditions were applied to simulate realistic operational scenarios of lithium-ion batteries [76]. Potentiostatic boundary condition is essential for analyzing the steady-state behavior of the electrode material and its response to a constant applied potential. Potentiodynamic conditions involve varying the electrode potential, typically in a cyclic manner, to study the dynamic response of the electrode material. This boundary condition helps to understand the cyclic behavior of lithium-ion batteries, including phenomena such as hysteresis and cyclic degradation. The modular approach and the application of potentiostatic and potentiodynamic boundary conditions ensure that the model applies to real-world battery systems [76].

The phase field model was also applied to electrode particles to model fatigue cracking, drawing parallels between intercalation-deintercalation cycles and fatigue damage, as Martínez-Pañeda et al [40] demonstrated. The framework predicts non-linear crack propagation, displaying an exponential increase in cracked area with cycle number. Three stages of crack growth are observed: slow, accelerating, and unstable, with significant contributions from crack initiation at concave regions and crack merging. Fatigue damage susceptibility increases with higher diffusion rates and particle sizes, but reducing initial crack length can lead to more unstable cracking if above a critical size.

CHAPTER 2

MATHEMATICAL MODELING

In electrochemistry, the primary focus is investigating mechanical stresses and strains resulting from changes in dimensions during the intercalation and deintercalation of lithium ions [31]. This interest stems from the need to predict and prevent a decrease in battery capacity and a decline in its ability to work. These issues can occur when the fiber's structure gets damaged, typically by cracking, due to the changes in size caused by the lithium ions.

This section summarizes the definition of processes and the mathematical models related to mechanical stresses arising from electrochemical reactions.

2.1 Mathematical Models of Electrochemical and Mechanical Processes in the Lithium-ion Battery

The theory can be summarized as follows: Electrons flow internally through the electrodes, following Ohm's Law, while externally, they move through the outer circuit. The movement of lithium ions between two electrodes is facilitated by the electrolyte, which involves a combination of diffusion, described by Fick's Second Law of Mass Balance, and migration to maintain electro-neutrality [51]. These ions serve as reactants at the interfaces with the active materials, where intercalation reactions occur according to the Butler-Volmer Equation [54]. The ions are reduced during these reactions, and neutral lithium diffuses into the active material.

Fiber Region: Fick's diffusion law clarifies the transfer of lithium in the negative electrode's active material, primarily the carbon fiber, in the fiber region [31].

Coating Region: In the coating region, we explain how different types of particles in the electrolyte interact while modeling the mass transport process [31].

Matrix Region: The architecture of the electrode affects the movement of mass inside the electrolyte phase and the speed of chemical reactions taking place in the active material. Fick's second law can also characterize lithium concentration within the active material phase. Additionally, in the electrodes' electronically conductive phase, the electrons' movement is governed by Ohm's Law.

Reaction Kinetics

The Butler-Volmer equation governs the rate of chemical reactions that occur only at the surface of the active materials by relating the current density, concentration, and overpotential [31,43,54]. The Butler-Volmer equation is given by,

$$j = j_0 \left[\exp\left(\frac{\alpha_a F \eta}{RT}\right) - \exp\left(\frac{-\alpha_c F \eta}{RT}\right) \right]$$

Where j is the current density, j_0 is the exchange current density, α_a and α_c are the anodic and cathodic charge transfer coefficients, F is the Faraday constant, η is the overpotential, R is the gas constant, and T is the temperature.

Intercalation-induced volume changes:

As a battery operates, its composite unit cell changes volume. To model this behavior, we use a micro-battery cell model that assumes an infinitely long fiber and no shear stress components within the material. Figure 2.1 represents this model as an axisymmetric problem. A thermomechanical analogy can be utilized to determine the stress-strain relationship of transversely isotropic materials that undergo volumetric changes due to intercalation [33]. In this analogy, it is assumed that the dimensional alterations in the material are directly proportional to the concentration of lithium ions, denoted as "c". Subsequent chapters will explain in detail the complete set of equations, including their coefficients and independent variables.

The original electrochemical structural battery problem is a coupled system of 11 nonlinear partial differential equations on different scales with 11 unknowns, consisting of 4 regions (fiber, coating, matrix, active materials). This model is refined better to predict the performance metrics at different loading conditions.

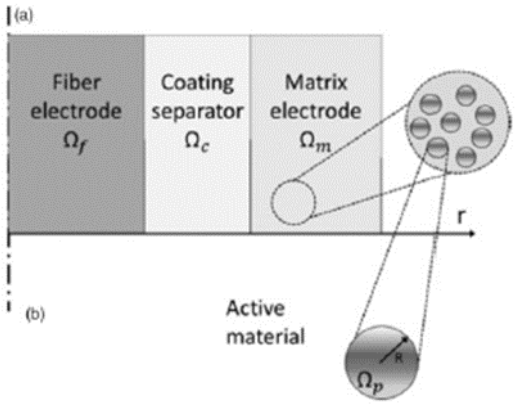


Figure 2.1. Schematic of the 3D-battery computational domains [31]

2.2 Simplified Mathematical Modeling

The analysis begins by focusing on the fiber region and employing simplified equation sets for a finite element approach aimed at exploring the interconnected behavior of electro-chemo-elastic materials, as discussed by Yang et al. [34] and Klinsmann et al. [35]. The critical emphasis lies in incorporating chemical effects into the equation system. A coupled equation set, including the ionic diffusion and momentum balance, is derived for a linearly coupled system, using the extended traditional Gibbs free energy to include chemical effects as a fundamental reference point. The proposed model mimics fiber region diffusion. Coating/Matrix is considered a boundary condition at the outer surface of the fiber. The material properties are assumed to be isotropic. The small strain assumption is applied for the formulation. The boundary condition is applied as the prescribed concentration at the outer surface, either linearly increasing or constant. The linearly increased concentrations reflect a controlled charging process where the surface

concentration gradually increases. The Butler-Volmer equation can be applied by calculating the resulting current density for the changing concentration and corresponding overpotential. Holding the concentration constant at the end of the process is analogous to a potentiostatic condition where the concentration does not change, and the Butler-Volmer equation can be used to describe the steady-state current density.

2.2.1 Governing Equations of the Field

Two fundamental equilibrium equations, commonly found in continuum mechanics, explain the interaction between lithium diffusion and mechanical stress in the storage particles of lithium-ion batteries.

The main factor responsible for the movement of ions within a liquid is ionic diffusion [34, 35]. By ignoring the convection effect (i.e., the macroscopic motion of the ions is not considered [36]), we have

$$\dot{c} + \nabla \cdot \mathbf{J} = 0 \text{ in } \Omega, \tag{2-1}$$

where c is the Li concentration per unit volume, $\dot{c}$ is the time rate of change of Li ions, $\mathbf{J}$ is the flux of Li ions.

The second one is the static equilibrium equation,

$$\nabla \cdot \boldsymbol{\sigma} = 0 \text{ in } \Omega, \tag{2-2}$$

where the body forces are neglected. $\boldsymbol{\sigma}$ represents the Stress Tensor. The equations mentioned above for equilibrium can only be applied to small deformation.

2.2.2 Free Energy and Constitutive Laws

The Gibbs free energy per unit volume is often denoted as g, a thermodynamic property representing the energy available to work in a system at constant temperature and pressure [34].

The expression for the extended Gibbs free energy per unit volume can be written by adding chemical energy [36] and excluding thermal and electrical energy, assuming that these effects are insignificant compared to the chemical and mechanical effects.

$$g = u_{mechanical} + u_{chemical} \tag{2-3}$$

where g is extended Gibbs free energy density, u denotes the internal energy density, including the mechanical and chemical energy contributions. Mechanical energy can be further expressed as strain energy because it represents the energy associated with deformation in the material due to applied mechanical forces. This reflects a focus on the material's response to mechanical loading. The precise expression for strain energy will depend on the material's constitutive equations and behavior under stress and strain.

$$g = u_{strain} + u_{chemical} \tag{2-4}$$

For an isotropic elastic material, the internal strain energy density is typically given by:

$$u_{strain} = \frac{1}{2}\sigma_{ij}\varepsilon_{ij} \tag{2-5}$$

where σ_{ij} is the stress tensor and ε_{ij} strain tensor. The general expression for the stress-strain relationship for an elastic material is given by Hooke's law,

$$\sigma_{ij} = \lambda\varepsilon_{kk}\delta_{ij} + 2\mu\varepsilon_{ij} \tag{2-6}$$

where λ and μ are Lamé parameters and ε_{kk} is the sum of normal strains (volumetric strain), and δ_{ij} is the Kronecker delta, which equals 1 when $i = j$ and 0 otherwise. Substitute the stress-strain relationship into the expression for u_{strain},

$$u_{strain} = \frac{1}{2}\left[(\lambda\varepsilon_{kk}\delta_{ij} + 2\mu\varepsilon_{ij})\varepsilon_{ij}\right] \tag{2-7}$$

The final version of internal strain energy density in reads

$$u_{strain} = \frac{1}{2}\left(\lambda \varepsilon_{ii}\varepsilon_{jj} + 2\mu \varepsilon_{ij}\varepsilon_{ij}\right) \tag{2-8}$$

In this equation, λ and μ are material properties that characterize the behavior of the isotropic linear elastic material. They are related to the material's bulk modulus (K), a measure of the material resistance to volume change and shear modulus (G), a measure of material's resistance to shear deformation as follows, $K = \lambda + \frac{2\mu}{3}$ and $G = \mu$. This formulation applies to linearly isotropic materials like most common elastic solids under small deformations. Under small strain assumption, the constitutive relation for stress ($\boldsymbol{\sigma}$) depends only on the symmetric part of the gradient of displacement $\mathbf{u}$

$$\boldsymbol{\varepsilon} = \frac{1}{2}[\nabla \mathbf{u} + (\nabla \mathbf{u})^T] \tag{2-9}$$

$\boldsymbol{\varepsilon}$ is the total strain and decomposed as

$$\boldsymbol{\varepsilon} = \boldsymbol{\varepsilon}^e + \boldsymbol{\varepsilon}^{ch}, \tag{2-10}$$

where $\boldsymbol{\varepsilon}^e$ is the elastic strain and $\boldsymbol{\varepsilon}^{ch}$ is the chemical strain. It is assumed that isotropic volume expansion due to Li movement is linearly dependent on the local concentration [35,8] via

$$\boldsymbol{\varepsilon}^{ch} = \frac{\Omega_c}{3}(c - c_0)\mathbf{1} \tag{2-11}$$

where Ω_c is the lithium partial molar volume, c_0 is reference concentration and $\mathbf{1}$ is the identity tensor. The elastic strain energy density, Eq. 2-8, can be written for elastic strain $\boldsymbol{\varepsilon}^e = \boldsymbol{\varepsilon} - \boldsymbol{\varepsilon}^{ch}$ with the help of a trace operator, $tr\,[\mathbf{A}] = A_{ii}$

$$u_{strain} = \frac{1}{2}\left(\lambda\left[tr(\boldsymbol{\varepsilon} - \boldsymbol{\varepsilon}^{ch})\right]^2 + 2\mu\, tr[(\boldsymbol{\varepsilon} - \boldsymbol{\varepsilon}^{ch})^2]\right) \tag{2-12}$$

The chemical energy density, $u_{chemical}$, in terms of electrochemical potential μ and ionic concentration c, related to the energy stored in the electrochemical potential of ions [7, 6].

$$u_{chemical} = \mu\, c \tag{2-13}$$

In classical physical chemistry, the Nernst equation (Eq. 2-14) represents ions' concentration and chemical potential and same for both galvanostatic and potentiostatic conditions [34].

$$\mu = \mu_0 + zF\emptyset + RT\, ln\frac{c}{c_0} \tag{2-14}$$

where z is the charge number, F is the Faraday constant, and $\emptyset$ is the electric potential. The second term in the Nernst equation ($zF\emptyset$) is the electrostatic term that can be ignored if the change in potential does not significantly affect the chemical potential of the ions [34]. This is applicable in some low-field conditions or during parts of the charging process where the electric field effects are minimal [34]. In scenarios where the electric field or potential changes are significant (e.g., during rapid charging or discharging or in high-field regions near the electrodes), neglecting the electrostatic term could lead to inaccuracies [60]. Additionally, the Nernst Equation assumes that Li ions are neutral, meaning the ion's charge number is zero.

$$\mu = \mu_0 + RT\, ln\frac{c}{c_0} \tag{2-15}$$

where R is the gas constant ($Jmol^{-1}K^{-1}$), T is temperature (K), c_0 reference concentration (mol/m^3) and μ_0 reference chemical potential ($Jmol^{-1}$). The Gibbs free energy per unit volume for the isotropic linearly coupled electrochemical system is defined in terms of strain $\boldsymbol{\varepsilon}$ and concentrations c

$$g = \frac{1}{2}\left(\lambda[tr(\boldsymbol{\varepsilon} - \boldsymbol{\varepsilon}^{ch})]^2 + 2G\, tr[\left(\boldsymbol{\varepsilon} - \boldsymbol{\varepsilon}^{ch}\right)^2]\right) + \mu_0 c + RT\, c\, ln\frac{c}{c_0} \tag{2-16}$$

Equations 2-1 and 2-2 require constitutive equations that describe the physical behavior of the material, relating the electrical potential, μ and stress $\boldsymbol{\sigma}$ with the

principal variables: ionic concentration (c) and displacement ($\mathbf{u}$). For a compact formulation, the derivative of the Gibbs free energy function with respect to strain $\boldsymbol{\varepsilon}$ can be used to calculate stress

$$\boldsymbol{\sigma} = \partial_{\varepsilon} g = \lambda tr\left(\boldsymbol{\varepsilon} - \boldsymbol{\varepsilon}^{\boldsymbol{ch}}\right)\mathbf{1} + 2G\left(\boldsymbol{\varepsilon} - \boldsymbol{\varepsilon}^{ch}\right). \tag{2-17}$$

For the chemical potential calculation of the coupled system, the derivative of Gibbs free energy density function to concentration c is used as follows. Note that the partial molar volume of Li concentration, which is Ω_c (m^3/mol) is multiplied by the first and second terms to make consistency in units of μ and comes from the definition of chemical strain (Eq. 2.11).

$$\mu = \partial_{\boldsymbol{c}} g = (-\lambda)\Omega_c tr\left(\boldsymbol{\varepsilon} - \boldsymbol{\varepsilon}^{ch}\right) - \frac{2G}{3}\Omega_c tr\left(\boldsymbol{\varepsilon} - \boldsymbol{\varepsilon}^{ch}\right) + \mu_0 + RT\left(1 + ln\frac{c}{c_0}\right), \tag{2-18}$$

where $K = \lambda + \frac{2\mu}{3}$ and $G = \mu$ (Lamé parameter) Eq. 2-18 can be rewritten as,

$$\mu = -K\Omega_c tr\left(\boldsymbol{\varepsilon} - \boldsymbol{\varepsilon}^{ch}\right) + \mu_0 + RT\left(1 + ln\frac{c}{c_0}\right). \tag{2-19}$$

2.2.3 Linear and Nonlinear Chemical Field Equations

The literature has used two approaches to determine the relation between electrochemical potential and ionic concentration. In this section, these relations are discussed.

2.2.3.1 Linear Approach

In this part linear relation ($\mu = S\,c$) is assumed between the electrochemical potential and concentration [34]. The proportional coefficient of chemical potential

and concentration, which is denoted as S, is calculated as follows. The Nernst equation (Eq. 2-15), can be modified for the current concentrations as $\bar{c} = c + c_0$

$$\mu = \mu_0 + RT\, ln \frac{c + c_0}{c_0} \tag{2-20}$$

The differentiation of this equation is given by

$$d\mu = S\, dc = RT \frac{dc}{c + c_0}. \tag{2-21}$$

Considering an infinitesimal change in concentration, we have,

$$S = RT \lim_{c \to 0} \frac{1}{c + c_0} = \frac{RT}{c_0} \tag{2-22}$$

If the temperature change is very small [34], the absolute temperature approximates the initial temperature. y, the dimension of chemical potential μ is $Jmol^{-1}$ and ionic concentration c is $molm^{-3}$, thus S have the dimension of $Jmol^{-2}\ m^{-3}$. The potential equation (Eq. 2-19) can be modified according to a linear relation

$$\mu = -K\Omega_c tr\left(\boldsymbol{\varepsilon} - \boldsymbol{\varepsilon}^{ch}\right) + \mu_0 + \frac{RT}{c_0} c. \tag{2-23}$$

In the linear method, the movement of Li ions (flux) (**J**) is described by Fick's first law, which is steady-state diffusion. This law states that the movement is proportional to the concentration gradient of the ions. The diffusion coefficient D_0 denotes this proportionality of anions and cations [34]. For isotropic medium, the same increments are assumed.

$$\mathbf{J} = -D_0 \nabla c \tag{2-24}$$

2.2.3.2 Nonlinear Approach

In a nonlinear approach, the convection-diffusion equation (Eq. 2-1) is a specific form of material balance equation that includes terms for diffusive transport (due to

concentration gradients) and convective transport (due to fluid motion or electric fields) [8, 35, 45]. For lithium ions in an electrolyte, the flux **J** can be expressed as:

$$\mathbf{J} = -\varphi \nabla \mathrm{c} + \mathrm{c}\mathbf{v} \tag{2-25}$$

where φ is the diffusion coefficient **v** is the velocity field (which includes both convective fluid motion and migration due to electric field [35, 45]. The velocity of lithium ions can be expressed as

$$\boldsymbol{v} = -M\nabla\mu \tag{2-26}$$

where M is the mobility of lithium ions, and μ is the chemical potential. The species flux can then be written as

$$\mathbf{J} = \mathrm{c}\mathbf{v} = -Mc\nabla\mu \tag{2-27}$$

where c is the concentration of the lithium ions and $M = \frac{D_0}{RT}\left(1 - {}^{c}/_{c_{max}}\right)$ [35, 45] and Li Flux is given by [35]

$$\mathbf{J} = -D_0\nabla c + \frac{D_0\Omega_c}{RT}c\left(1 - {}^{c}/_{c_{max}}\right)\nabla\sigma_h \tag{2-28}$$

The first term on the right side of the equation (2-28) corresponds to Linear diffusion, which results from constant mobility and Lithium concentrations that are less than the maximum concentration (c_{max}). In addition, the concentration-dependent mobility of Li, as explained in Equation (2-25), confirms that stress gradient-driven diffusion controlled by the second term on the right-hand side of Equation (2-28) and determines that it is negligible at low and high Li concentrations [35]. The second term is important for describing lithium-ion diffusion in materials where both concentration and stress gradients are significant, such as in the presence of mechanical stresses and where the mobility of lithium ions varies with concentration. Equation (2-28) suggests that the second term is negligible at very low and very high lithium concentrations. The stress gradient can also be neglected if constant mobility is assumed [35].

In their work, Dal and Miehe [54] address the challenge of accurately computing the pressure gradient term using continuous shape functions by introducing a semi-

implicit scheme with an explicit definition of the pressure gradient. They employ a projection algorithm and an additional negative pressure field to improve the accuracy and stability of the gradient computation. This approach allows for more accurate modeling of the Li-ion flux in lithium-ion battery electrodes, essential for reliable simulation of their electro-chemo-mechanical behavior [54].

The electrochemical potential in nonlinear solution is expressed as

$$\mu = -\Omega_c \sigma_h + \mu_0 - RTln\frac{1 - {}^{c}/_{c_{max}}}{{}^{c}/_{c_{max}}} \tag{2-29}$$

where Ω_c is the molar volume of Li ion, c_{max} is the maximum ionic concentration and hydrostatic stress (σ_h) given by,

$$\sigma_h = \frac{1}{3} tr[\boldsymbol{\sigma}] \tag{2-30}$$

Table 2.1 The set of Equations with Boundary Conditions of the Coupled System

	Mechanical	**Electrochemical**
Independent variables	u_i	c
Governing Equations	$\nabla \cdot \boldsymbol{\sigma} = 0$	$\dot{c} + \nabla \cdot \mathbf{J} = 0$
Boundary Conditions	$\sigma_{ij} n_j - \bar{t}_i = 0$ $u_i = \bar{u}_i$	$D_0\, c_{,i} n_i = -\overline{J_n}$ $c = \bar{c}_0$
Strain/Displacement and Flux/Concentration relations	$\boldsymbol{\varepsilon} = \frac{1}{2}[\nabla \mathbf{u} + (\nabla \mathbf{u})^T]$	$\mathbf{J} = -D_0 \nabla c$ for linear approach $\mathbf{J} = -D_0 \nabla c + \frac{D_0 \Omega_c}{RT} c(1 - {}^{c}/_{c_{max}}) \nabla \sigma_h$ for nonlinear approach
Constitutive relations of the coupled system	$\boldsymbol{\sigma} = \lambda tr(\boldsymbol{\varepsilon} - \boldsymbol{\varepsilon}^{ch})\mathbf{1}$ $+2\mu(\boldsymbol{\varepsilon} - \boldsymbol{\varepsilon}^{ch})$	$\mu = -K\Omega_c tr(\boldsymbol{\varepsilon} - \boldsymbol{\varepsilon}^{ch}) + \mu_0 + \frac{RT}{c_0} c$ for linear approach $\mu = -\Omega_c \sigma_h + \mu_0 - RTln\frac{1 - {}^{c}/_{c_{max}}}{{}^{c}/_{c_{max}}}$ for nonlinear approach

The initial and boundary conditions of the coupled system can be defined on the domain Ω describing the storage particle geometry and its boundary S. We denote prescribed displacements by $\bar{\boldsymbol{u}}$, tractions by $\bar{\boldsymbol{t}}$, concentration by $\bar{c}_0$ and fluxes by $\bar{\boldsymbol{J}}_n$. The required initial conditions have the form $c(x,t_0)=c_0$ and $u(x,t_0)=u_0$. The set of mechanical and linear/nonlinear electrochemical equations with boundary conditions for the electrochemical problem is tabulated in Table 2.1.

The Gibbs free energy per unit volume for an electrochemical system is rewritten for linear and nonlinear electrochemical approaches in terms of strain $\boldsymbol{\varepsilon}$ and concentrations c in equation (2-27) and (2-28), respectively.

$$g = \frac{1}{2}\left(\lambda[tr(\boldsymbol{\varepsilon}-\boldsymbol{\varepsilon}^{ch})]^2 + 2G\ tr[\left(\boldsymbol{\varepsilon}-\boldsymbol{\varepsilon}^{ch}\right)^2]\right) + \mu_0 c + \frac{RT}{2c_0}c^2 \tag{2-31}$$

$$g = \frac{1}{2}\left(\lambda\left[tr(\boldsymbol{\varepsilon}-\boldsymbol{\varepsilon}^{ch})\right]^2 + 2G\ tr[\left(\boldsymbol{\varepsilon}-\boldsymbol{\varepsilon}^{ch}\right)^2]\right) + \mu_0 c + RT\ c\ ln\frac{c}{c_0} \tag{2-32}$$

2.3 Phase Field Implementation to Solution of Coupled System

To study the damage mechanisms of the composite battery, a phase field model for fracture is integrated into the coupled system to model the growth of cracks. The phase field method has emerged as a highly effective approach for addressing and mitigating the challenges associated with earlier numerical methods. Within the phase field method, the traditional concept of a sharp, well-defined crack is transformed into a more flexible representation characterized as a diffuse crack zone [37,38].

The phase field technique is a major improvement in crack analysis and simulation, as it removes the necessity for arbitrary standards to identify the paths of cracks and the need to separate, delete, or re-meshing elements [39]. It not only smoothly monitors crack growth but can also precisely depict the onset and branching of

cracks. It is particularly effective in handling complex crack patterns and interactions without additional computational complexity [70].

This transformation is made possible by introducing a scalar phase field variable known as the order parameter. This new method provides a more accurate and adaptable way to describe how cracks behave in materials [40, 41]. It is especially useful for modeling the complex processes of crack formation, branching, and interaction, which were challenging to represent accurately using older numerical methods.

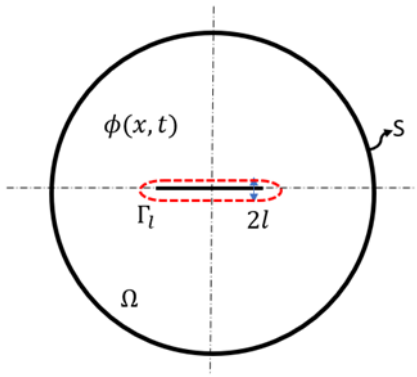


Figure 2.2. A phase field approximation of the discrete discontinuities

In the phase field fracture framework, cracks are represented by a diffuse field variable $\phi \in [0,1]$. Here, $\phi = 0$ signifies undamaged or intact material, while $\phi = 1$ signifies the fully broken material state. The extent of the smoothed crack surface is determined by the selection of the length scale parameter, denoted as l. A regularized crack density functional, denoted as $\Gamma_l(l,\phi)$, can be established (Figure 2.2). This functional converges to the discrete crack's functional as the length scale parameter, " l " approaches zero [49]. As a result, the approximation of the fracture energy related to crack formation can be obtained as follows:

$$\int_{\Gamma_c} G_c d\Gamma_c = \int_{\Omega} G_c \left(\frac{1}{2l}\phi^2 + \frac{l}{2}|\nabla\phi|^2\right) d\Omega \tag{2-33}$$

The total potential energy of a solid can be obtained by combining the bulk energy and the estimated energy of the cracked surface (Ψ)

$$\Psi = \int_{\Omega} \left\{ (1-\phi)^2 \mathrm{g}(\boldsymbol{\varepsilon}, \mathrm{c}) + G_c \left(\frac{1}{2l}\phi^2 + \frac{l}{2}|\nabla\phi|^2 \right) \right\} d\Omega \tag{2-34}$$

where the term $(1-\phi)^2$ describes the degradation of the stored energy with evolving damage. Here, $\mathrm{k} = 10^{-6}$ is a numerical parameter chosen to stabilize the solution. By taking the first variation of Eq. 2-34 and applying the Gauss theorem, the following steps are followed for obtaining the coupled field equation.

$$\delta\Psi_{\phi} = \frac{\partial \Psi}{\partial \phi}\, \delta\phi = 0 \tag{2-35}$$

Taking the variation of the total potential energy of the solid with respect to $\delta\phi$

$$\delta\Psi_{\phi} = \int_{\Omega} \frac{\delta}{\delta\phi} \left\{ (1-\phi)^2 \mathrm{g}(\boldsymbol{\varepsilon}, \mathrm{c}) + G_c \left(\frac{1}{2l}\phi^2 + \frac{l}{2}|\nabla\phi|^2 \right) \right\} \delta\phi d\Omega = 0 \tag{2-36}$$

and $\nabla\phi \cdot \boldsymbol{n} = 0$ on dS

$$\delta\Psi_{\phi} = \int_{\Omega} \left\{ G_c \left(\frac{1}{l}\phi + l\nabla\phi \cdot \nabla(\delta\phi) \right) - 2(1-\phi) g(\boldsymbol{\varepsilon}, c) \right\} \delta\phi d\Omega \tag{2-37}$$

applying integration by parts to the gradient term with respect to $\delta\phi$ and applying Gauss theorem,

$$G_c l \int_{\Omega} \nabla\phi \cdot \nabla(\delta\phi) d\Omega = -G_c l \int_{\Omega} \Delta\phi \delta\phi d\Omega + G_c l \int_{\partial\Omega} (\nabla\phi \cdot \boldsymbol{n}) \delta\phi dS \tag{2-38}$$

and $\nabla\phi \cdot \boldsymbol{n} = 0$ on dS

substituting this back into the variation,

$$\delta\Psi_{\phi} = \int_{\Omega} \left\{ G_c \left(\frac{1}{l}\phi - l\Delta\phi \right) - 2(1-\phi) g(\boldsymbol{\varepsilon}, c) \right\} \delta\phi d\Omega = 0 \tag{2-39}$$

The coupled phase field equation is obtained by,

$$G_c \left(\frac{1}{l}\phi - l\Delta\phi \right) - 2(1-\phi) g(\boldsymbol{\varepsilon}, c) = 0 \tag{2-40}$$

It is possible to incorporate a regularization technique that utilizes a viscous crack resistance to improve the algorithm's robustness. This work aims to solve the deviation and instability problems during crack propagation, especially in the chemo-mechanical case. We can introduce viscous regularization to ensure that solution paths remain stable after a critical point. This consists of the introduction of a viscous term ($\eta\dot{\phi}$) (the time derivative of the phase field variable) and viscosity parameter $\eta = 1 \times 10^{-6}$ Ns/mm^2 that supplements the crack surface resistance. This feature of the proposed theory is a very important element of stable computational execution; see Miehe et al. (2010b) [38]. The modified phase field equation with a viscous term is,

$$G_c\left(\frac{1}{l}\phi - l\Delta\phi\right) + \eta\dot{\phi} - 2(1-\phi)g(\boldsymbol{\varepsilon}, c) = 0 \tag{2-41}$$

with satisfying the following the boundary condition

$$\nabla\phi \cdot \boldsymbol{n} = 0 \text{ on } \partial\Omega \tag{2-42}$$

In the finite element method, the update of the phase field variable is based on a history variable that represents the localized maximum energy caused by positive normal strains.

$$G_c\left(\frac{1}{l}\phi - l\Delta\phi\right) + \eta\dot{\phi} - 2(1-\phi)\mathrm{H}^{+}(\boldsymbol{\varepsilon}(\mathrm{t}), \mathrm{c}(\mathrm{t}))) = 0 \tag{2-43}$$

$$\mathrm{H}^{+} = \max_{\mathrm{t}\epsilon[0,\tau]}\mathrm{g}^{+}(\varepsilon(\mathrm{t}), \mathrm{c}(\mathrm{t})) \tag{2-44}$$

H^{+} is called history variable field which plays a crucial role in the phase field theory. It monitors and accumulates elastic strain energy during material deformation, essentially serving as a memory bank that records the maximum strain energy at various points. This information is vital for tracking the evolution of cracks and structural changes over time. When updating the phase field variable, the history variable offers critical insights, helping the model identify areas of high-strain energy where cracks might form or grow [40]. By incorporating the history

variable into the solution scheme, the model can make informed decisions about accurately representing the material's changing structural integrity. Ultimately, the history variable bridges material mechanics with the phase field model, ensuring an accurate depiction of physical processes, particularly crack formation and propagation. Additionally, the history field plays a crucial role in preventing healing within the material. Since the phase field variable is irreversible, the history variable ensures that once a crack forms, it does not heal, accurately reflecting the material's irreversible damage. This is important for maintaining the integrity of the phase field model in simulating real-world scenarios where material damage is permanent.

By implementing a strain energy decomposition to prevent cracking in compression, as proposed by Amor et al. [42] in their volumetric-deviatoric split approach, it is assumed that the strain energies associated with volume change and shear deformation can be susceptible to damage, while the volumetric strain energy under compression remains unaffected. Thus, the strain energy can be decomposed as

$$g^{+}(\boldsymbol{\varepsilon}(\mathrm{t}), c(t)) = \frac{1}{2}K\left\langle \mathrm{tr}(\boldsymbol{\varepsilon} - \boldsymbol{\varepsilon}^{ch})\right\rangle_{+}^{2} + \mu((\boldsymbol{\varepsilon} - \boldsymbol{\varepsilon}^{ch})^{dev} : (\boldsymbol{\varepsilon} - \boldsymbol{\varepsilon}^{ch})^{dev}) \tag{2-45}$$

Here, $\langle a\rangle_{+} = \frac{1}{2}(a + |a|)$, K is the bulk modulus and deviatoric strain tensor, which measure the distortion of the material's shape without any volume change. And defined as $\varepsilon^{dev} = \varepsilon - \frac{1}{3}tr(\varepsilon)\mathbf{1}$

2.4 Weak Forms and Solution Algorithms

To account for the coupling effect in the multifield case, we need to modify Equation 2-1. To do this, we can differentiate Equation 2.20 with respect to time.

$$\frac{\partial \mu}{\partial t} = \frac{RT}{c}\frac{\partial c}{\partial t} \tag{2-46}$$

Consider a small concentration increment, $\bar{c} = c + c_0 \approx c_0$, [34] we can obtain,

$$\frac{\partial \mu}{\partial t} = \frac{RT}{c_0}\frac{\partial c}{\partial t} \tag{2-47}$$

The modified diffusion equation for multifield problems can be rewritten as,

$$\dot{\mu} + \frac{RT}{c_0}\nabla \cdot \mathbf{J} = 0 \text{ in } \Omega \tag{2-48}$$

where $\dot{\mu}$ is time derivative of electrochemical potential. The linear relation (Eq. 2-23) can be written as

$$\dot{\mu} = -K\Omega_c tr\left(\dot{\boldsymbol{\varepsilon}} - \dot{\boldsymbol{\varepsilon}}^{ch}\right) + \frac{RT}{c_0}\dot{c} \tag{2-49}$$

and for isotropic medium Eq. 2-28 explains the relationship between ionic concentration and flux as $\mathbf{J} = -D_0\nabla c$ and material constant $\tau = \frac{RT}{c_0}$

The final form of the diffusion equation is,

$$-K\Omega_c tr\left(\dot{\boldsymbol{\varepsilon}} - \dot{\boldsymbol{\varepsilon}}^{ch}\right) + \tau\dot{c} - \tau D_0\nabla^2 c = 0 \text{ in } \Omega \tag{2-50}$$

To derive the weak form, we will follow the standard procedure in the finite element method (FEM) by multiplying the equation by a test function $\hat{c}$ and integrating it over the domain Ω

$$-K\Omega_c\int_\Omega tr\left(\dot{\boldsymbol{\varepsilon}} - \dot{\boldsymbol{\varepsilon}}^{ch}\right)\hat{c}\, d\Omega + \tau\int_\Omega \dot{c}\hat{c}d\Omega - \tau D_0\int_\Omega \nabla^2 c\hat{c}\, d\Omega = 0. \tag{2-51}$$

Now, we can apply integration by parts to the third term of the Eq (2-47), which results in:

$$\begin{gathered}-K\Omega_c\int_\Omega tr\left(\dot{\boldsymbol{\varepsilon}} - \dot{\boldsymbol{\varepsilon}}^{ch}\right)\hat{c}\, d\Omega + \tau\int_\Omega \dot{c}\hat{c}d\Omega + \tau D_0\int_\Omega \nabla c\cdot\nabla\hat{c}d\Omega \\ -D_0\int_{\partial\Omega}(\nabla c\cdot n)\hat{c}\, dS = 0\end{gathered} \tag{2-52}$$

Here, $\partial\Omega$ represents the boundary of the domain Ω, n is the outward unit normal vector, and dS represents the differential surface area. By setting $\dot{\boldsymbol{\varepsilon}} - \dot{\boldsymbol{\varepsilon}}^{ch} = \dot{\boldsymbol{\varepsilon}}^{el}$, the finite difference approximations of rate of change of elastic strain and

concentration for current time step and previous time step are $\dot{\boldsymbol{\varepsilon}}^{el} = \frac{\boldsymbol{\varepsilon}^{el} - \boldsymbol{\varepsilon}_n^{el}}{\Delta t}$ and $\dot{c} = \frac{c - c_n}{\Delta t}$. The final form of the weak form is

$$\int_{\Omega} (-K\Omega_c tr\left(\frac{\boldsymbol{\varepsilon}^{el} - \boldsymbol{\varepsilon}_n^{el}}{\Delta t}\right) + \tau \frac{c - c_n}{\Delta t})\hat{c} d\Omega - D_0 \int_{\Omega} \tau[(1-\phi)^2 + \mathrm{k}]\nabla c \cdot \nabla \hat{c}\, d\Omega = \int_{\partial\Omega} \tau[(1-\phi)^2 + k] D_0 (\nabla c \cdot n)\hat{c}\, dS \tag{2-53}$$

In the above equation, the chemical diffusivity D_0 is allowed to degrade by $[(1-\phi)^2 + k]$ with the evolution of the phase field variable [47], where $\mathrm{k} = 10^{-6}$ is a numerical parameter chosen to stabilize the solution. In this problem, $\boldsymbol{\varepsilon}_n^{el}$ is the elastic strain and c_n is the ionic concentration calculated in the previous time step.

The same procedure is applied to calculate weak form static equilibrium equation. Equation (2-2) is multiplied by a test function v and integration over the domain Ω.

$$\int_{\Omega} \nabla \cdot \boldsymbol{\sigma}(\boldsymbol{\varepsilon}, \mathrm{c}) \cdot v d\Omega = 0 \tag{2-54}$$

Now, apply Gauss's divergence theorem to Eq. (2-50),

$$\int_{\Omega} (\nabla \cdot \boldsymbol{\sigma}(\boldsymbol{\varepsilon}, \mathrm{c})) \cdot v d\Omega = \int_{\partial\Omega} (\boldsymbol{\sigma}(\boldsymbol{\varepsilon}, \mathrm{c}) \cdot \boldsymbol{n}) \cdot v dS - \int_{\partial\Omega} \boldsymbol{\sigma}(\boldsymbol{\varepsilon}, \mathrm{c}) : \nabla v d\Omega = 0 \tag{2-55}$$

In this equation, $d\Omega$ represents the boundary of the domain Ω, $\boldsymbol{n}$ is the outward unit normal vector, and dS represents the differential surface of the boundary. Equation (2-55) has two terms; the surface integral term represents the flux of the stress tensor $\boldsymbol{\sigma}$ across the boundary of the domain, and the volume integral term involves the contraction (double dot product) of $\boldsymbol{\sigma}$ and the gradient of the test function ∇v.

To resultant weak form is

$$\int_{d\Omega} (\boldsymbol{\sigma}(\boldsymbol{\varepsilon}, \mathrm{c}) \cdot n) \cdot v dS - \int_{d\Omega} \boldsymbol{\sigma}(\boldsymbol{\varepsilon}, \mathrm{c}) : \nabla v d\Omega = 0 \tag{2-56}$$

where the traction vector is $t = \boldsymbol{\sigma}(\boldsymbol{\varepsilon}, \mathrm{c}) \cdot n$ and from Eq. 2-16,

$$\boldsymbol{\sigma}(\boldsymbol{\varepsilon}, \mathrm{c}) = \lambda tr(\boldsymbol{\varepsilon} - \boldsymbol{\varepsilon}^{ch})\mathbf{1} + 2\mu(\boldsymbol{\varepsilon} - \boldsymbol{\varepsilon}^{ch}) \tag{2-16}$$

The weak form of the linear momentum equation in this coupled system is modified for phase field coupling, the final form of the coupled weak form is

$$\int_{\Omega}[(1-\phi)^2+\mathrm{k}]\left(\lambda tr\left(\boldsymbol{\varepsilon}-\boldsymbol{\varepsilon}^{ch}\right)\mathbf{1}+2\mu(\boldsymbol{\varepsilon}-\boldsymbol{\varepsilon}^{ch})\right):\nabla v d\Omega=\int_{d\Omega}\boldsymbol{t}\cdot v dS \tag{2-57}$$

The weak form of phase field equation (Eq. 2-43) of the coupled system can be calculated by the following procedure. This equation multiplied with test function q and integrate over domain Ω.

$$\int_{\Omega}\left[\left(G_c\left(\frac{1}{l}\phi-l\Delta\phi\right)+\eta\dot{\phi}-2(1-\phi)\mathrm{H}^{+}(\boldsymbol{\varepsilon}(\mathrm{t}),\mathrm{c}(\mathrm{t}))\right)q\right]d\Omega=0 \tag{2-58}$$

$$\int_{\Omega}\left[G_c\frac{1}{l}\phi q-G_c l\Delta\phi q+\eta\dot{\phi}q-2(1-\phi)\mathrm{H}^{+}(\boldsymbol{\varepsilon}(\mathrm{t}),\mathrm{c}(\mathrm{t}))q\right]d\Omega=0 \tag{2-59}$$

The integration by parts is applied to the equation. Using divergence theorem, we can write second term as follows

$$-\int_{\Omega}G_c l\Delta\phi q\,d\Omega=-\int_{d\Omega}(G_c l\nabla\phi\cdot\boldsymbol{n})qdS+\int_{\Omega}G_c l\nabla\phi\cdot\nabla q d\Omega \tag{2-60}$$

Now the weak form becomes,

$$\begin{aligned}\int_{\Omega}\left[G_c\frac{1}{l}\phi q+\eta\dot{\phi}q-2(1-\phi)\mathrm{H}^{+}(\boldsymbol{\varepsilon}(\mathrm{t}),\mathrm{c}(\mathrm{t}))q\right]d\Omega-\\ \int_{\partial\Omega}(G_c l\nabla\phi\cdot\boldsymbol{n})qdS+\int_{\Omega}G_c l\nabla\phi\cdot\nabla q d\Omega=0\end{aligned} \tag{2-61}$$

Rearrange equation (2-61) for simpler visualization,

$$\begin{aligned}\int_{\Omega}\left\{\nabla q\cdot\nabla\phi G_c l+\eta\left(\frac{\phi-\phi_n}{\Delta t}\right)q+q\left(\frac{G_c}{l}+2H^{+}\right)\phi-2H^{+}q\right\}d\Omega\\ =\int_{\partial\Omega}(G_c l\nabla\phi\cdot\boldsymbol{n})qdS\end{aligned} \tag{2-62}$$

In the absence of remote tractions and body forces, the resulting weak form of coupled system can be obtained by considering the trial $(u,\ c,\ \phi)$ and test $(\boldsymbol{v},\ \hat{c},q)$ spaces.

Electrochemical:

$$\int_{\Omega}(-K\Omega_c tr\left(\frac{\boldsymbol{\varepsilon}^{el}-\boldsymbol{\varepsilon_n}^{el}}{\Delta t}\right)+\tau\frac{c-c_n}{\Delta t})\hat{c}d\Omega$$
$$-D_0\int_{\Omega}\tau[(1-\phi)^2+\mathrm{k}]\nabla c\cdot\nabla\hat{c}\,d\Omega=\int_{\partial\Omega}\tau D_0\,(\nabla c\cdot\boldsymbol{n})\hat{c}\,dS \tag{2-53}$$

Mechanical:

$$\int_{\Omega}[(1-\phi)^2+\mathrm{k}]\big(\lambda tr\,(\boldsymbol{\varepsilon}-\boldsymbol{\varepsilon}^{ch})\mathbf{1}+2\mu(\boldsymbol{\varepsilon}-\boldsymbol{\varepsilon}^{ch})\big):\nabla v d\Omega=\int_{\partial\Omega}\boldsymbol{t}\cdot\boldsymbol{v}dS \tag{2-55}$$

Phase Field:

$$\int_{\Omega}\{\nabla q\cdot\nabla\phi G_c l+\eta\left(\frac{\phi-\phi_n}{\Delta t}\right)q+q\left(\frac{G_c}{l}+2H^{+}\right)\phi-2H^{+}q\}d\Omega$$
$$=\int_{\partial\Omega}(G_c l\nabla\phi\cdot\boldsymbol{n})qdS \tag{2-62}$$

By taking advantage of the symbolic differentiation capabilities of FENICS [61, 62], the mechanical, electrochemical, and phase field weak forms, i.e., (2-53), (2-55), and (2-62), are directly transferred to the FENICS code. In FENICS, a Function Space is defined on a specific mesh, which is a discretization of the domain of the PDE. A function space can be scalar, dealing with single-valued functions, or vector, dealing with vector-valued functions. This solution algorithm defines the History field, phase field, and chemical field as 1st order (linear) function space with Continuous Galerkin (Lagrange) element. The displacement field is defined as 2nd order (quadratic) function space with a vector element of Continuous Galerkin (Lagrange) type. For the monolithic solution of a coupled system, displacement chemical fields are combined as mixed elements. The mixed element type combines different types of elements into a single function space [61,62]. Triangular mesh is used in the calculation. The combination of quadratic vector element and linear scalar element has 15 Nodes per element (6 nodes per quadratic vector (2D) element component and 3 nodes for linear triangular element).

In the solution algorithm, both the diffusion Eq. (2-53) and the mechanical equilibrium Eq. (2-55) are simultaneously solved for the variables u and c while the phase field state remains fixed. Once the convergence criterion is met, a history variable is computed. This variable retains essential information concerning the phase transition's evolution and defects or cracks within the fiber.

The phase field equation shown in Eq. (2-62) is subsequently solved for the variable ϕ, utilizing the frozen values of c and u, along with the assistance of the history variable. Integrating the history variable into the model enables it to consider the system's previous states and behavior, particularly under electrochemical loading conditions. After the convergence criterion is met, the simulation continues for the next step, see Figure 2.3.

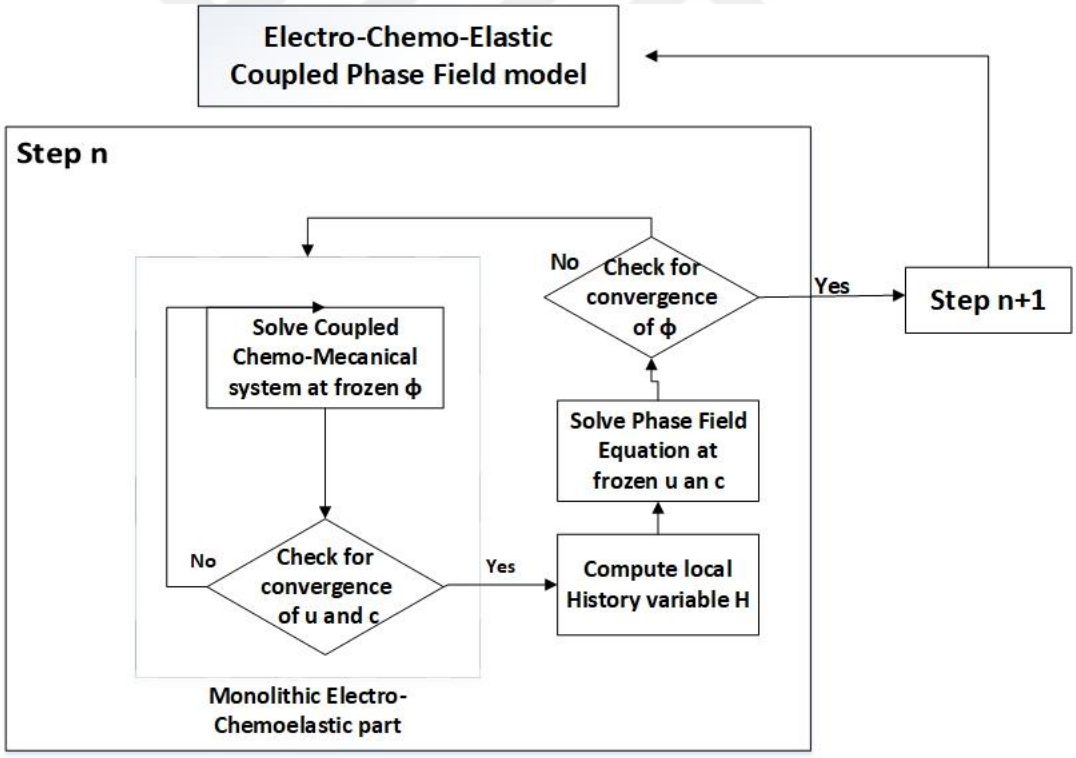


Figure 2.3. Proposed solution scheme for coupled phase field algorithm.

CHAPTER 3

ELECTROCHEMICAL MECHANICAL COUPLING RESULTS

The main idea of this chapter is to present a framework for coupled modeling of a multifunctional composite material, structured on the micro-scale, with the ability to function as a battery cell and carry the mechanical load. The focus is on simulating the electro-chemo-mechanical behavior of the composite structure under different electrochemical states (charging-discharging). Our primary aim is to recreate scenarios from existing research and assess the results side by side. Our overarching goal is to achieve outcomes that closely align with the initial qualitative and quantitative reports. This chapter serves as a critical foundation for the subsequent analysis and conclusions.

3.1 Numerical Examples

3.1.1 Electrochemical-Mechanical Coupling: Example 1

In this example, a square plate is subjected to a chemical load. The coating/matrix region is treated as boundary conditions at the top. Several key assumptions support the solution procedure, including considering isotropic material properties, the assumption of linearity within the coupled system, and adopting a linear constitutive chemical law to govern the material's behavior.

The problem assumes that the plate has no external forces acting on it and is not subject to any surface traction. The plane strain assumption is utilized in this problem. The lower boundary is completely constrained, with no displacement on this side. On the other hand, the remaining sides are free from surface traction. In the y-direction, all nodes are fixed to the lower side of the system, with only the middle node at the lower boundary being fixed in the x-direction. The ionic

concentration is zero at the lower boundary and reaches its maximum at the upper boundary. The ionic concentration is applied at the upper boundary, varying from 0.001 mol/l to 0.01 mol/l (Figure 3.1). The side surfaces are flux-free and traction-free. The material parameters for this model are tabulated in Table 3.1.

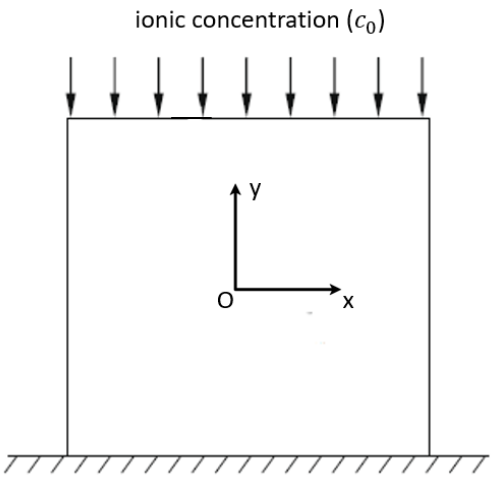


Figure 3.1. Numerical Example-1 Geometry and Boundary Condition. (Yang et al.) [34].

Table 3.1 Material Parameters [34]

	Material parameters	Values
E	Young's modulus	3.5×10^5 Pa
ν	Poisson's ratio	0.45
φ	Diffusion coefficient	7.8×10^{-10} m^2/s
S	Coefficient of the chemical potential	10^3 Nm/mol
R_0	Chemo-mechanical coupling coefficient	1.75×10^4 Nm/mol

Focusing on a single region, the equation sets presented in Yang et al.'s theoretical work are employed [34]. These equations are utilized within a finite element framework to investigate the complex coupled behavior of electro-chemo-

mechanical media. The article explains Gibbs free energy function (Eq. 3-1) and constitutive equations (Eq. 3-2 and 3-3).

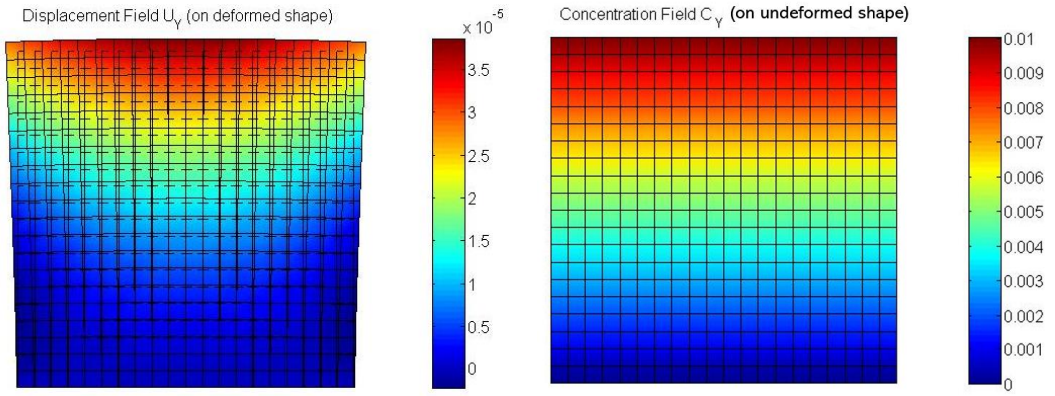
$$g = \frac{1}{2}(\sigma_{ij}\varepsilon_{ij} - \sum_{\alpha=+,-} \mu^{\alpha}c^{\alpha}) = \frac{1}{2}C_{ijkl}\varepsilon_{kl}\varepsilon_{ij} - \sum_{\alpha=+,-} R_0^{\alpha}c^{\alpha}\varepsilon_{ij} + \frac{1}{2}\sum_{\alpha=+,-} S^{\alpha}c^{\alpha}c^{\alpha} \quad 3\text{-}1$$

$$\sigma_{ij} = C_{ijkl}\varepsilon_{ij} - \sum_{\alpha=+,-} R_0^{\alpha}c^{\alpha} \quad 3\text{-}2$$

$$\mu^{\pm} = -R_0^{\pm}\varepsilon_{kl} + S^{\pm}c^{\pm} \quad 3\text{-}3$$

The equation set resembles the one derived in Chapter 2, with the main differences being that the paper [34] defines chemo-mechanical coupling and chemical coefficients for constitutive equations and specifies these constants for negative and positive ions (Table 3.1). However, they assumed the same values for the positive and negative ions in numerical examples. Also C_{ijkl} is the elastic modulus tensor, which is derived from Young's modulus (E) and Poisson's ratio (ν) for isotropic materials.

To simulate diffusion in the fiber region, a simplified geometry based on the electrochemical-mechanical coupling model outlined in the reference paper by Yang et al. is implemented and solved [34]. The upper boundary experiences the most notable swelling due to the distribution of linear ionic concentration, while there is no apparent swelling at the lower boundary. The symmetric deformation in the x-direction arises from the model's symmetry and the applied load (Figure 3.2). Chemical swelling of the medium is very similar to heat expansion, where pure volume expansion is produced under thermal load.



(a) (b)

Figure 3.2. (a) The y-displacement results of the present study on the deformed shape of the body (b) Ionic concentration distribution on the undeformed shape of the body

3.1.2 Electrochemical-Mechanical Coupling: Example 2

Another example of testing the coupled system is a single fiber with a radius r in a 2D plane strain setting, modeled as shown in Figure 3.3. The circular domain mimics the fiber domain, and the loading scenario refers to the charging state. The ionic concentration is applied linearly to the outer boundary up to 1 mol/l with a concentration of zero at the initial state and reference ionic concentration $c_0 = 0.0001$ mol/l. Pressure is applied to the outer surface to prevent the body's rotation and translation, which is very small compared to chemical stresses. The fiber model shown in Figure 3.3 contains no internal damage mechanisms and is utilized for calculating ion concentration and stress distributions. The material parameters for this model are tabulated in Table 3.2. The constitutive relations are explained in Chapter 2 with all the derivation procedures. The free energy function and governing equations are rewritten as follows.

$$g = \frac{1}{2}\left(\lambda[tr(\boldsymbol{\varepsilon} - \boldsymbol{\varepsilon}^{ch})]^2 + 2G\, tr[(\boldsymbol{\varepsilon} - \boldsymbol{\varepsilon}^{ch})^2]\right) + \mu_0 c + \frac{RT}{2c_0}c^2 \tag{2-27}$$

$$\boldsymbol{\sigma} = \partial_{\varepsilon} g = \lambda tr\left(\boldsymbol{\varepsilon} - \boldsymbol{\varepsilon}^{ch}\right)\mathbf{1} + 2\mu\left(\boldsymbol{\varepsilon} - \boldsymbol{\varepsilon}^{ch}\right). \tag{2-16}$$

$$\mu = -K\Omega_c tr\left(\boldsymbol{\varepsilon} - \boldsymbol{\varepsilon}^{ch}\right) + \mu_0 + \frac{RT}{c_0} c. \tag{2-22}$$

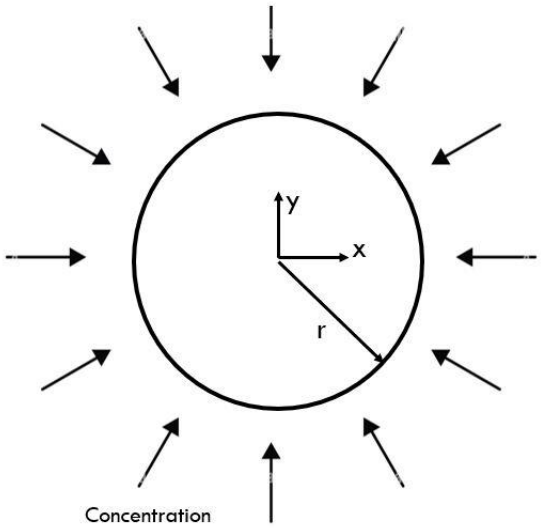


Figure 3.3. Numerical Example-2 geometry and Boundary conditions (Klinsmann et al. [35]

Table 3.2 The material parameters

Material parameters		Values	Ref.	Material parameters		Values	Ref.
E	Young's modulus	9.3 GPa	[44]	D_0	Diffusion coefficient	7.8×10^{-15} m^2/s	[46]
ν	Poisson's ratio	0.3	[44]	G_c	Critical energy release rate	$10\, J/m^2$	[35]
ρ	Density	530 kg $/m^3$	-	Ω_c	Molar volume of Li	3.497×10^{-6} m^3/mol	[45]

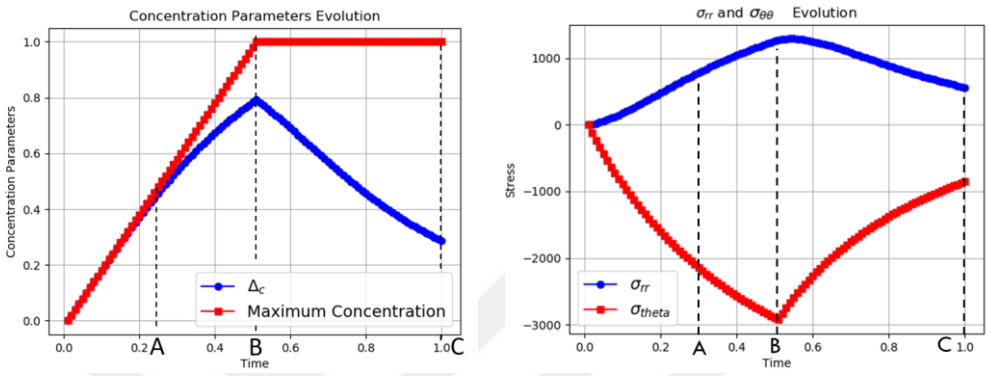
This part aims to calculate the stress distributions in the circular domain and predict the critical time intervals that trigger the potential damage mechanisms. For this purpose, the ionic concentration difference with respect to time is calculated. The

proposed algorithm controls the concentration rate over time with a linearly increasing concentration. First, the concentration is linearly increased to the maximum concentration value ($1\ \mathrm{mol/l}$) up to time $0.5t_{max}$. Once it reaches the maximum value, a constant concentration is maintained up to time t_{max} (as indicated by the red curve in Figure 3-4(a)) [58]. This scenario involves a controlled concentration gradient, which is more aligned with a concentration-driven diffusion process. This setup is suitable for modeling systems where the concentration is the primary controlled variable, reflecting diffusion processes under a concentration gradient rather than strictly under constant current (galvanostatic) or constant voltage (potentiostatic) conditions.

Additionally, we calculate the concentration difference within the fiber (Δc) during the loading process, as shown by the blue curve in Figure 3-4(a).

The role of concentration difference in generating mechanical stress becomes obvious when comparing the concentration difference values in Figure 3.4. (a) with the maximum values of radial and circumferential stresses at corresponding time steps in Figure 3.4. (b). The graph depicting the highest magnitude of maximum stresses over time is directly correlated with the time history of the maximum concentration difference Δc. The concentration difference and mechanical stresses both exhibit peaks simultaneously. In their study, Klinsmann et al. also show the relation between ionic concentration diffusion and maximum principal stresses [35]. Due to limited diffusivity, a significant concentration difference develops, leading to higher maximum principal stress in the particle. When there is a significant concentration difference, the outer part of the fiber expands more than the interior. This results in the fiber being stressed in two directions: it stretches radially, causing tensile stress, and compresses circumferentially, leading to compressive stress in the outer region of the fiber. As the diffusion process ends, the concentration difference and all associated mechanical stresses gradually decrease.

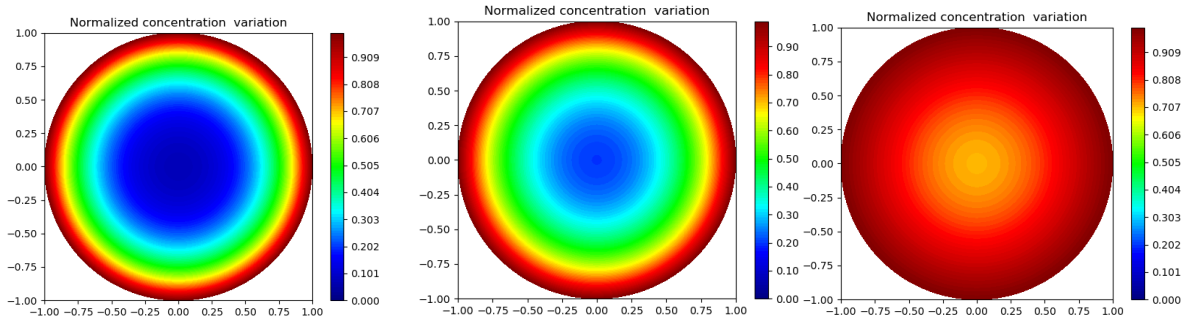
Figure 3-5 presents the ionic concentration distributions at three different time steps relative to the loading curve in Figure 3-4 (a). Lithium ions penetrate the region very close to the fiber's surface at the onset of ionic diffusion. The fiber concentration is highest at the surface and gradually decreases towards its center, where the ionic concentration is almost negligible.



(a) (b)

Figure 3.4. (a) Loading condition and concentration difference Δc (b) The highest value of the radial stress and the highest values of circumferential stress for time

The maximum value of (Δc) is observed at $0.5t_{max}$ when the surface concentration reaches its peak. After this point, i.e., $t > 0.5\ t_{max}$, the outer concentration value is kept constant, and Li ions migrate to the inner part of the fiber. At the end of the diffusion process, the concentration gradient and Δc decline, see Figure 3-5 (c). Empirical evidence suggests that the maximum concentration difference occurs when the outer surface reaches its peak value. Moreover, diffusion within the body towards the center reduces concentration differences under constant concentration boundary conditions. Furthermore, prolonged simulation durations result in the body's concentration reaching equilibrium with the outer boundary [58].



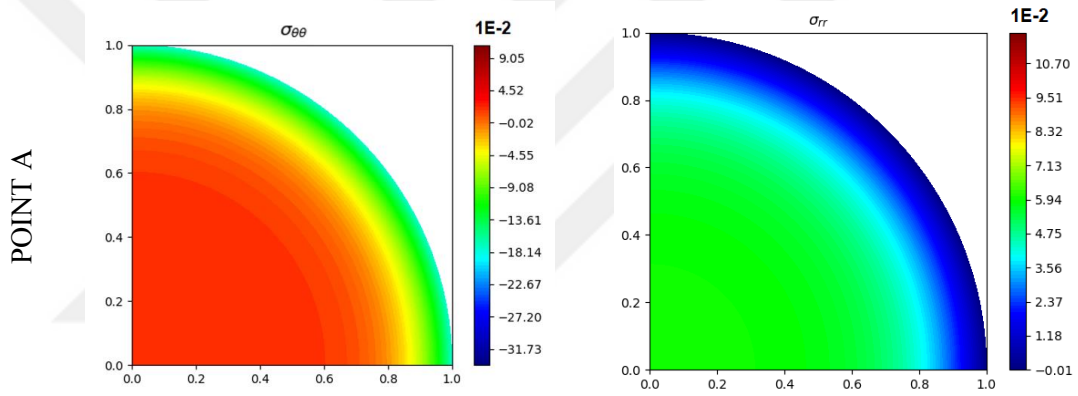
(a) (b) (c)

Figure 3.5. Ionic concentration distribution at three different time steps (a) A ($0.25t_{max}$), (b) B ($0.5t_{max}$) (c) C (t_{max})

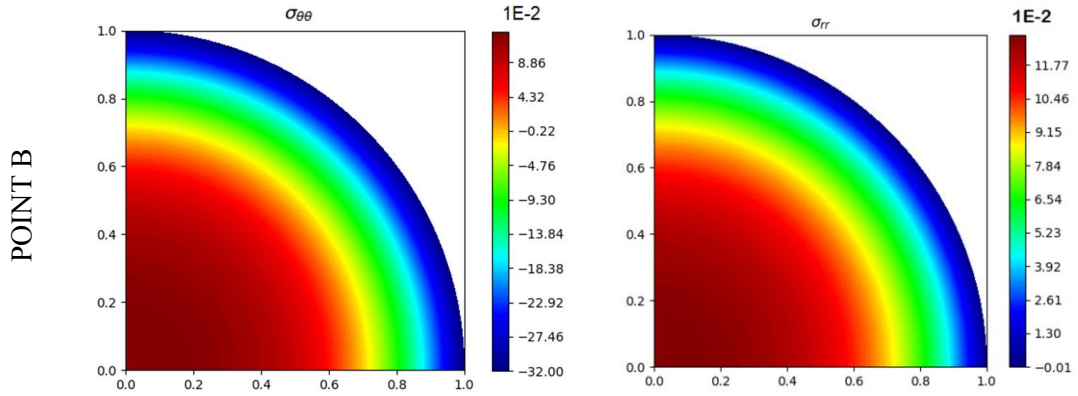
The circumferential and radial stress distribution in the first quadrant of the body for Point A ($0.25t_{max}$), Point B ($0.5t_{max}$) and Point C (t_{max}) are illustrated in Figure 3.6 relative to the loading curve in Figure 3-4 (b). Due to the concentration gradient, the outer part of the fiber expands more. This expansion leads to the development of internal stresses within the fiber. As a result, radial stresses (σ_{rr}) are positive everywhere, as the outer region attempts to expand more and applies radial tractions to the inner part while being zero at the outer surface. On the other hand, circumferential stresses ($\sigma_{\theta\theta}$) are negative in the outer region and positive in the inner region. This is because the outer region's expansion in the circumferential direction is constrained by the inner region, which does not expand as much due to its lower concentration of ions. The radial and circumferential distributions observed in this work are similar to those found by Varna et al. [33].

In point A, the lithium ions diffuse towards the outer region close to the fiber surface. Numerically, the fiber has not reached the maximum stress values. Figuratively, the gradient is very close to the fiber surface (Figure 3.6 (a)). In point B, the fiber exhibits the highest concentration difference. The lithium ions have diffused throughout the fiber, resulting in a significant ionic concentration gradient. The stress values within the fiber have reached their peak, indicating a substantial mechanical response due to the high ionic concentration gradient (Figure 3.6 (b)).

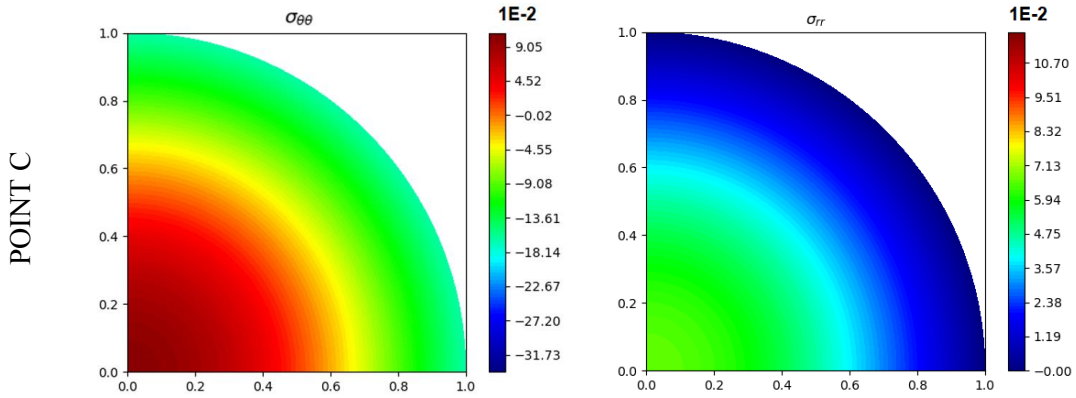
This distribution suggests that the fiber is under significant mechanical stress, particularly near the outer regions where the concentration gradient is steepest. At point C, the body is in a relaxation state. This results in a more uniform distribution of lithium ions across the fiber, as depicted by the smoother and more consistent color gradient from the core to the surface (Figure 3.6 (c)). The fiber's stress values are lower than at point B, reflecting the reduced mechanical strain due to the stabilized ionic concentration. When comparing three different points, point B represents the most critical moment in the fiber, as it exhibits the highest concentration difference and maximum stress, indicating the peak mechanical and chemical loading conditions within the fiber.



(a)



(b)



(c)

Figure 3.6. Circumferential and radial stress distributions at (a) Point A ($0.25t_{max}$), (b) Point B ($0.5t_{max}$), (c) Point C (t_{max})

CHAPTER 4

ELECTROCHEMICAL MECHANICAL PHASE FIELD COUPLING RESULTS

This chapter presents the results of coupling the phase field with the electro-chemo-mechanical framework presented before. To this end, different geometries and crack configurations are studied, focusing on their implications for crack initiation and propagation. Initially, we explore the coupling of phase field with a mechanical problem in a single-edge notched specimen to understand the purely mechanical aspects of crack growth. The phase-field method is used to represent the fracture process. This approach smoothly transitions between damaged and undamaged states, avoiding the need for explicit crack tracking [70]. This is later extended to include electrochemical effects, examining how ionic diffusion influences stress distributions and crack propagation in the same geometry. The study then examines crack propagation behavior in circular fibers under electrochemical loading conditions. We analyze three distinct crack configurations: a central crack, an arc crack, and a T-crack. We investigate the stress distribution and crack growth behavior for each configuration, highlighting each crack type's unique characteristics and propagation mechanisms. The goal is to clarify the coupled relationship between electrochemical and mechanical factors influencing crack behavior.

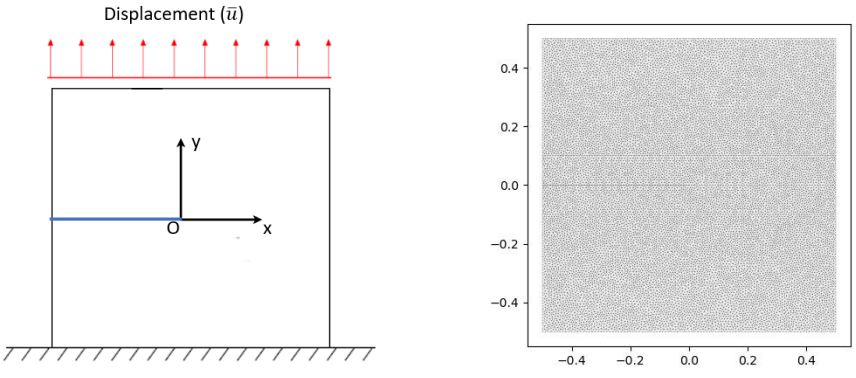
4.1 Mechanical Phase Field Coupling: Single Edge Notched Specimen

The simulation of crack propagation in solid materials is challenging when dealing with sharp cracks, as modeling the propagation of complex crack patterns is difficult. Researchers have used a diffusive crack modeling approach with phase-field modeling to address this [38, 40, 41, 48]. Miehe et al. [48] introduced a variational framework for modeling rate-independent diffusive fractures,

incorporating a local history field and monolithic Newton-type solvers. This approach and a semi-implicit finite element algorithm demonstrated robustness in solving the regularized dissipation function and balance equation. Further advancements by Miehe et al. [38] included a strain history source term for a staggered approach, enhancing the stability of post-critical solution paths through viscous regularization. Initial studies focused on pure mechanical loading. Benchmark tests, including tensile and shear load scenarios, validated these methods. The current study utilized the FENICS [61, 62] program and the solution algorithm described in Chapter 2. Identical numerical examples from the literature were used to compare the effects of viscous regularization and monolithic-staggered algorithms on load-deflection curves and to test the code.

4.1.1 Geometry, Boundary Conditions, and Study Parameters

A tensile loading is applied to a single-edge notched specimen (1mm×1mm) with a crack of 0.5mm in the middle. A prescribed remote displacement boundary condition ($\dot{u}$=0.0007 mm/s) is enforced on the upper surface while the bottom of the plate is clamped. The side surfaces are traction-free; see Figure 4.1(a). For the simulations, triangular mesh is used (Figure 4.1(b)). The material parameters used in this example are shown in Table 4.1. [38].



(a) (b)

Figure 4.1. Single-edge-notched specimen: (a) Geometry and boundary conditions (Miehe et al. [38]), (b) Mesh structure

Table 4.1 The material parameters used in single-edge-notched specimen. (Miehe et al. [38])

Material parameters		Values
E	Young's modulus	210 GPa
ν	Poisson's ratio	0.3
G_c	Critical energy release rate	2.7 MPa

4.1.2 Mechanical-Phase Field Coupling Results

The computational simulation of crack propagation in solid materials often involves sharp cracks that are unsuitable for representing complex crack patterns. To address this issue, researchers in the literature have adopted a diffusive crack modeling approach, utilizing phase field modeling. In a notable reference paper by Miehe et al. [48], they introduced an innovative variational framework for modeling rate-independent diffusive fracture. This framework incorporates the concept of a local history field and employs monolithic Newton-type solvers to solve the regularized dissipation function and the balance equation in a coupled manner. The proposed semi-implicit finite element algorithm in [54], featuring discretization of the pressure field as an independent variable and monolithic update scheme for concentration and deformation fields, also demonstrated robustness.

Miehe et al. [38] introduced a more robust algorithm that presents the balance equation for the phase field evolution, including a strain history source term. This modification allows for a staggered approach to solving the two-field problem. This revised formulation leads to two linear problems for sequentially updating the phase and displacement fields within a typical time step. In both studies, [48] and

[38], they adopted viscous regularization to enhance the stability of post-critical solution paths. To evaluate the numerical modeling capabilities, they conducted tests using benchmark problems, including a single-edge notched specimen exposed to both tensile and pure shear loads. The same staggered phase-field fracture algorithm was implemented in FENICS [61, 62] by Martinez-Paneda [40]. In [40], the numerical results were compared with [38], and the details of the FENICS [61, 62] implementation were explained.

In this section, the same numerical example shown in Figure 4.1 is used for comparison. The effect of viscous regularization on load-deflection curves and the comparison of monolithic-staggered algorithm results are also discussed in this section. Different simulations are performed to point out the effects of the length scale parameter l and viscosity η. For the fixed length scale parameter, the influence of viscosity is analyzed. First, staggered solution schemes are compared for l=0.015 mm. Figure 4.2 depicts the load-deflection curves. Solid lines correspond to the current results, while markers are discretized results from Miehe [48]. A very good agreement with the literature is observed. The maximum loads and the post-crack critical regimes are almost identical.

It can be noted that in cases where η=0 Ns/m^2, the structural response exhibits a sharper decline, whereas including the viscous model results in a more gradual and controlled crack propagation during the post-critical phase. Importantly, the introduction of viscous regularization does not alter the maximum load capacity but significantly affects the stability of crack propagation after reaching the peak load.

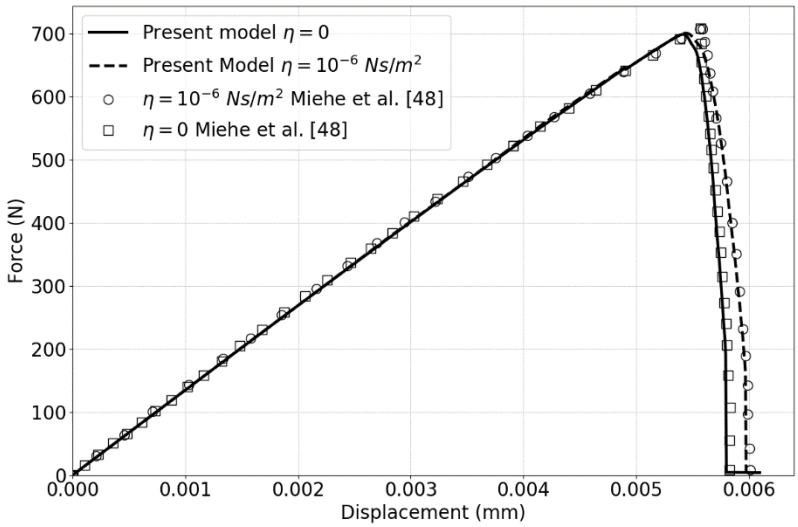


Figure 4.2. The comparison of load-deflection curves with Miehe [48] results in a length scale l=0.015 mm

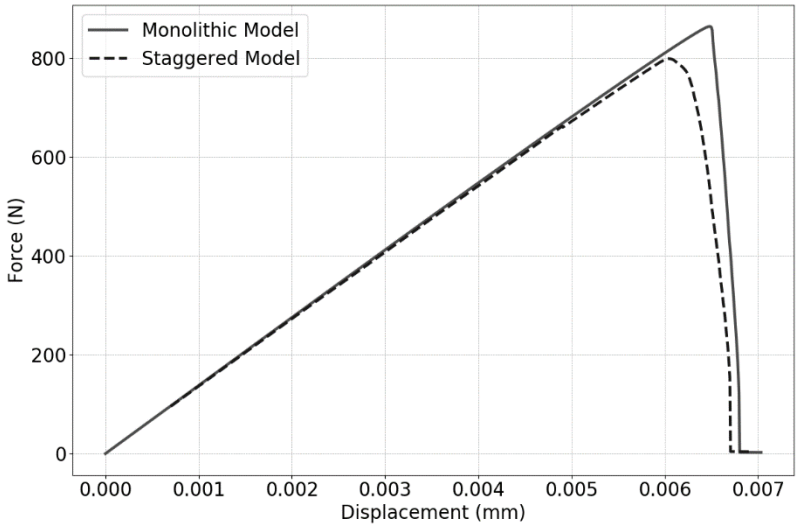
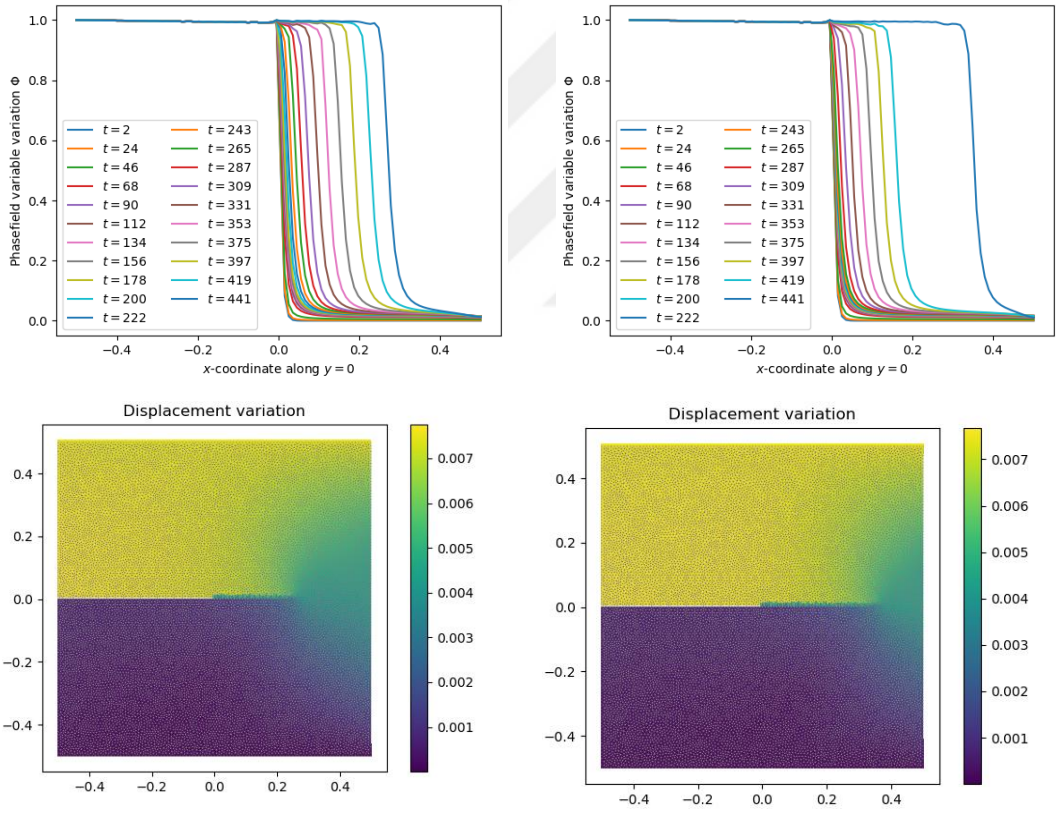


Figure 4.3. The comparison of load-deflection curves of monolithic and staggered solutions

Next the monolithic and staggered approaches are compared for the same model. The load-displacement curves are depicted in Figure 4.3. As the displacement increases, both models show a linear increase in force, which suggests an elastic response where the force is directly proportional to the displacement. The monolithic model predicts a higher ultimate load that can be sustained and a steeper

post-peak response, while the staggered solution gives a lower ultimate load and a more gradual post-peak curve.

The variation of the phase field variable parallel to the crack tip (parallel to the x-axis, along $y = 0$) is plotted for different time steps during crack propagation in Figure 4.4. Here, $\phi = 0$ denotes intact material, while $\phi = 1$ represents the fully broken material state. The same time increment and total time are used to solve the model problem with staggered and monolithic algorithms. The crack propagation is faster in the staggered solution than in the monolithic case. In Figure 4.4, the crack is captured with displacement vector norm at the last time step ($t_{max}/\Delta t = 441$). The crack length looks different when the two cases are compared.



(a) (b)

Figure 4.4. The comparison of phase field variation through the crack surface and crack pattern at the final state of simulation for (a) monolithic solution and (b) staggered solution.

4.2 Electrochemical Mechanical Phase Field Coupling: Single-Edge Notched Specimen

4.2.1 Geometry, Boundary Conditions, and Study Parameters

In this section, the aim is to use chemo mechanical-phase coupling with standard geometry. This section serves as a verification for the proposed solution scheme using a simple and standard geometry.

This standard testing has previously been discussed in the context of thermo-mechanical coupling. Analogies of ionic diffusion and heat conduction [34] transfer knowledge to chemo-mechanical and phase field coupling. The thermo-elastic results [47, 3] were compared with those obtained from the FENICS [61, 62] software. The thermomechanical results are not included in this section as they are beyond the scope of this thesis. However, the knowledge gained from the thermo-elastic case was used to model crack formation in a single-edge notched specimen under chemical and mechanical loading. The crack propagation results for chemo-mechanical loading are discussed in this section. The material parameters are like the uncracked square specimen in Chapter 3 (Table 3.1).

A tensile loading is applied to a single-edge notched specimen (1mm×1mm) with a crack of 0.5mm in the middle. The same mesh structure shown in Figure 4.1 is used in this section. A prescribed remote displacement boundary condition ($\dot{u}$=0.0007 mm/s) is enforced on the upper surface, while the bottom of the plate is clamped; see Figure 4.5. The side surfaces are both traction-free and flux-free. On the upper surface, an ionic concentration boundary condition ($\dot{c}$=10^{-4} mol/Ls) is applied. On the lower surface, the concentration is prescribed as zero. Both mechanical and chemical loading gradually increase with time. Along the initial crack path (blue line in Figure 4.5), the phase field parameter is set to 1. The chosen phase field parameters are as follows: The length scale parameter l is 0.015

mm or 0.0075 mm; the element size is chosen such that $h \leq l/2l$, and the viscosity parameter $\eta = 1 \times 10^{-6}$ kNs/mm^2

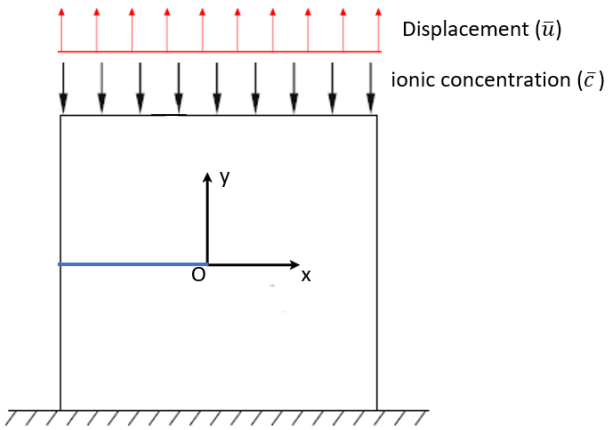


Figure 4.5. Single-edge-notched specimen geometry and boundary conditions.

4.2.2 Electrochemical-Mechanical-Phase Field Coupling Results

This section uses an electrochemical mechanical formulation to integrate the phase field algorithm into the coupled system. The objective is to examine the impact of electrochemical loading on crack propagation within a single edge-notched specimen subjected to combined electro-chemo-mechanical loading.

Several important findings emerged from our analysis. Firstly, we observe a great difference in ionic concentration on the upper and lower surfaces of the crack (Figure 4.6). This difference underscores the influence of crack morphology on ion transport within the fiber, affecting the electrochemical performance of the system. Furthermore, the orientation of the crack, perpendicular to the direction of ionic diffusion, leads to the blockage of ion transport across the body. This blockage significantly affects how electrochemical processes behave, demonstrating how crack propagation can significantly influence the performance of the structural battery.

Lastly, apply the phase field parameter, with a value of 1 assigned to the crack surface and 0 everywhere else. The variation of the phase field variable parallel to

the crack tip (parallel to the x-axis, along $y = 0$) is plotted for different time steps during crack propagation (in the right column of Figure 4.6.). A remarkable agreement with the actual crack propagation process is compelling evidence of the compatibility and accuracy of the phase field equation set when coupled with the electrochemical equations, effectively capturing the dynamics of crack initiation and propagation in the presence of electrochemical forces.

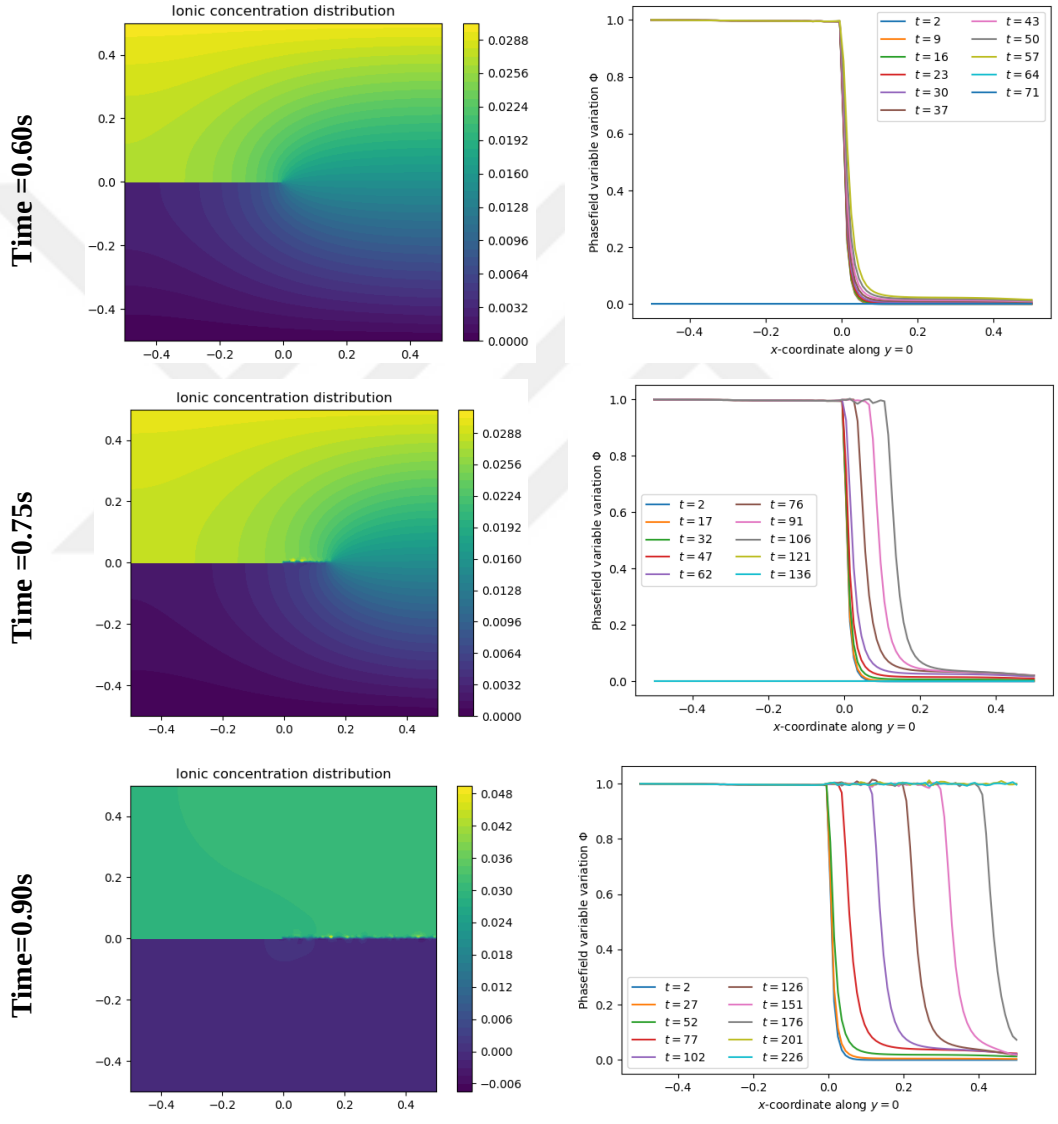


Figure 4.6. The crack propagation with respect to phase field distribution on the crack surface for different time intervals

4.3 Electrochemical-Mechanical-Phase Field Coupling: Crack Propagation in Circular Fiber

In the preceding chapter (Section 3.1.2), we explored the relationship between the evolving pattern of maximum concentration difference (Δc) and the graph depicting the highest values of radial and circumferential stresses over time (Figure 3.5). As Li diffusion rate takes precedence, elevated mechanical stresses are expected. This analysis also helps identify two critical regions within geometry.

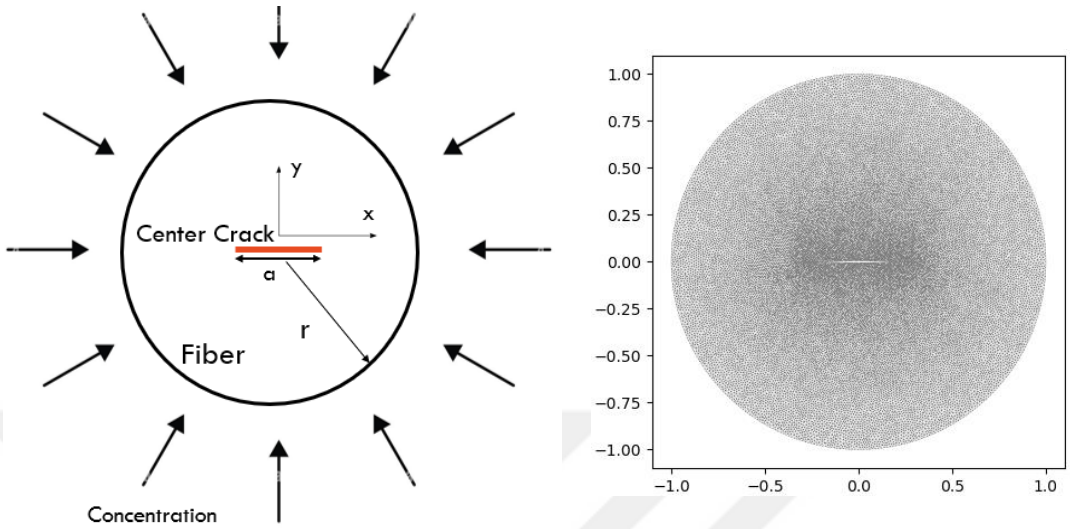
Due to the concentration gradient, the outer section of the fiber experiences more significant free swelling strains than the inner region during charging [33, 35]. Radial stresses are positive at the center because the outer portion expands further and exerts radial tractions on the inner part. Conversely, hoop stresses are negative in the outer region and positive in the inner region. This happens because the outer region tries to expand in the direction of θ, the inner region, with a lower ionic concentration level, does not expand as much. These observations highlight the potential for two distinct types of damage: surface crack mechanisms near the fiber surface and central cracks positioned at the fiber's symmetry plane. In this section, we investigate these crack mechanisms.

4.3.1 Circular Fiber with Central Crack

4.3.1.1 Geometry and Boundary Conditions (Central Crack)

We model a single fiber with a radius r in a 2D plane strain setting to simplify the study and obtain general results. We also incorporate possible initial cracks of length a into the structure (Figure 4.7(a)). The ionic concentration is applied to the outer boundary, ranging up to 1 mol/l, with a zero concentration at the initial state and reference ionic concentration $c_0 = 0.0001$ mol/l. The diffusion problem with the center crack is modeled to discuss the effect of the electrolyte during the charging state with different initial crack lengths and loading rates ($\dot{c}$). The

triangular mesh structure is used in simulations with a physical crack in the body (Figure 4.7(b)).



(a) (b)

Figure 4.7. (a) Geometry and boundary conditions for the Li intercalation fiber with a central crack, (b) Mesh structure of fiber with a crack length $a = 0.6\,m$

The material parameters are selected for Li and the fiber, as shown in Table 3.2. This material's critical energy release rate is consistent with the range of experimental results, and the temperature is adjusted to match the room temperature [44]. Table 4.2 shows four different crack lengths, and four different loading rates used in simulations.

Table 4.2 The material parameters used in the center crack numerical examples.

Crack length $\boldsymbol{a}$ $(\boldsymbol{m})$	Charging rate $\dot{\boldsymbol{c}}$ (mol/Ls)
0.1	0.0003
0.2	0.0005
0.4	0.0007
0.6	0.001

4.3.1.2 Numerical Results (Central Crack)

Section 3.1.2 depicts a circular-shaped fiber subjected to chemical loading with the same procedure and boundary conditions. The additional crack parameters for the center crack are summarized in the previous section. The impact of varying ionic concentration loading rates, ranging from 0.0003 mol/Ls to 0.001 mol/Ls, are studied to understand the initiation and development of cracks. The ionic concentration linearly increases over time $t = 0.5t_{max}$. Upon reaching this peak level, it remains constant until $t = t_{max}$.

In Klinsmann's work, flux BC is applied, which is analogous to the operation of constant current constant voltage (CCCV) [57]. This involves two consecutive steps: constant current (galvanostatic) and constant voltage (potentiostat). The first step involves galvanostatic charging, where a constant current is applied until the concentration reaches a minimum value. The second step is potentiation, where the concentration is constant [57].

As explained before, in the proposed solution, the concentration is linearly increased over time up to a certain value (i.e., normalized concentration is equal to 1), which implies a controlled rate of increase in ionic concentration, simulating a more gradual charging process where the concentration at the boundary changes linearly with time. Then, the concentration is kept constant after it reaches the maximum value. This is similar to the potentiostatic phase, where the concentration is maintained at a specified value once the target concentration is achieved. Both boundary conditions aim to simulate charging/discharging a structural battery component (either fiber or active material) by controlling the concentration at the surface.

To understand the relationship between concentration difference and stress distributions during this loading regime, we have chosen one of the test cases without crack propagation. This case involves a fiber with a crack length of $a =$

0.1 m and a charging rate of $\dot{c} = 0.0003$ mol/Ls. The results for this test case are presented and explained in Figures 4.8 and 4.9.

Furthermore, the maximum difference in concentration within the fiber (Δc) throughout the loading process is computed, illustrated by the blue curve in Figure 4.8 (a). Figure 4.8 (c) shows the distribution of ionic concentrations at three distinct time steps during charging. Initially, as ionic diffusion begins, lithium ions diffuse the area near the fiber's surface. During this phase, the fiber shows a high concentration gradient at its surface, whereas the ionic concentration near the center of the fiber is almost negligible.

Results presented in Figure 4-8 reveal that the ion concentration within the system changes progressively from an initial value of $t_0 = 0$ to maximum value t_{max} over a specific period. This transition happens between the initial time (t_0) and halfway of the maximum time ($0.5t_{max}$). The concentration increases steadily until it reaches the midpoint of the maximum time. The maximum value of concentration difference is observed at $0.5t_{max}$ when the outer concentration peaks. As the ionic concentration of the outer surface is kept constant from $0.5t_{max}$ to t_{max}, Li ions migrate to the inner part of the fiber. At the end of the diffusion process, the concentration gradient declines; see Figure 4-8 (c) Ponit C.

As mentioned in the preceding chapter, the graph illustrating the highest values of radial and circumferential stresses over time is closely connected to the changing pattern of the maximum concentration difference, Δc; see Figure 4-8 (b). The maximum concentration difference and the stress components exhibit peaks simultaneously. When the rate of lithium diffusion takes precedence, we expect increased mechanical stress.

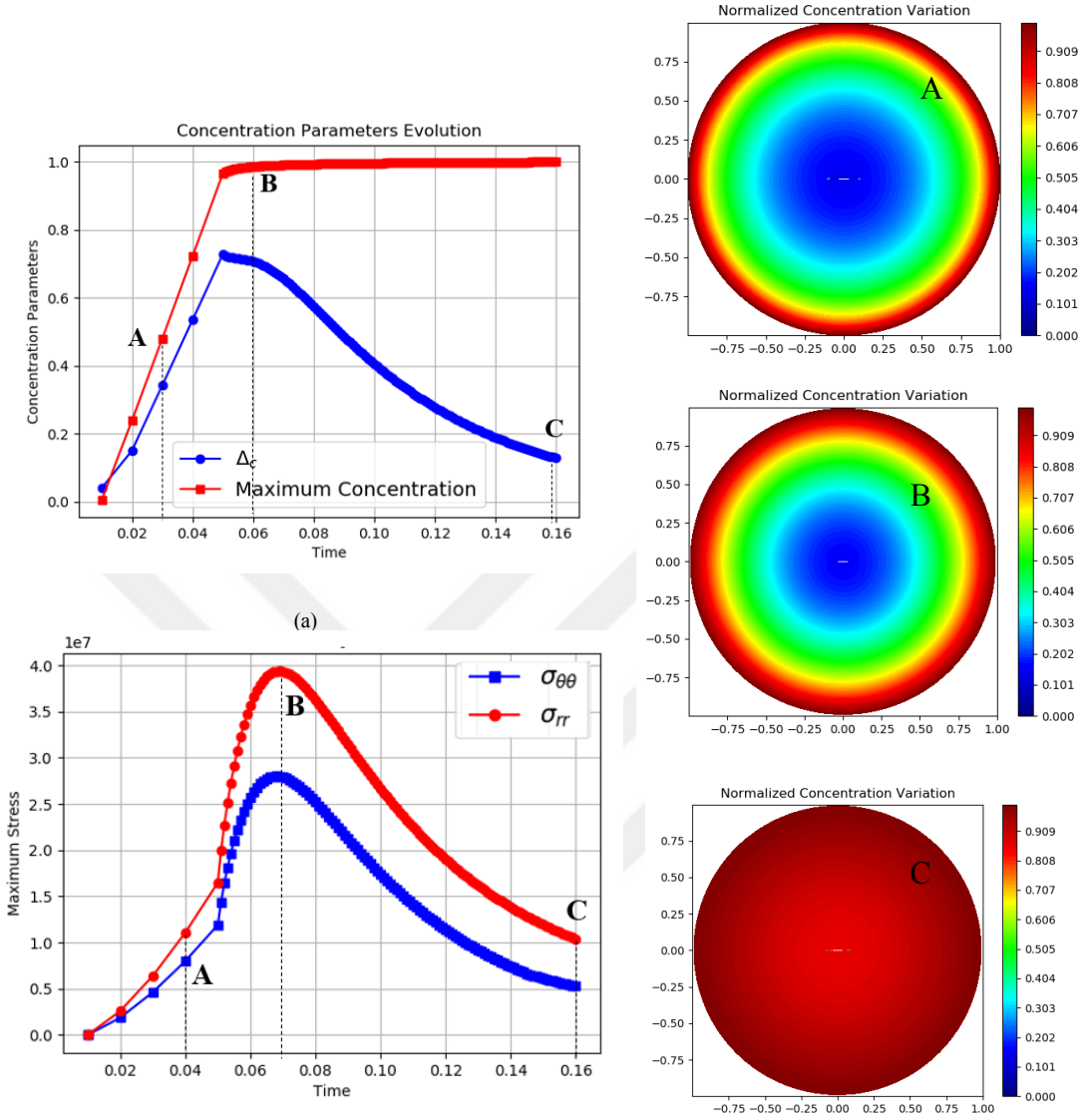
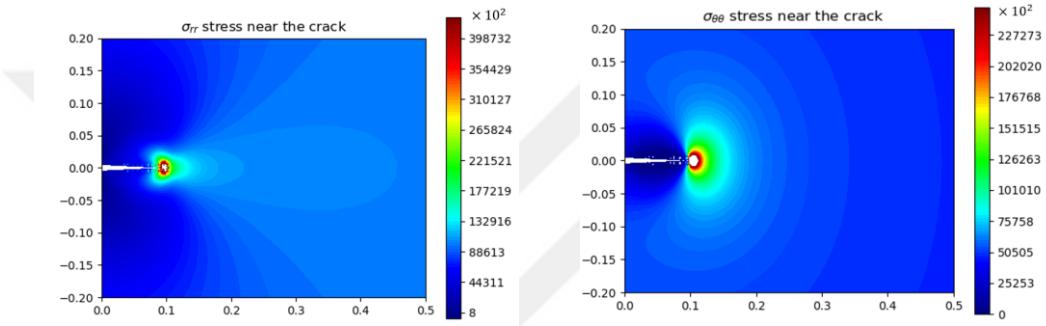


Figure 4.8. (a) Loading condition and maximum concentration difference Δc. (b) The maximum values of the radial and circumferential stress components with time. (c) Ionic concentration distribution at three different time steps: A at $t = 0.3t_{max}$, B at $t = 0.5t_{max}$, and C at $t = 1.5t_{max}$

The highest positive radial and circumferential stresses are located at the crack tips (Figure 4-9 (a) and (b)). These stresses situated at the crack tips serve to promote the initiation and advancement of the crack. If the stress intensity at the crack tip

exceeds a critical threshold, it can trigger and facilitate the further propagation of the crack within the fiber shown in upcoming sections [67]. If the crack fails to propagate at the point of maximum concentration difference, it remains inactive and does not propagate in subsequent instances. In such cases, when the outer surface is exposed to a constant maximum ionic concentration, ions start to diffuse the inner parts of the fiber (Figure 4-8 (c)), and relaxation processes begin (Figure 4-8 (b)). The crack does not propagate for this crack geometry when the ionic concentration loading rate $\dot{c}$ is less than 0.0003 mol/Ls.



(a) (b)

Figure 4.9. (a) Radial stress distribution corresponding to maximum concentration difference (point B) (b) Circumferential stress distribution corresponding to maximum concentration difference (point B)

Table 4.3 lists the various test cases considered to analyze crack propagation in the specimen. Four different crack sizes and four different loading rates are listed. The initial crack length characterizes each test case (a) and the rate of concentration change ($\dot{c}$) The crack propagation and branching information are also listed in Table 4.3. For $a = 0.1$ m, the crack needs high loading rates for propagation; with slower loading rates, the formation of new crack surfaces does not start up from the crack tips even when the outer boundary reaches maximum concentration, and entirely new cracks may form from the outer boundary. This type of crack formation is not considered a physically sound crack formation mechanism. Because of this, an additional loading rate is used for $a = 0.1$ m (Test case A*).

The lower limit is chosen as $\dot{c} = 0.0003$ mol/Ls because no crack propagation occurs in all the crack lengths. The upper limit is chosen as $\dot{c} = 0.001$ mol/Ls.

Table 4.3 The test case details and crack conditions in numerical examples.

Case	Crack length $a\ (m)$	Charging rate $\dot{c}$ (mol/Ls)	Crack propagation	Branching at the onset of propagation.
A1	0.1	0.0003	No	N/A
A2	0.1	0.0005	No	N/A
A3	0.1	0.0007	No	N/A
A*	0.1	0.0008	Yes	Yes
A4	0.1	0.001	Yes	Yes
B1	0.2	0.0003	No	N/A
B2	0.2	0.0005	Yes	Yes
B3	0.2	0.0007	Yes	Yes
B4	0.2	0.001	Yes	Yes
C1	0.4	0.0003	No	N/A
C2	0.4	0.0005	Yes	No
C3	0.4	0.0007	Yes	No
C4	0.4	0.001	Yes	No
D1	0.6	0.0003	No	N/A
D2	0.6	0.0005	Yes	No
D3	0.6	0.0007	Yes	No
D4	0.6	0.001	Yes	No

The investigation focuses on determining the maximum radial and circumferential stresses occurring at the crack tip before crack propagation. Table 4.4 presents the maximum radial (σ_{rr}^{max}) and circumferential ($\sigma_{\theta\theta}^{max}$) stresses observed at the onset of crack growth in each scenario. Comparative evaluations are conducted across various crack sizes and loading rates. The findings consistently reveal that across

all scenarios culminating in crack growth, the maximum circumferential stresses exceed the radial stresses, albeit remaining within the same order of magnitude. This behavior is indeed expected as the cracks mostly propagate in Mode-I. Moreover, it is observed that enlarging the crack size for identical loading rates and fiber radius reduces the maximum stresses. This trend suggests a significant influence of crack size on stress distribution, indicating that larger cracks experience lower stress concentrations than smaller ones under similar loading conditions.

Table 4.4 The maximum radial and circumferential stresses at the onset of crack propagation

Testcase	Crack length $a\ (m)$	Charging Rate $\dot{c}$ (mol/Ls)	σ_{rr}^{max} (MPa)	$\sigma_{\theta\theta}^{max}$ (GPa)
A*	0.1	0.0008	400	900
A4	0.1	0.001	400	850
B2	0.2	0.0005	100	175
B3	0.2	0.0007	100	175
B4	0.2	0.001	300	600
C2	0.4	0.0005	150	270
C3	0.4	0.0007	270	350
C4	0.4	0.001	190	390
D2	0.6	0.0005	125	285
D3	0.6	0.0007	105	250
D4	0.6	0.001	135	280

In addition, the study compares different crack sizes under the same charging conditions. It notes that smaller crack sizes require more energy to initiate crack propagation. Consequently, larger maximum radial and circumferential stresses are observed before crack propagation onset in cases of smaller crack sizes. However,

if the concentration difference resulting from the applied concentration to the outer boundary does not meet the high-stress requirements, crack propagation does not occur.

In the simulations, crack branching is also observed in some cases. When the crack is smaller, branching happens in a single time step without having a mode-I crack propagation, showing that the particle has accumulated more energy to initiate branching rather than self-similar propagation. This pattern is consistent across all loading rates. On the other hand, when the initial crack size is larger, mode-I propagation occurs first, and branching is observed later.

The reason for branching is the increased velocity of the crack tip. This acceleration occurs due to the crack traversing regions of high tensile stress over a longer distance, thereby gaining momentum [63, 64]. Additionally, a smaller initial crack length to fiber radius ratio causes the crack to propagate later when more elastic energy is stored in the particle (Klinsmann et al. [35]). This delayed initiation of crack growth allows extra energy to accumulate, leading to eventual crack branching.

In smaller crack-length configurations (i.e., $a = 0.1$ m and $a = 0.2$ m), crack formation involves branching in a single step. As a result, the crack tip speed is not calculated; instead, the position of the crack branching to the crack tip is compared at various loading rates. Table 4.5 illustrates the branching location relative to the fiber's center and the location relative to the crack tip. As the loading rate increases, the branching location moves closer to the crack tip. Higher loading rates lead to greater stress levels and faster crack propagation. When the loading rate increases, the fiber experiences faster deformation and stress buildup, causing stress to concentrate nearer the crack tip. This increased stress concentration encourages branching closer to the crack tip, which explains the observed trend in the branching location [63, 64]. The same correlation of crack branching location with loading rates is also observed for crack sizes $a = 0.4$ m and $a = 0.6$ m.

Table 4.5 Crack branching location comparison

Case	Crack length $a\ (m)$	Charging rate $\dot{c}$ (mol/Ls)	Branching location (m)	Branching location relative to crack tip (m)
A*	0.1	0.0008	0.265	0.296
A4	0.1	0.001	0.211	0.234
B2	0.2	0.0005	0.605	0.556
B3	0.2	0.0007	0.420	0.410
B4	0.2	0.001	0.288	0.278

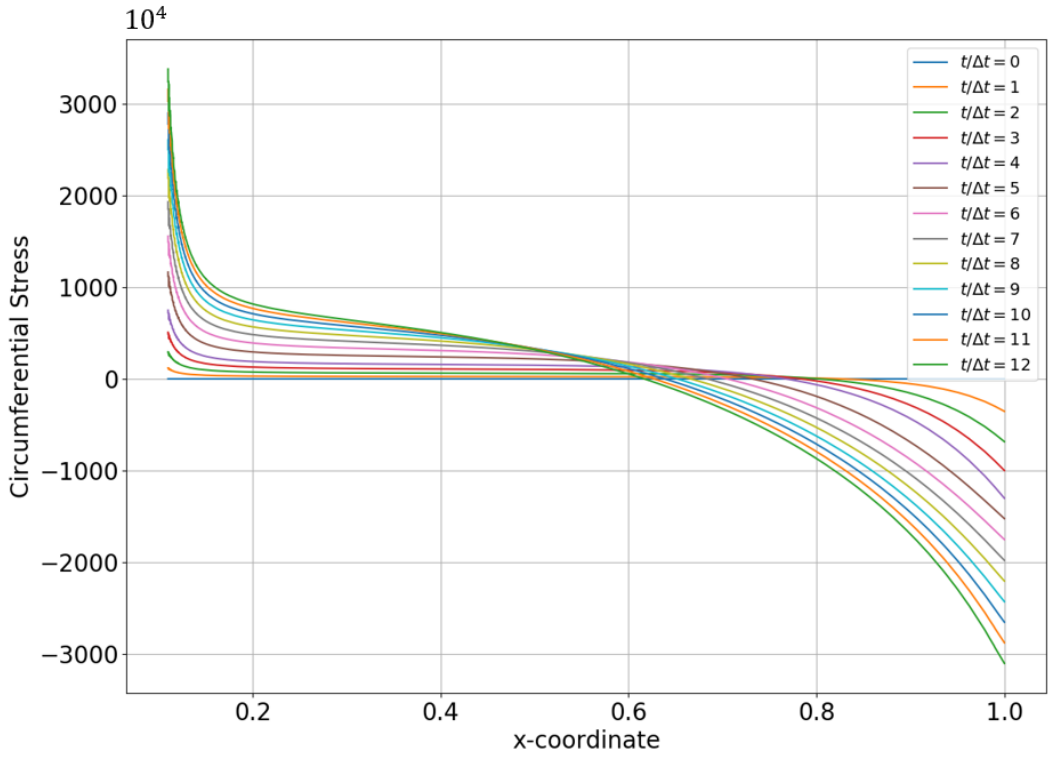


Figure 4.10. Circumferential stress distribution ($\sigma_{\theta\theta}$) for the test case B2 along y=0 (from x=0.11 (very close to crack tip) to x=1 (outer surface) for different time steps

In section 3.1.2, the text discusses the radial and circumferential stress distributions for charging conditions. Radial stresses are at their maximum at the inner part and zero at the outer surface. Conversely, circumferential stresses are negative at the outer portion near the surface and positive at the inner part. There is a twisting effect within the fiber, and its location depends on the charging rate and simulation time. To establish a connection between the point where circumferential stress is zero (the twisting point) and the location where cracks begin to branch, stress distributions along the crack tip are plotted from t=0 until crack initiation (Figure 4.10). As ionic concentration in the fiber increases, the point where circumferential stresses are zero shifts inward. The latest location is x=0.602, precisely where the crack branching starts (see Figure 4.10 and Table 4.5). When testing the same phenomenon at higher charging rates, the twisting point is approximately x=0.6, which differs from the branching locations in other cases. Nevertheless, this point is regarded as a threshold value; the branching location is either smaller or equal to this twisting point. Branching does not initiate in the area of negative circumferential stresses.

For crack sizes of $a = 0.4$ m and $a = 0.6$ m, the crack propagates in the initial crack direction until a certain point, and then crack branching occurs. The crack tip speeds are calculated for these two initial crack lengths, dividing the distance traveled in the x direction by a one-time step. Figure 4.10 compares these cracks' maximum crack tip speeds across three loading rates. For identical loading rates, smaller crack lengths exhibit higher crack tip speeds. These differences in crack tip speeds mirror the variation observed in maximum radial and circumferential stresses during crack propagation, as detailed in Table 4.4. Additionally, for $a = 0.6$ m, the crack tip speed increases with higher loading rates. When comparing the behavior of crack branching and crack tip speeds with smaller crack lengths, it is evident that Griffith's theory for brittle fracture suggests that the critical stress for crack growth typically decreases with larger crack sizes [35].

We compare the fiber's calculated wave speeds with the observed crack tip speeds to understand the dynamics of crack propagation and the fiber's response under different conditions. The fiber's wave speeds are calculated using the formulation in [59] and the material constants in Table 3.2. The details of the calculation are explained in Appendix A. The wave speeds of the fiber are as follows: Dilatational (P-Wave) Speed (V_P): 4860 m/s, Shear (S-Wave) Speed (V_s): 2598 m/s, Rayleigh Wave Speed (V_R): 3133 m/s and Critical Wave Speed (c_s): 3676 m/s. When the maximum crack tip speeds are shown in Figure 4.11 with these wave speeds, the following observations are made. For the smaller crack length (a = 0.4 m), the crack tip speeds for different charging rates generally exceed the Rayleigh wave speed and reach the critical wave speeds but remain below the critical wave speed. For the larger crack length (a = 0.6 m), the crack tip speeds mostly range between the shear wave speed and below or very close to the Rayleigh wave speed, with some values even below the shear wave speed. There is a crack tip speed twist that occurs at high charging rates. As the charging rate increases, the concentration gradient becomes steeper, providing more driving force for crack propagation and increasing the crack tip speed. One possible explanation for this decrease is that the location of crack branching starts shifting inwards.

At certain loading rates, the crack might temporarily be arrested due to insufficient energy or a change in material properties at the crack tip. This can temporarily reduce crack tip speed before it accelerates again when the conditions become more favorable for propagation [77]. Further analysis should be conducted to determine the specific explanations for this twist. These analyses are beyond the scope of this study and will be considered as future work.

Crack tip speeds for the smaller crack length and higher loading rates exceed the Rayleigh wave speed, indicating more dynamic crack propagation, but they do not reach the dilatational wave speed. Smaller crack lengths tend to have higher crack tip speeds, often exceeding the Rayleigh wave speed, while larger crack lengths exhibit lower speeds, generally below or close to the Rayleigh wave speed. The

comparison with wave speeds confirms that increasing crack length decreases crack tip speed.

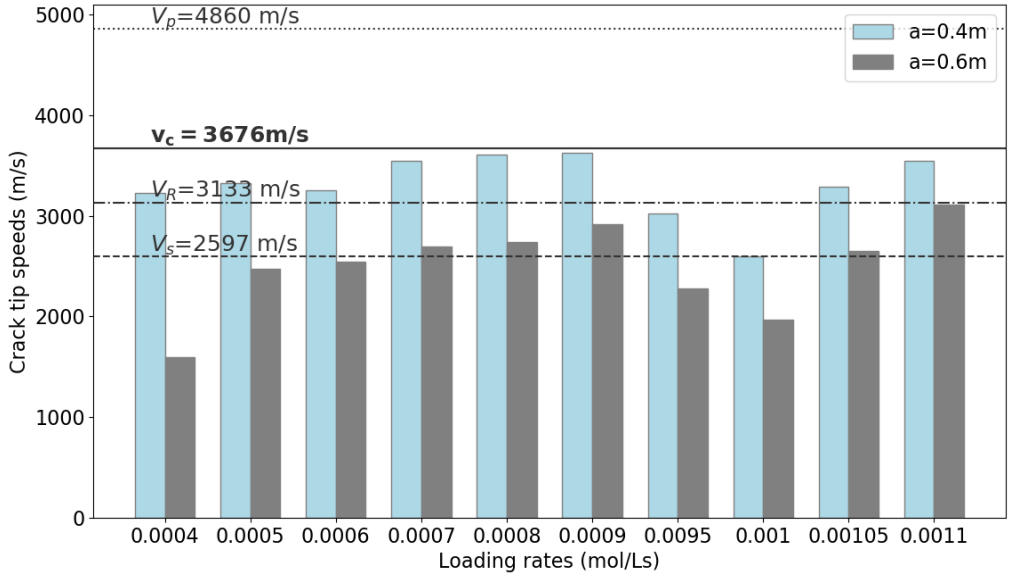
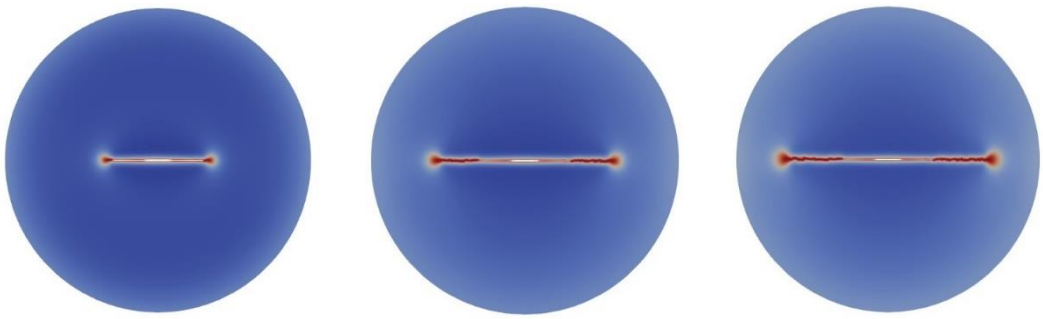
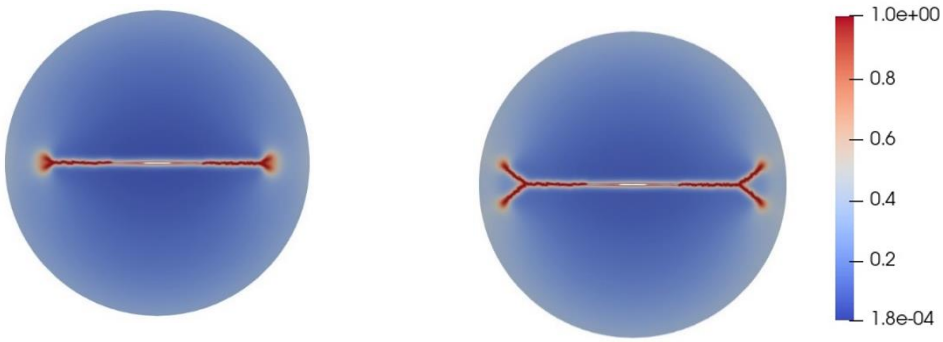


Figure 4.11. Maximum crack tip speeds of cracks $a = 0.4$ m and $a = 0.6$ m

For example, Figure 4.12 illustrates the phase field distributions capturing key stages of crack evolution and separation in test case D2, characterized by an initial crack length of 0.6 m and a 0.0005 mol/Ls charging rate. The figure's color scale employs blue to represent zero phase field values and red to signify a phase field value 1. At the time $t_n/\Delta t$ =8, corresponding to the stage before crack initiation, and extends through times $(t_n/\Delta t)$ 9 to 11, marking crack propagation, followed by time $t_n/\Delta t$ = 12, where crack branching begins. Appendix B gives all the frames of tests used for crack branching and crack tip speed comparison.

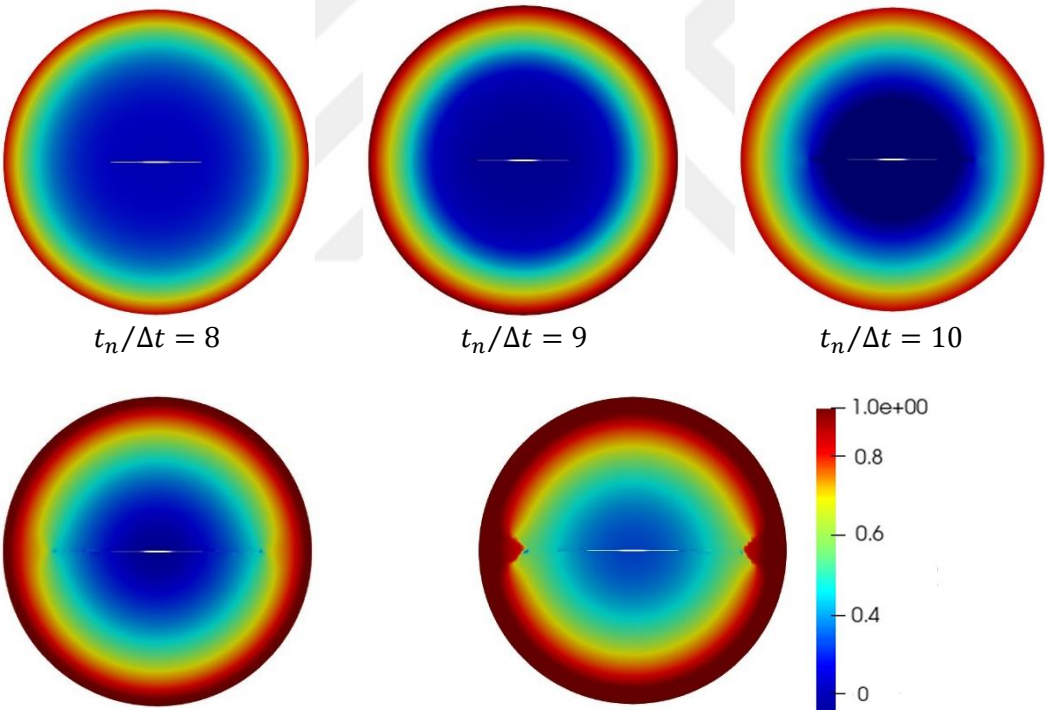


$t_n/\Delta t = 8$ $t_n/\Delta t = 9$ $t_n/\Delta t = 10$



$t_n/\Delta t = 11$ $t_n/\Delta t = 12$

Figure 4.12. Phase field distributions during crack growth and propagation for the test case D2 (a=0.6 m and $\dot{c} = 0.0005$ (mol/Ls)



$t_n/\Delta t = 8$ $t_n/\Delta t = 9$ $t_n/\Delta t = 10$

$t_n/\Delta t = 11$ $t_n/\Delta t = 12$

Figure 4.13. Ionic concentration distributions during crack growth and propagation for the test case D2 (a=0.6 m and $\dot{c} = 0.0005$ (mol/Ls)

Figure 4.13 shows the ionic concentration distribution corresponding to the phase field distributions in Figure 4.12.

Figure 4.14 compares crack tip speeds for two different crack lengths under the same charging rate (Test Case C2 and D2). The starting times for both cracks are identical. The initial propagation of the crack occurs over a relatively short distance, after which it accelerates. As the crack front approaches the surface, it decelerates and attempts to branch symmetrically within the crack plane. Comparing Figure 4.12 and Figure 4.13, it is evident that crack branching does not occur at the highest crack tip speeds. Instead, crack propagation takes place along the x-axis before branching begins at the second highest speed, which happens very close to the specimen boundary.

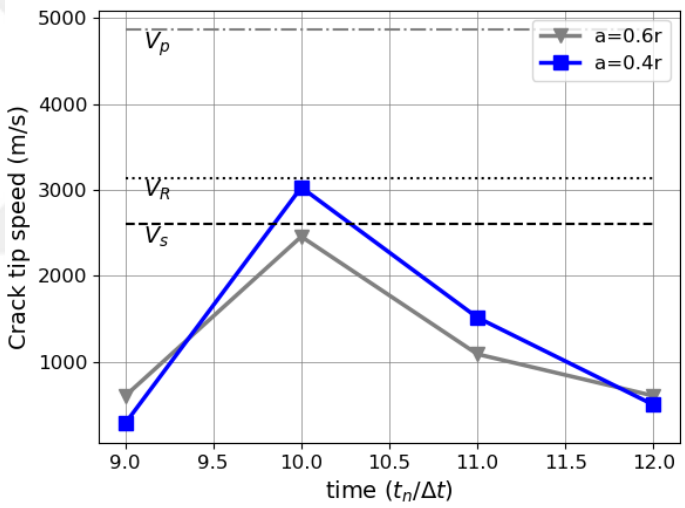


Figure 4.14 Crack tip speed comparison of two different crack lengths in the same loading rate ($\dot{c} = 0.0005$ (mol/Ls)

The viscosity parameter is included in the phase field algorithm for post-crack initiation stability (for details, please look at sections 2.3 and 4.1). The effect of the viscosity parameter on the crack tip speed is a question mark. To investigate this, one test case is selected (Test D3), and simulations are repeated for different viscosity parameters. The results are plotted in Figure 4.15. For the $\eta = 0$ (without any viscosity term), This test case's maximum crack tip speed is calculated as 2750

m/s., which is very close to the selected viscosity term ($\eta = 10^{-6}\ \mathrm{Ns/m^2}$) result. Increasing the viscosity term increased the crack tip speed and deviated from the $\eta = 0$ value. This term should be selected small enough to avoid affecting the results.

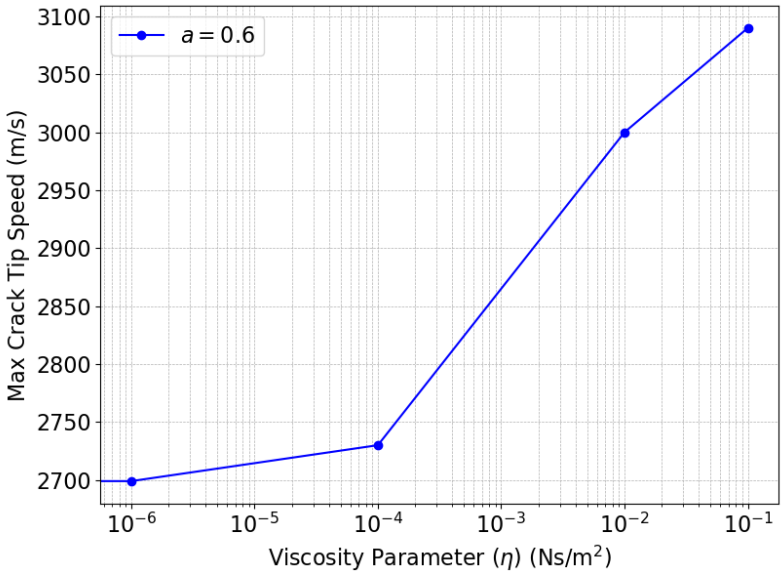
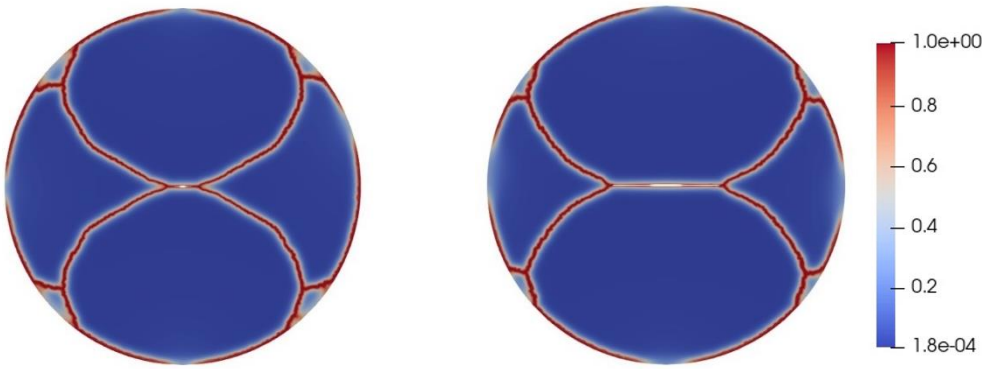


Figure 4.15. Maximum crack tip speed of the fiber for different phase field viscosity parameters (η) crack length for $\dot{c} = 0.0007\ \mathrm{mol/Ls}$ (a) $a = 0.6\ m$

The crack propagation behavior for higher loading rates is also examined to determine the upper limits for this fiber under these loading conditions. At loading rates exceeding $\dot{c} = 0.001\ \mathrm{mol/Ls}$, the crack either begins propagating in a single time step or immediately branches from the crack tips. Additionally, the crack extends to the outer boundary and continues to propagate. Based on this observation, further analysis under these loads was unnecessary. The phase field distribution following crack formation is depicted in Figure 4.16.

In summary, this section explores the behavior of a center crack under various loading rates and crack sizes. It investigates the analysis of crack tip speeds and examines the mechanisms of crack formation and growth.



(a) (b)

Figure 4.16 Phase field distribution after crack propagates in a one-time step for $\dot{c} = 0.004$ mol/Ls (a) $a = 0.2\ m$ (b) $a = 0.6\ m$

4.3.2 Circular Fiber with Arc Crack

In the previous section, fibers with central cracks are analyzed. It is well known that cracks decrease the mechanical strength of fibers due to decreases in load transfer across crack surfaces. However, the concentration difference plots show that radial cracks have no significant impact on ion diffusion because these cracks are entirely within the particle's interior and are not exposed to the electrolyte. Conversely, arc cracks are expected to affect diffusion by obstructing ion movement with their exposed surfaces. To investigate this mechanism, arc cracks parallel to the fiber's outer surface are investigated during the charging state in this section.

4.3.2.1 Geometry and Boundary Conditions (Arc Crack)

Similar to the central crack case, a fiber with a radius r is considered in a 2D plane strain setting. We also incorporate possible initial arc cracks with arc length $a(\rho, \theta)$ into the structure, where ρ is the radius of the arc crack, θ is the arc angle. The ionic concentration is applied to the outer boundary, ranging up to 1 mol/l, with a zero concentration at the initial state and reference ionic concentration $c_0 = 0.0001$ mol /l. The diffusion problem with the arc crack is modeled to discuss the

effect of the electrolyte during the charging state with different initial crack lengths and charging rates ($\dot{c}$). The material parameters for Li and the fiber are selected as before; see Table 3.2.

Table 4.6 The material parameters used in numerical examples.

θ (deg)	ρ (m)	$\dot{c}$ (mol/Ls)
40	0.9	0.00008
45	0.8	0.0001
50		0.0003
		0.0005
		0.0007

Table 4.6 shows the parameters defining the crack geometry and charging rates used in numerical examples. Simulations are conducted using three different crack lengths (measured by arc angle), three different crack locations (measured by distance to the fiber center), and four loading rates. The study investigates the effects of crack length and locations (especially those closer to the surface) and charging rates on fracture mechanisms, crack propagation, and the influence of loading rates. Figure 4.17(a) shows the geometry, crack parameters, and loading conditions. One of the mesh structures is shown in Figure 4.17(b). A finer mesh is used near the crack surfaces. A coarser mesh was used in areas far from the crack zone to reduce computational time.

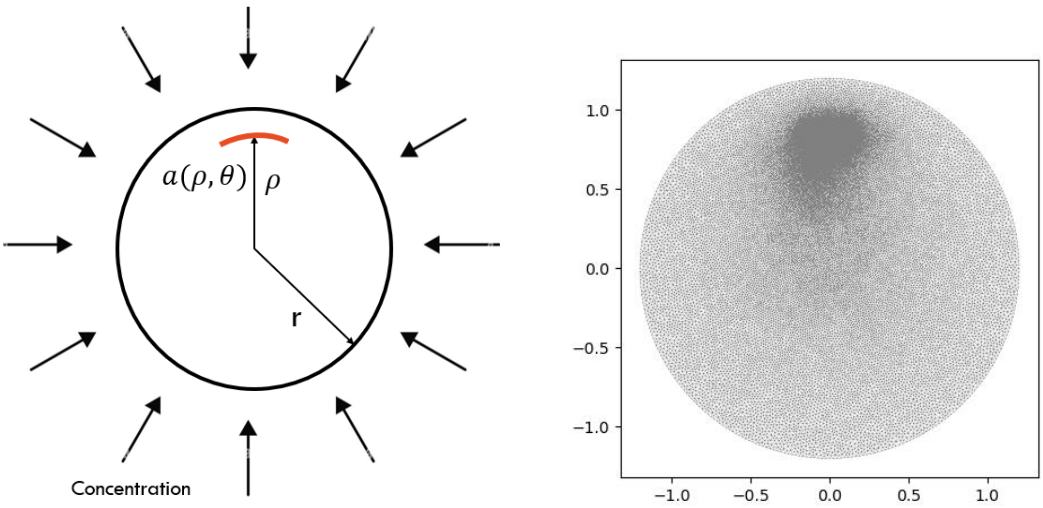


Figure 4.17. (a) Geometry and boundary conditions of fiber with an arc crack, (b) Mesh structure of fiber with a crack length $\rho = 0.9\ m$ and $\theta = 19°$

4.3.2.2 Numerical Results (Arc Crack)

The analysis starts by comparing the distribution of ions with previous fiber models. The same ionic concentration loading rate $\dot{c} = 0.0003$ mol/Ls is applied at the outer boundary, leading to the maximum ionic concentration for comparison. This process involves comparing a fiber with a central crack ($r = 0.6$ m), an arc crack ($\rho = 0.8$ m and $\theta = 50°$), and a fiber without a predefined crack. All three fiber models share the same boundary conditions and material properties. The only distinction is the presence or location of a crack with the same phase field parameters. The concentration difference, the variation between the highest and lowest fiber concentrations, is documented during the simulation.

The results are shown in Figure 4.18. The gray curve in the plot represents the maximum concentration in the fiber, i.e., the prescribed concentration at the outer surface. Without any predefined crack, the concentration difference in the fiber is 63% of the maximum value (indicated by the red curve). In contrast, the concentration difference increases to 75% when a central crack is present

(indicated by the green curve). Interestingly, the impact of crack presence on ionic diffusion is notable, even when the crack is not positioned near the fiber surface. Conversely, arc cracks close to the surface affect diffusion by obstructing ion movement with their exposed surfaces. The fiber with an arc crack has a 90% concentration difference (blue curve). The presence of a crack increased the concentration difference in the body.

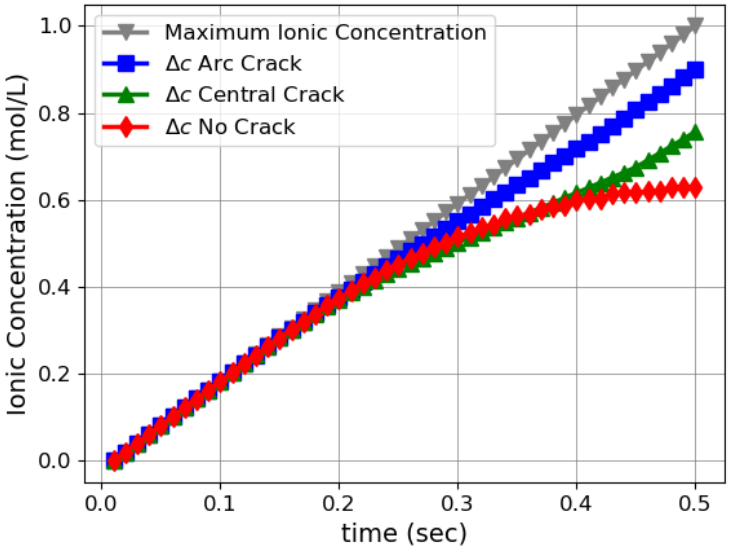
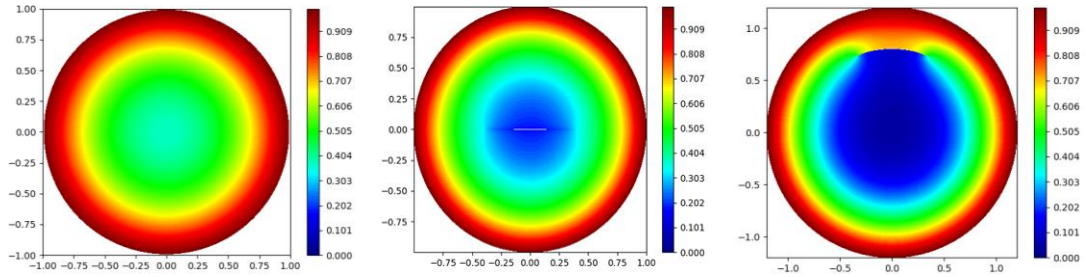


Figure 4.18. The maximum concentration difference compared with fiber without arc and center cracks.

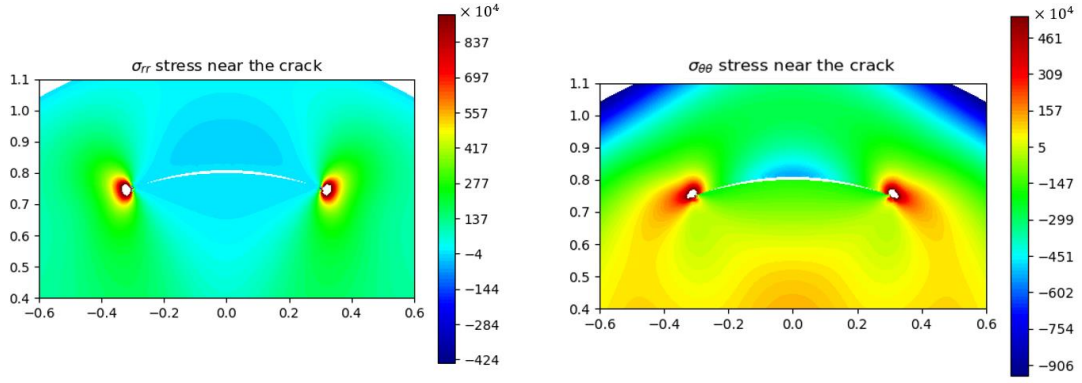
Figure 4.19 compares the distribution of ionic concentration in three different fiber models. The screenshots were taken at the end of the simulation (time = 0.5) when the differences between the three fibers were most distinct. When the crack is located at the center, the Li diffusion in the fiber with a central crack closely resembles that of a particle without cracks; see Figure 4.19 (a) and (b). On the other hand, an arc crack significantly impedes the ionic diffusion, as shown in Figure 4.19 (c). Arc cracks near the surface cause a more significant concentration difference within the fiber, affecting the overall charging performance at a macroscopic level.



(a) (b) (c)

Figure 4.19. Concentration distribution of fiber at time = 0.5 for (a) fiber without crack, (b) central crack ($r = 0.6$ m), (c) arc crack ($\rho = 0.8$ m and $\theta = 50°$)

The substantial concentration gradient generated leads to elevated radial stresses that are concentrated at the crack tips. At these tips, radial and circumferential stresses are positive and reach their maximum values. Additionally, the difference in concentration between the upper and lower sides of the crack results in a unique stress distribution. Specifically, there is a negative stress concentration bump on the upper side of the crack, which contrasts with the high positive stresses observed at the crack tips (Figure 4.20). This complex interplay of stresses around the crack highlights the critical areas where fiber failure will likely initiate and propagate. The crack is likely to propagate towards regions of high tensile circumferential and radial stresses while avoiding or deviating from regions of high compressive circumferential stresses. The compressive stress on the upper side of the crack can cause the crack to bend or curve downwards, away from the compressive zone. In summary, the positive high radial and circumferential stresses at the crack tips drive the crack to propagate forward. In contrast, the negative circumferential stresses on the upper side can alter its path, leading to a curved or more complex trajectory.



(a) (b)

Figure 4.20. (a) Radial stress distribution (b) Circumferential stress distribution corresponding to onset of crack growth ($\rho = 0.8$ m and $\theta = 45°$)

Crack growth is observed for all the test cases described in Table 4.6. The crack growth begins in the circumferential direction, consistent with the expected stress distribution patterns. The crack extends in a circular direction due to the high tensile stresses at the crack tips. As the crack extends, the stress distribution evolves, causing the crack tips to deviate towards the outer surface. This deviation occurs because the crack seeks to propagate through regions of lower resistance, moving away from areas of compressive stress and towards areas where the tensile stresses are more favorable for crack growth. Ultimately, the crack path transitions from a predominantly circumferential trajectory to one that curves outward, approaching the fiber's outer surface; see Figure 4.21. The crack propagation figures for all test cases analyzed are given in Appendix B. Only one of the cases is chosen here to show as an example.

The crack tip speed for all test cases is calculated using the following procedure. Since the crack growth does not follow a straight path, points along the path are selected, and their x and y coordinates are determined. These data points are chosen very close to each other. The differences in the x and y coordinates between two points are calculated, and then the distance between the two points is determined. Summing all these relative lengths gives the total crack length at a given time. This crack length is then divided by the time difference to find the

crack tip speed. For this geometry-specific calculation method, the comparison of crack tip speeds in different arc cracks is done only to understand the general tendency. The crack tip speeds are not compared with other crack types for the same reason.

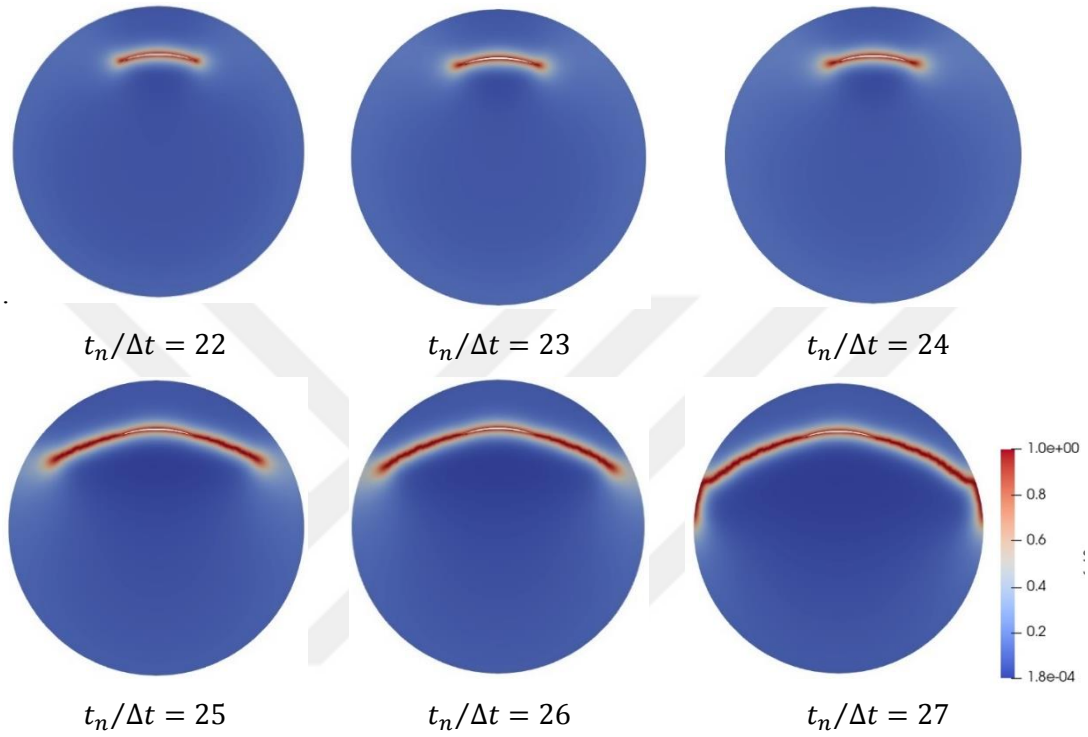


Figure 4.21. Phase field distributions during crack growth for the arc crack with the parameters θ= 45º, ρ=0.8 m and $\dot{c} = 0.0001$ mol/Ls

Figure 4.22 shows the crack tip speed over time for three different arc cracks with angles θ=50º and θ=45º where ρ=0.8 m. The two curves exhibit a similar pattern where the crack tip speed is initially low, increases sharply to a peak value, and decreases. When Figure 4.21 and Figure 4.22 (corresponds to the blue curve in Figure 4.22) are analyzed together, all cracks start with low crack tip speeds, indicating stable crack growth initially. The 40° crack reaches the outer boundary in one-time step. If the crack reaches the outer surface in one time step, the crack tip speed is not calculated. The 50° crack has the lowest peak speed among the three angles considered. Increasing crack length decreases the crack tip speed. The

crack slows down significantly as it grows closer to the outer surface. Additionally, it is important to note that the crack tip speeds are calculated only until the crack reaches the outer surface. These calculations do not include the portion of the crack propagation at the outer surface.

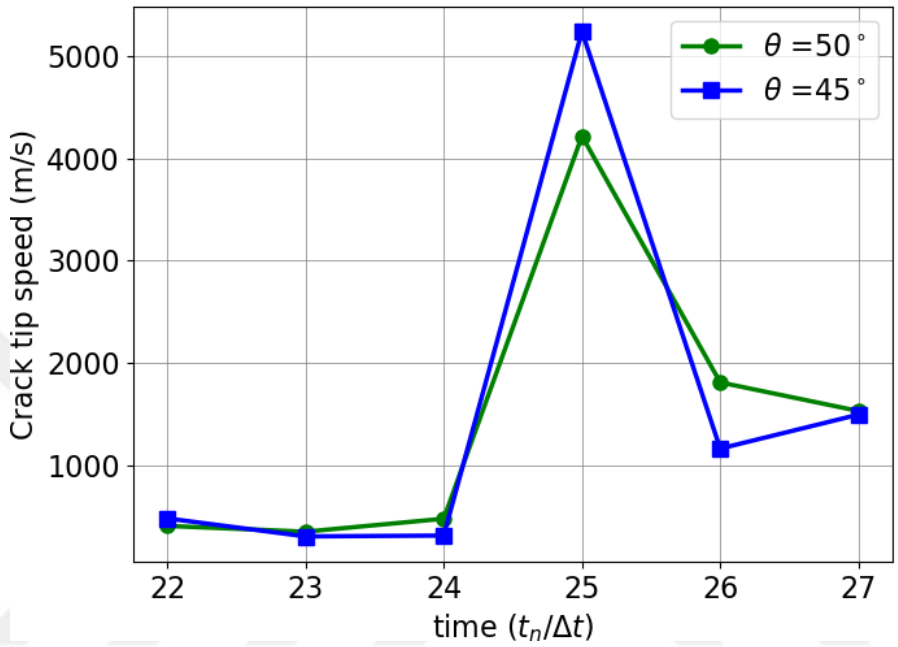


Figure 4.22. Crack tip speed comparison of two different arc cracks for $\rho = 0.8$ m and charging rate $\dot{c} = 0.0001$ mol/Ls

Table 4.7 Maximum Crack Tip Speeds for $\rho = 0.8$ m

	$\dot{c}$=0.00008	$\dot{c}$=0.0001
θ=50º	5576	4221
θ=45º	4846	5245
θ=40º	4397	-

Table 4.7 lists the maximum crack tip speeds for the cases with lower charging rates. For the higher charging rates, the crack tips reach the outer surface in one time step, so crack tip speeds are not calculated.

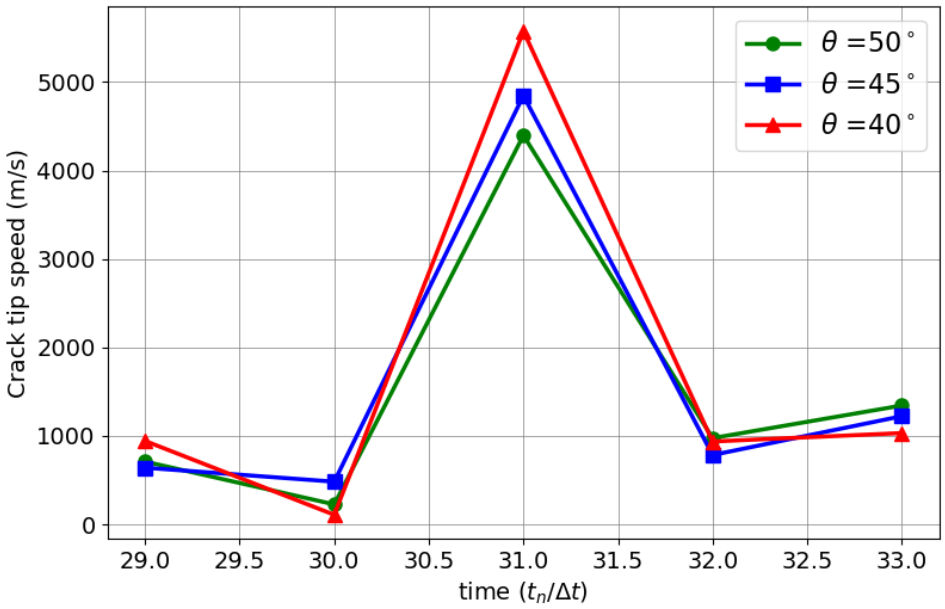


Figure 4.23. Crack tip speed comparison of three different arc cracks for $\rho = 0.8$ m and charging rate $\dot{c} = 0.00008$ mol/Ls

The maximum crack tip speeds for the lowest charging rate, $\dot{c} = 0.00008$ mol/Ls, are shown in Figure 4.23. When Figure 4.22 and Figure 4.23 are considered together, the first observation is that higher ionic concentration loading rates increase crack tip speeds. This is likely due to the higher energy input associated with increased loading rates, accelerating crack propagation. Additionally, shorter crack lengths exhibit higher crack tip speeds. This can be attributed to the fact that shorter cracks have less surface area, leading to lower resistance to the propagation and, thus, faster crack tip speeds. When a crack propagates through a material, new surfaces are created. Creating these new surfaces requires energy, referred to as surface energy (γ_s) or fracture energy [64]. The crack propagation criteria proposed by Griffith is the energy release rate(G) is greater than the critical energy release rate (G_c) which equals the $2\gamma_s$[65]. The total energy required for crack propagation is the product of the surface energy and the new surface area created by the crack. As the crack length increases, the surface area of the crack also increases. Therefore, the total energy required for crack propagation increases with the crack

surface area [66]. With lower resistance, more supplied energy can be directed towards crack propagation rather than dissipating through other mechanisms like plastic deformation or overcoming microstructural barriers [64]. This leads to crack tip speeds faster. Also, stress concentration is more severe in shorter cracks. This localized stress can lead cracks to propagate faster in cases with short initial cracks.

Table 4.8 The maximum radial and circumferential stresses at the onset of crack propagation

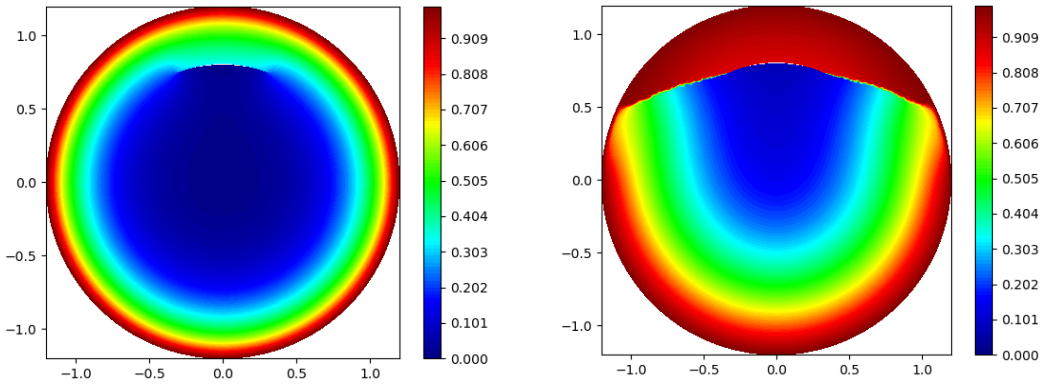
Testcase	Arc Angle θ (deg)	Charging Rate $\dot{c}$ (mol/Ls)	σ_{rr}^{max} (MPa)	$\sigma_{\theta\theta}^{max}$ (MPa)	$\sigma_{r\theta}^{max}$ (MPa)
1	40	0.0001	50	23	16
2	40	0.0003	27	12	8
3	40	0.0005	75	50	32
4	40	0.0007	120	80	51
5	45	0.0001	21	20	13
6	45	0.0003	18	10	6
7	45	0.0005	40	25	16
8	45	0.0007	12	10	6
9	50	0.0001	23	18	11
10	50	0.0003	16	12	5
11	50	0.0005	25	10	7
12	50	0.0007	20	9	6

The maximum radial (σ_{rr}^{max}), circumferential stresses ($\sigma_{\theta\theta}^{max}$), and shear stresses ($\sigma_{r\theta}^{max}$) that occur at the crack tip before crack propagation are listed in Table 4.8. When these stresses are compared with central crack stresses in Table 4.4, the closeness of the cracks to the surface makes them more prone to propagation. Across all scenarios that lead to crack growth, the findings consistently show that the maximum radial stresses exceed the circumferential and shear stresses.

However, they remain within the same order of magnitude. As discussed in Varna's work [33], radial stresses dominate in initiating radial cracks close to the surface. Notably, Table 4.8 shows that the shear stresses are of the same order of magnitude as the radial stresses. Moreover, the crack growth path is angular, indicating that both Mode-I and Mode-II fracture mechanisms are at play.

This suggests that while radial stress is critical in initiating the crack, the direction and growth of the crack are influenced by the interplay of shear stress and circumferential stress, leading to a complex crack propagation behavior. The angular path of the crack further supports the involvement of both tensile (Mode-I) and shear (Mode-II) forces, indicating a mixed-mode fracture. This complexity underscores the importance of considering all stress components in predicting crack growth and resistance, especially in cases where the crack is close to the surface and thus more susceptible to propagation.

Furthermore, the crack size for identical loading rates and fiber radius reduces the maximum stresses. This trend suggests a significant influence of crack size on stress distribution, indicating that larger cracks experience lower stress concentrations than smaller ones under similar loading conditions.



(a) (b)

Figure 4.24. Concentration distribution of fiber with an arc crack (θ= 45º m, ρ=0.8 m and $\dot{c} = 0.0001$ mol/Ls) (a) before crack growth (b) after crack growth

Figure 4.24 compares the concentration distribution before and after crack growth. The figures illustrate the effect of crack propagation on the concentration field, highlighting the shielding effect in the inner regions. The flux over the crack surfaces is zero, indicating that the crack acts as a barrier to diffusion. As a result, the concentration remains zero on the inner side of the fiber even after the crack reaches the outer boundary. This comparison clearly shows how the curved crack growth impacts the concentration distribution, with the inner region being shielded from any changes in concentration.

4.3.3 Circular Fiber with T-Crack

In previous sections, we explored two critical types of cracks in fiber structures. This chapter focuses on another significant crack mechanism that can occur during the charging process: the formation of arc cracks that start from the ends of radial cracks. Radial cracks, caused by repeated intercalation and deintercalation cycles in fiber structures, were initially thought to not affect ion diffusion along radial pathways [33]. Arc cracks, driven by high radial tensile stresses during initial intercalation stages, can start from the tips of radial cracks and propagate circumferentially [33]. So, our discussion on arc cracks reveals their dynamic role in mechanical stress and ionic diffusion processes. This understanding emphasizes the complexity of crack mechanisms. So, the arc crack propagation disrupts diffusion by exposing ion movement, highlighting the interplay between mechanical stresses and ionic dynamics in composite materials.

4.3.3.1 Geometry and Boundary Conditions (T-Crack)

Again, a single fiber with a radius r in a 2D plane strain setting is considered. We also incorporate possible initial T-crack mechanisms into the structure with radial crack length b and arc crack defined by $a(\rho, \theta)$, where ρ is the radius of the arc crack, and θ is the arc angle. Table 4.9 tabulates all the variables used in numerical

simulations. Simulations are conducted using three different crack lengths (measured by arc angle or x component of arc length, i.e., x_a), three different crack locations (measured by distance to the fiber center), and three loading rates to compare results.

Table 4.9 The material parameters used in numerical examples.

θ (deg)	ρ (m)	$\dot{c}$ (mol/Ls)	x_a
19	0.9	0.0003	0.30
16		0.0005	0.25
13		0.0007	0.20

Figure 4.25(a) shows the geometry, crack parameters, and loading condition. The ionic concentration is applied to the outer boundary, ranging up to 1 mol/l, with a zero concentration at the initial state and reference ionic concentration $c_0 = 0.0001$ mol/l. The phase field boundary condition is applied only to the circular part of the crack. The radial portion is initially defined as a flux-free and traction-free surface. The diffusion problem with the T-crack is modeled to discuss the effect of the complex crack mechanism during the charging state with different initial crack lengths and different charging rates $\dot{c}$. The material parameters for Li and the fiber are chosen as before; see Table 3.2. Figure 4.25(b) shows one of the fiber mesh structures with a T-crack. A finer mesh is used near the crack surfaces. A coarser mesh was used in areas far from the crack zone to reduce computational time.

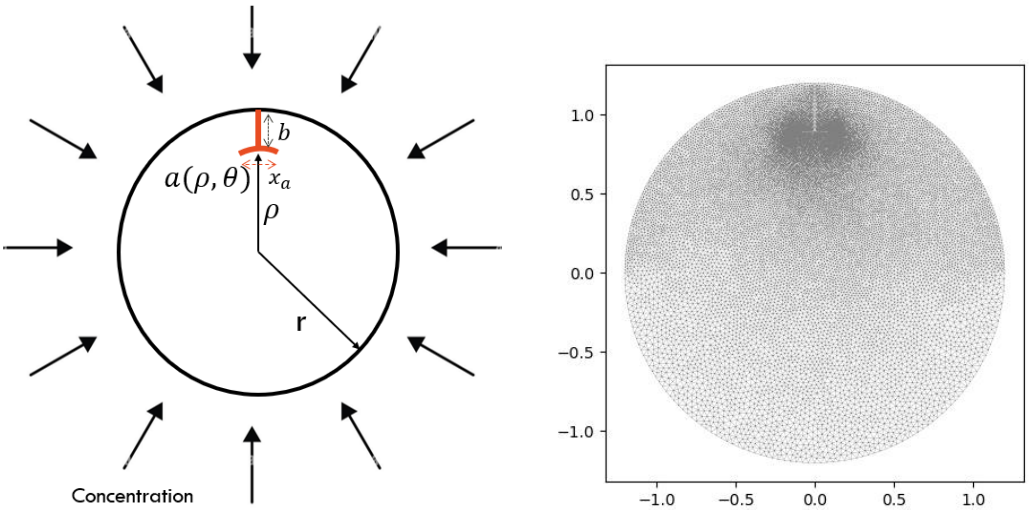


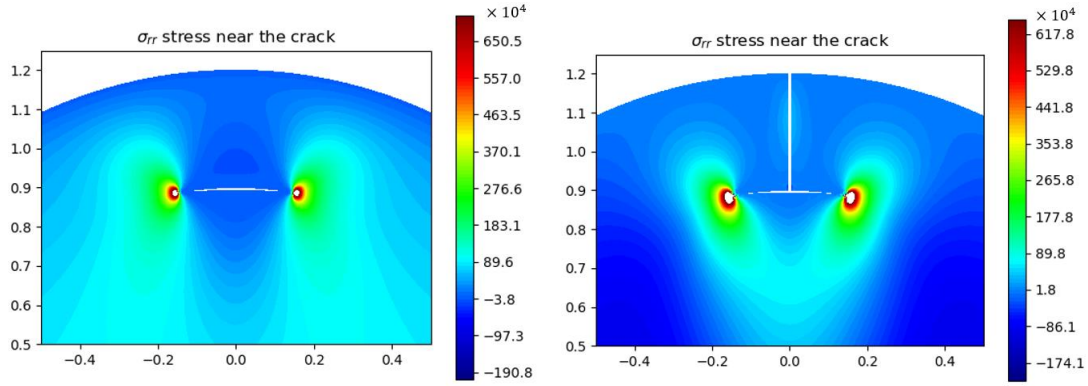
Figure 4.25. (a) Geometry and boundary conditions for the Li intercalation fiber with a T-crack (b) (b) Mesh structure of fiber with a crack length $\rho = 0.9\ mm$ and $x_a = 0.3$m

4.3.3.2 Numerical Results (T-Crack)

The discussion on T-cracks begins by comparing radial and circumferential stress distributions with the arc crack before crack growth. The prescribed concentration is applied to the outer surface. The radial crack surfaces are physically defined and chosen as flux-free and traction-free. For the same loading rate ($\dot{c}$=0.0005 mol/Ls), the T-crack's radial and circumferential stress distributions are compared with the arc crack stress distributions. The similarities or differences are highlighted.

Figure 4.26 (a) shows the radial stress distribution for an arc crack. The stress is concentrated around the crack tips, and the stress pattern around the crack tip is more or less symmetric with respect to the crack surface. There are notable stress intensities at the ends of the arc crack. Figure 4.26 (b) illustrates the radial stress distribution for a T-crack. In this instance, the areas of high stress are clearer and more significant. When comparing these stress distributions, we can see that the arc

crack tends to show more symmetrical stress concentrations around the crack tips, while the T-crack results in a broader stress distribution along the radial direction.



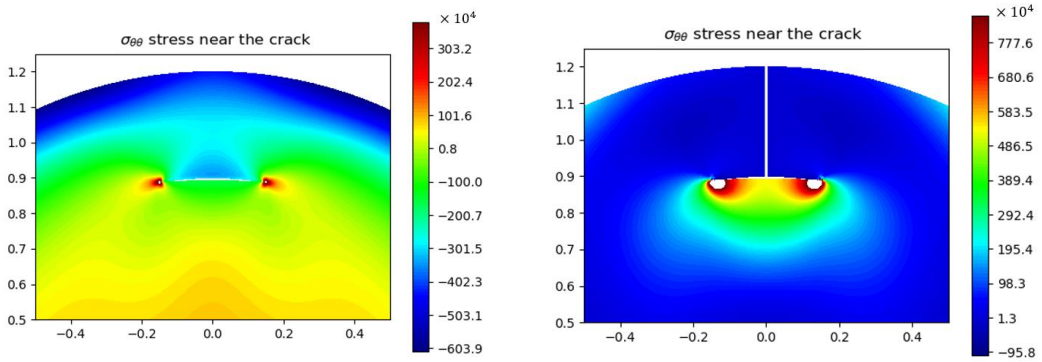
(a) (b)

Figure 4.26. Radial stress distribution corresponding to the onset of crack growth (a) Radial Crack (b) T-crack for $\dot{c}$=0.0005 mol/Ls. Note that the positions and sizes of the arc cracks are the same in both cases.

Figure 4.27 illustrates the circumferential stress distributions for an arc crack and a T-crack under identical conditions. The same symmetry differences are observed in circumferential stress distributions. The broader high tensile stress region in the case of the T-crack suggests a more extensive influence on the fiber's structural integrity, potentially leading to different failure mechanisms compared to the arc crack. The arc crack's localized stress concentrations might lead to more focused damage near the crack tips, whereas the T-crack could cause a more widespread fiber weakening. It is also worth noting that, in the case of the T-crack, the radial crack's presence almost eliminates compressive stress in the circumferential direction, allowing for expansion in that direction. The compressive stress values in the T-crack case are significantly lower than those in the arc crack case, especially near the surface region.

These observations indicate that T-cracks might create a higher tensile stress concentration in the fiber than arc cracks. Therefore, in the T-crack case, cracks

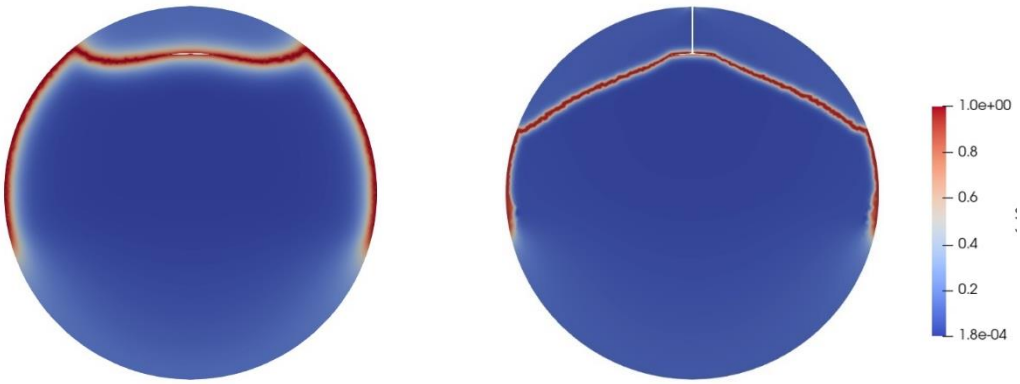
could propagate more easily and in different directions, leading to various failure mechanisms under similar loading conditions.



(a) (b)

Figure 4.27. Circumferential stress distribution corresponding to the onset of crack growth (a) Radial Crack (b) T-Crack for $\dot{c}$=0.0005 mol/Ls. Note that the positions and sizes of the arc cracks are the same in both cases.

Figure 4.28 illustrates the phase field distributions for an arc crack and a T-crack after crack growth. These phase field distributions highlight the fiber regions that have experienced crack propagation, with the red areas indicating the regions where the phase field parameter is at its maximum, signifying crack presence. Appendix B gives all the frames of tests used for crack tip speed comparison.



(a) (b)

Figure 4.28. Phase field distribution (a) arc crack (b) T-crack for $\dot{c}$=0.0005 mol/Ls

The same test case is used in stress distribution comparison and phase field distribution. For arc cracks, the propagation is stable and primarily circumferential, driven by localized stress concentrations at the crack tips. The crack deviates to the upper part when getting closer to the surface. At the crack tip, the stress intensity factors influence the crack propagation direction [67]. As can be seen from Figure 4.28, the stress fields shown in Figure 4.26 and Figure 4.27 lead to different crack trajectories for the two cases considered. In the T-crack case, large tensile circumferential stress concentrations result in a propagation closer to Mode II; see Figure 4.28 (b), while the crack propagation in the arc crack case seems closer to Mode I; see Figure 4.28 (a). When Figure 4.28 (a) is compared with Figure 4.26 (a) and Figure 4.27 (a), even though the circumferential stress is negative in the outer region, the radial stress is positive or less negative, creating a net tensile environment. The radial stress can contribute to the upward deviation of the crack by providing a driving force for crack propagation in that direction. The overall stress gradient within the fiber may guide the crack upwards. During intercalation, the insertion of lithium ions can also create expansion and contribute to the positive radial stresses, aiding in the upward deviation of the crack. Please note that the crack location to the center (ρ) is 0.9 m. At the same time, in the previous chapter, this distance is chosen as 0.8 m. The cracks are getting closer to the surface, and the concentration gradients are more effective on crack propagation mechanisms.

On the other hand, T-crack propagates in a more complex manner. The difference in stress fields affects the crack propagation mechanisms. The irregular crack path suggests that the stress distribution around the T-crack induces a less stable propagation than the arc crack. One of the possible explanations for this crack path is as follows. The fiber subjected to complex loading, such as during intercalation and deintercalation cycles, the principal stresses can orient themselves such that the planes of maximum tensile stress (Mode I) and maximum shear stress (Mode II) align at 45 degrees to the initial crack direction. The T-crack propagates at an angle where these principal stresses facilitate the opening and sliding of the crack faces.

Figure 4.29 displays the phase field distribution of the crack before, during, and after crack growth. Due to the dynamic nature of crack growth, the intermediate steps in crack propagation are not visible. The crack speeds are not determined in T-crack geometry, because the crack tips reach the boundary at a single time step. No calculations are included for the portion of the crack traveling along the boundary of the fiber.

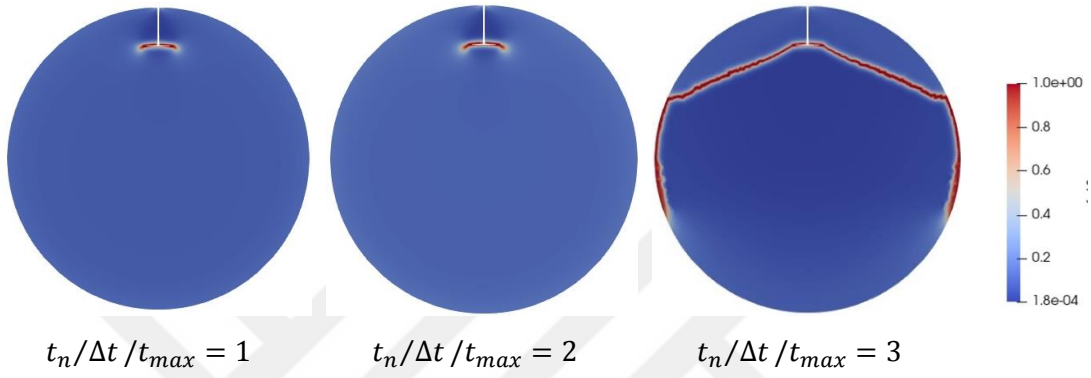


Figure 4.29. Phase field distributions during crack growth for the T-crack with the parameters $x_a = 0.25$, $\rho = 0.9$ m and for $\dot{c}$=0.0005 mol/Ls

CHAPTER 5

CONCLUSION

The concept of a structural composite battery represents an innovative breakthrough in materials science and energy storage technology. This multifunctional material is an energy storage solution and a load-bearing component, pioneering a new era of efficient and integrated design. These composite materials effectively store energy while preserving their structural strength by utilizing the intercalation process present in lithium-ion batteries. This process involves the insertion of ions between the layers of a material's crystal structure [52]. This dual functionality is particularly transformative for industries like aerospace, where composite laminates already contribute to constructing lightweight yet durable aircraft structures, thus enhancing fuel efficiency and overall performance. The remarkable properties of carbon fibers, known for their superior mechanical strength and promising energy storage capabilities, ensure that the energy storage capacity remains intact despite structural demands. This investigation can potentially revolutionize energy storage technologies, paving the way for advanced lithium-ion batteries with enhanced performance and efficiency while ensuring safety and reliability in various applications.

This thesis investigates the 3D battery concept, where carbon fibers play a pivotal role. In this innovative design, every individual fiber is an independent battery cell. Carbon fibers in this arrangement have a dual function: they act both as negative electrodes in each battery cell and as current collectors on the negative side. The thin solid polymer electrolyte (SPE) surrounding each fiber serves as both an electrolyte and a separator layer, thus improving the performance of each cell. The polymer matrix is doped with positive electrode particles, such as LiFePO4, which serve as the positive electrode in the battery cell. An electrically conductive

material, like carbon black, is introduced into the matrix through doping to facilitate electrical conduction within the matrix [24]. This unique role of carbon fibers in the 3D battery concept significantly contributes to the system's overall efficiency, potentially revolutionizing the field of energy storage.

The main advantages of this composition include enhanced energy density, reduced electrode distance, and flexibility in design. These benefits could lead to more efficient and compact energy storage solutions, opening new possibilities for various applications. However, several challenges need to be addressed, such as the complexity of manufacturing, the difficulties in scaling up production, the high costs associated with advanced materials and processes, and ensuring the long-term durability and reliability of the batteries [20-23]. Although there are difficulties, the investigation of 3D battery ideas shows great potential for improving the effectiveness and productivity of lithium-ion batteries, which contributes to the continual advancement of creative energy storage technologies.

In this concept, electro-chemo-mechanical coupling is employed to enhance the understanding and functionality of composite materials as energy storage solutions. A comprehensive knowledge and mathematical representation of composite batteries' electrochemical and mechanical properties and failure mechanisms are crucial. The primary objective is to investigate the mechanical stresses and strains induced by dimensional changes during the intercalation and deintercalation of Li ions. This includes studying crack formation on the surface of Li-transported surfaces of materials, which can lead to decreased cycling performance and reduced capacity. The commonly used approach combines diffusion and continuum mechanics models, taking advantage of the similarity between ionic diffusion and heat conduction [34,35,36,54].

The focus of this thesis on the crack mechanisms of structural batteries is crucial to addressing performance challenges and uncertainties related to this innovative concept. Simulating crack formation and propagation is essential to enhance

structural batteries' performance and resolve associated issues. By studying the damage mechanisms, a phase field model for fracture is integrated into the coupled system to model cracks' growth accurately. This approach helps understand the underlying reasons for composite batteries' failure and performance degradation.

The part chosen for simulations in this study is the carbon fibers within the composite battery. By integrating stress analysis and ion concentration distribution with predefined cracks, the research explores the complex relationship between mechanical stresses and ion diffusion and how they affect the structural integrity of carbon fibers. This comprehensive approach supports identifying critical crack mechanisms and aids in developing solutions to enhance structural batteries' durability and performance. The study identifies two primary types of cracks in carbon fibers: radial cracks, caused by high hoop stresses during deintercalation [33, 35, 57], and arc cracks, which can deflect from radial cracks during subsequent intercalation cycles [33].

By taking advantage of FENICS's symbolic differentiation capabilities [61, 62], the mechanical, electrochemical, and phase field weak forms, i.e., (2-49), (2-51), and (2-58), are directly transferred to the FENICS code.

The analysis starts by remodeling existing geometries for electrochemical loading, with or without cracks, using thermomechanical models adapted to chemo-mechanical scenarios. Chemical swelling is treated similarly to thermal expansion, involving pure volume increase (see Section 3.1.1). Initially, phase field coupling with mechanical problems is studied using a single-edge notched specimen to understand crack growth mechanics. This is extended to include electrochemical effects, examining how ionic diffusion affects stress distributions and crack propagation. The influence of viscous regularization (Eq. 2-37) on load-deflection curves and comparing monolithic versus staggered algorithm results are also discussed. Viscous regularization does not alter maximum load capacity but significantly impacts the stability of crack propagation post-peak load, consistent

with findings by Miehe et al. [48]. The monolithic model predicts a higher ultimate load and steeper post-peak response, while the staggered solution shows a lower ultimate load and a gradual post-peak curve. Crack propagation is faster in the staggered solution (see Section 4.1). These findings provide a critical foundation for the subsequent analysis and conclusions.

The main geometry studied in this thesis is a single fiber with a radius r in a 2D plane strain setting, simulating the charging state. Firstly, this circular domain is tested for electrochemical coupling without initial cracks to calculate stress distributions and predict critical time intervals and regions for potential damage. The study observed that peaks in ionic concentration differences correspond to maximum stresses. As the concentration difference increases, the outer region of the fiber expands more than the interior, causing radial tensile stress and circumferential compressive stress. Radial stresses are positive at the center because the outer portion expands further and exerts radial tractions on the inner part. Conversely, hoop stresses are negative in the outer region and positive in the inner region. This happens because the outer region tries to expand in the direction of θ, but the inner region, with a lower ionic concentration level, does not expand as much (see Section 3.1.2). This behavior aligns with findings by Klinsmann et al. [35] and Varna et al. [35].

These observations highlight the potential for two distinct types of damage: surface crack mechanisms near the fiber surface and central cracks positioned at the fiber's symmetry plane. In this study, the diffusion problem with three distinct crack configurations: a central crack, an arc crack, and a T-crack are modeled to discuss the effect of the chemical stresses during the charging state with different initial crack lengths and charging rates ($\dot{c}$). The ionic concentration is applied to the outer boundary, ranging up to $1\ \mathrm{mol/l}$, with a zero concentration at the initial state. The Butler-Volmer equation is not used in this simulation. Besides the complexity of the coupled equation set, the boundary condition is chosen as simple as possible. However, the prescribed concentration boundary condition must be discussed

whether realistic or not. The linearly increasing concentration BC is implemented such that the resulting current density and overpotential are consistent with Butler-Volmer kinetics. The constant concentration phase reflects a potentiostatic condition where the Butler-Volmer equation describes the steady-state current density [31]. The concentration at the surface impacts the overpotential and, consequently, the current density. Any prescribed concentration will reflect a realistic scenario where the Butler-Volmer kinetics are satisfied. The related updates in the solution algorithm will be planned for future work.

If the stress intensity at the crack tip exceeds a critical threshold as the outer surface reaches maximum concentration, it can trigger further crack propagation within the fiber [67, 68]. However, if the crack does not propagate at this point, it remains inactive in subsequent cycles. Central cracks require higher loading rates for propagation than surface cracks; with slower loading rates, new crack surfaces do not form from the crack tips even when the outer boundary reaches maximum concentration.

Comparative evaluations are conducted across various crack sizes and loading rates to understand these behaviors better. The findings consistently reveal that across all scenarios culminating in crack growth, maximum circumferential stresses consistently exceed radial stresses, leading to crack growth mostly in Mode-I. Moreover, Larger cracks experience lower stress concentrations, reducing maximum stresses compared to smaller cracks under the same loading conditions. The study also finds that smaller cracks require more energy to initiate propagation, highlighting the significant influence of crack size on stress distribution (see Section 4.3.1).

In the simulations, crack branching is also observed in some cases for fiber with center crack. When the crack is smaller, branching happens in a single time step without having a mode-I crack propagation, showing that the particle has accumulated more energy to initiate branching rather than self-similar propagation. This pattern is consistent across all loading rates. On the other hand, when the

initial crack size is larger, mode-I propagation occurs first, and branching is observed later. The reason for branching is the increased velocity of the crack tip. Studies by Freund [63] and Anderson [64] have shown that as the crack tip velocity increases, the stress intensity factors at the tip change, leading to instability and the potential for branching. The branching location relative to the crack tip is calculated. As the loading rate increases, the branching location moves closer to the crack tip due to increased stress concentration, which encourages branching closer to the crack tip (see Section 4.3.1.2).

To understand the dynamics of crack propagation and how fiber responds under different circumstances, we compare the fiber's calculated wave speeds with the observed crack tip speeds. For smaller crack lengths ($a = 0.4$ m), crack tip speeds generally range between the shear wave speed and the Rayleigh wave speed, occasionally exceeding the Rayleigh wave speed at higher loading rates but remaining below the dilatational wave speed. This indicates dynamic crack propagation. For larger crack lengths ($a = 0.6$ m), crack tip speeds are mostly below or close to the Rayleigh wave speed, sometimes even below the shear wave speed. The findings show that smaller cracks tend to have higher crack tip speeds, often exceeding the Rayleigh wave speed, while larger cracks exhibit lower speeds, typically below or near the Rayleigh wave speed. This confirms that increased crack length decreases crack tip speed (see Section 4.3.1.2).

Another crack mechanism involves arc cracks near the fiber surface, which can obstruct ion movement and affect diffusion. Arc cracks parallel to the fiber's outer surface are investigated during charging. Defined by the crack arc length $a(\rho, \theta)$, where ρ is the arc radius and θ is the arc angle, these cracks show a significant impact on diffusion. The maximum concentration difference in fibers with arc cracks is compared to those with center cracks and no cracks under identical conditions. The results show that surface-near arc cracks significantly affect diffusion by obstructing ion movement. Due to their proximity to the surface, lower charging rates can drive crack growth in arc cracks compared to center cracks. This

is because the radial and circumferential stresses at the tips of arc cracks are smaller in magnitude than those at the tips of center cracks (see Section 4.3.2).

Our research has practical implications for the design and performance of structural batteries. Crack tip speeds are calculated for tests conducted with three arc lengths and four loading conditions using a geometry-specific method (see Section 4.3.2). This comparison aimed to understand the general trends in crack tip behavior. The first observation is that higher ionic concentration loading rates increase crack tip speeds, likely due to the higher energy input accelerating crack propagation. Additionally, shorter crack lengths exhibit higher crack tip speeds, as shorter cracks have less surface area and lower resistance to propagation, resulting in faster crack tip speeds [64, 65]. Comparing concentration distribution before and after crack growth highlights the shielding effect of cracks on diffusion in the inner regions. The flux over the crack surfaces is zero, indicating that the crack acts as a barrier to diffusion. Consequently, the concentration remains zero on the inner side of the fiber even after the crack reaches the outer boundary. These findings underscore the importance of understanding crack behavior to improve the performance and reliability of structural batteries.

A third crack mechanism observed during the charging process is arc cracks forming from the ends of radial cracks. Radial cracks, caused by repeated intercalation and deintercalation cycles, were initially thought not to affect ion diffusion along radial pathways [33]. However, arc cracks, driven by high radial tensile stresses during initial intercalation stages, can propagate circumferentially from the tips of radial cracks [33]. This crack is called a T-crack in this thesis, defined with radial crack length b and arc crack defined by $a(\rho, \theta)$, where ρ is the radius of the arc crack, and θ is the arc angle (see Section 4.3.3).

The radial and circumferential stress fields are compared with radial cracks and T-cracks. In both configurations, the positions and sizes of the arc cracks are the same. The broader high tensile stress region in the case of the T-crack suggests a more extensive influence on the fiber's structural integrity, potentially leading to

different failure mechanisms compared to the arc crack. The stress concentrations around the arc crack may result in concentrated damage near the crack tips, while the T-crack may result in a more widespread weakening of the fibers. It is also worth noting that, in the case of the T-crack, the radial crack's presence almost eliminates compressive stress in the circumferential direction, allowing for expansion in that direction. The compressive stress values in the T-crack case are significantly lower than those in the arc crack case, especially near the surface region.

These observations indicate that T-cracks might create a higher tensile stress concentration in the fiber than arc cracks. Therefore, in the T-crack case, cracks could propagate more easily and in different directions, leading to various failure mechanisms under similar loading conditions. This is supported by comparing phase field distributions after crack growth (see Section 4.3.3). The T-crack propagates at an angle where these principal stresses facilitate the opening and sliding of the crack faces.

The proposed algorithm presents several strengths. One of its key strengths is introducing a two-way coupling approach for electrochemical loading. Unlike the common one-way coupling assumption in the literature [31], which often ignores the effect of mechanical stresses on diffusion due to typically slower diffusion rates compared to mechanical loads, this fully coupled system offers a more accurate prediction of fracture mechanisms, especially under faster diffusion rates.

The study has some limitations that need further attention. The charging rate range in the algorithm should be expanded to better handle slow diffusion cases. Additionally, crack propagation mechanisms during discharging need exploration in future research. The diffusive parameters of the phase field algorithm need further refinement, and results for different phase field parameters need to be reported. Future studies will address combined loading scenarios for macro models. Furthermore, incorporating nonlinear diffusion equations (described in Section 2.2.3), including both the solid electrolyte and matrix in the model, and examining

three-dimensional configurations will be essential. The pressure gradient is the higher-order term of the non-linear approach and is difficult to implement numerically. However, the reliability of the electro-chemo mechanical behavior solution can be improved by applying the methods suggested in the literature [54].

In conclusion, the findings of this thesis provide significant insights into the behavior and mechanisms of cracks in structural composite batteries. The investigation into stress distributions reveals that surface-near arc cracks significantly affect ion diffusion, acting as barriers and altering concentration profiles. Higher ionic concentration loading rates increase crack tip speeds, highlighting the impact of energy input on crack propagation. Additionally, shorter cracks exhibit higher crack tip speeds due to lower resistance to propagation. The analysis also demonstrates that radial and arc cracks, particularly T-cracks, play crucial roles in composite batteries' structural integrity and performance. Notably, the study of crack propagation for arc crack and T-crack geometries is a novel contribution to the literature, as previous studies only examined predefined crack geometries without showing actual propagation or propagation for the central crack geometry. These findings underscore the importance of understanding crack mechanisms and their effects on ion diffusion and mechanical stresses, offering critical guidance for improving the design and reliability of structural batteries. The in-depth knowledge of how cracks behave, as identified in this research, is crucial for improving the effectiveness and longevity of future energy storage systems.

REFERENCES

1. Xu, J. (2017). *Structural lithium-ion battery: Multiphysics modeling of mechanical and electrochemical phenomena* (Licentiate dissertation). Luleå University of Technology. Retrieved from

http://urn.kb.se/resolve?urn=urn:nbn:se:ltu:diva-63048

2. Hull, D., & Clyne, T. W. (1996). *An introduction to composite materials* (2nd ed.). Cambridge University Press. https://doi.org/10.1017/CBO9781139170130

3. Adam, T. J., et al. (2018). Multifunctional composites for future energy storage in aerospace structures. *Energies, 11*(2), Article 335. https://doi.org/10.3390/en11020335

4. Asp, L. E., & Greenhalgh, E. S. (2014). Structural power composites. *Composites Science and Technology, 101*, 41–61.

5. Kjell, M. H., Jacques, E., Zenkert, D., Behm, M., & Lindbergh, G. (2011). PAN-based carbon fiber negative electrodes for structural lithium-ion batteries. *Journal of The Electrochemical Society, 158*(12), A1455–A1460.

6. Sørensen, B. F. (2016). Delamination fractures in composite materials. In R. Talreja & J. Varna (Eds.), *Modeling damage, fatigue and failure of composite materials* (pp. 213–240). Woodhead Publishing. https://doi.org/10.1016/B978-1-78242-286-0.00011-X

7. Fazlali, B., Lomov, S. V., & Swolfs, Y. (2021). Fiber break model for tension-tension fatigue of unidirectional composites. *Composites Part B: Engineering, 220*, Article 108970. https://doi.org/10.1016/j.compositesb.2021.108970

8. Luo, H. A., & Chen, Y. (1991). Matrix cracking in fiber-reinforced composite materials. *ASME Journal of Applied Mechanics, 58*(3), 846–848.

https://doi.org/10.1115/1.2897274

9. Johnson, A., Hayes, S., & Jones, F. R. (2012). The role of matrix cracks and fibre/matrix debonding on the stress transfer between fibre and matrix in a single fibre fragmentation test. *Composites Part A: Applied Science and Manufacturing, 43*(1), 65–72. https://doi.org/10.1016/j.compositesa.2011.09.005

10. Greenhalgh, E. S. (Ed.). (2009). Chapter 7 - Defects and damage and their role in the failure of polymer composites. In *Failure analysis and fractography of polymer composites* (pp. 253–297). Woodhead Publishing.

11. Joffe, R. (1999). *Damage accumulation and stiffness degradation in composite laminates* (Doctoral thesis). Luleå University of Technology, Department of Engineering Sciences and Mathematics, Material Science.

12. Nairn, J. A. (2000). Matrix microcracking in composites. In R. Talreja & J. E. Manson (Eds.), *Polymer matrix composites* (Vol. 2, pp. 403–432). Elsevier.

13. Mehdikhani, M., Gorbatikh, L., Verpoest, I., & Lomov, S. V. (2019). Voids in fiber-reinforced polymer composites: A review on their formation, characteristics, and effects on mechanical performance. *Journal of Composite Materials, 53*(12), 1579–1669. https://doi.org/10.1177/0021998318772152

14. Chen, R., Bresser, D., Saraf, M., Gerlach, P., Balducci, A., Kunz, S., Schröder, D., Passerini, S., & Chen, J. (2020). A comparative review of electrolytes for organic-material-based energy-storage devices employing solid electrodes and redox fluids. *ChemSusChem, 13*(9), 2205–2219.

https://doi.org/10.1002/cssc.201903382

15. Ray, A., & Saruhan, B. (2021). Application of ionic liquids for batteries and supercapacitors. *Materials, 14*(11), Article 2942.

https://doi.org/10.3390/ma14112942

16. Zhou, D., Shanmukaraj, D., Tkacheva, A., Armand, M., & Wang, G. (2019). Polymer electrolytes for lithium-based batteries: Advances and prospects. *Chem, 5*(9), 2326–2352. https://doi.org/10.1016/j.chempr.2019.05.009

17. Ekstedt, S., Wysocki, M., & Asp, L. E. (2010). Structural batteries made from fibre reinforced composites. *Plastics, Rubber and Composites, 39*(3–5), 148–150. https://doi.org/10.1179/174328910X12647080902259

18. Ince, J. C., Peerzada, M., Mathews, L. D., & others. (2023). Overview of emerging hybrid and composite materials for space applications. *Advanced Composites and Hybrid Materials, 6*, Article 130. https://doi.org/10.1007/s42114-023-00678-5

19. Lim, G. J. H., Chan, K. K., Sutrisnoh, N. A. A., & Srinivasan, M. (2022). Design of structural batteries: Carbon fibers and alternative form factors. *Materials Today Sustainability, 20*, Article 100252.

https://doi.org/10.1016/j.mtsust.2022.100252

20. Asp, L., Bismarck, A., Lindbergh, G., Leijonmarck, S., Carlson, T., & Kjell, M. (2015). *Structural battery half cell, a structural battery and their manufacture* (Patent No. 2893582).

21. Leijonmarck, S., Carlson, T., Lindbergh, G., Asp, L. E., Maples, H., & Bismarck, A. (2013). Solid polymer electrolyte-coated carbon fibres for structural and novel micro batteries. *Composites Science and Technology, 89*, 149–157.

22. An, Q., Rider, A. N., & Thostenson, E. T. (2012). Electrophoretic deposition of carbon nanotubes onto carbon-fiber fabric for production of carbon/epoxy composites with improved mechanical properties. *Carbon, 50*(11), 4130–4143.

23. Carlstedt, D., Marklund, E., & Asp, L. E. (2019). Effects of state of charge on elastic properties of 3D structural battery composites. *Composites Science and Technology, 169*, 26–33. https://doi.org/10.1016/j.compscitech.2018.10.033

24. Carlstedt, D. (2019). *On the multifunctional performance of structural batteries* (Licentiate thesis). Chalmers University of Technology, Gothenburg, Sweden.

25. Donnet, J.-B., & Bansal, R. C. (1998). *Carbon fibers*. CRC Press.

26. Snyder, J., Gienger, E., & Wetzel, E. (2015). Performance metrics for structural composites with electrochemical multifunctionality. *Journal of Composite Materials, 49*(15), 1835–1848. https://doi.org/10.1177/0021998314568167

27. Jacques, E., Hellqvist Kjell, M., Zenkert, D., & Lindbergh, G. (2014). The effect of lithium-intercalation on the mechanical properties of carbon fibres. *Carbon, 68*, 725–733. https://doi.org/10.1016/j.carbon.2013.11.056

28. Snyder, J. F., Wetzel, E. D., & Watson, C. M. (2009). Improving multifunctional behavior in structural electrolytes through copolymerization of structure- and conductivity-promoting monomers. *Polymer, 50*(20), 4906–4916. https://doi.org/10.1016/j.polymer.2009.07.050

29. Zhang, H., Kulkarni, S., & Wunder, S. (2007). Blends of POSS−PEO(n=4)8 and high molecular weight poly (ethylene oxide) as solid polymer electrolytes for lithium batteries. *The Journal of Physical Chemistry B, 111*(13), 3583–3590. https://doi.org/10.1021/jp064585g

30. Asp, L. E. (2013). Multifunctional composite materials for energy storage in structural load paths. *Plastics, Rubber and Composites, 42*(4), 144–149. https://doi.org/10.1179/1743289811Y.0000000043

31. Xu, J., Lindbergh, G., & Varna, J. (2018). Multiphysics modeling of mechanical and electrochemical phenomena in structural composites for energy storage: Single carbon fiber micro-battery. *Journal of Reinforced Plastics and Composites, 37*(10), 701–715.

32. Carlson, T. (2013). *Multifunctional composite materials: Design, manufacture and experimental characterisation* (PhD dissertation). Luleå tekniska universitet. Retrieved from https://urn.kb.se/resolve?urn=urn:nbn:se:ltu:diva-26038

33. Pupurs, A., & Varna, J. (2013). Modeling mechanical stress and exfoliation damage in carbon fiber electrodes subjected to cyclic intercalation/deintercalation of lithium ions. *Composites Part B, 65*, 69–79.

34. Yang, Q. S., Qin, Q. H., Ma, L. H., & Cui, C. Q. (2010). A theoretical model and finite element formulation for coupled thermo-electro-mechanical media. *Mechanics of Materials, 42*, 148–156.

35. Klinsmann, M., Rosato, D., Kamlah, M., & McMeeking, R. (2015). Modeling crack growth during Li extraction in storage particles using a fracture phase field approach. *Journal of The Electrochemical Society, 163*(2), A102–A118.

https://doi.org/10.1149/2.0281602jes

36. Moyne, C., & Murad, M. A. (2002). Electro-chemo-mechanical coupling in swelling clays derived from a micro/macro-homogenization procedure. *International Journal of Solids and Structures, 39*(25), 6159–6190.

37. Li, S., Tian, L., & Cui, X. (2019). Phase field crack model with diffuse description for fracture problem and implementation in engineering applications. *Advances in Engineering Software, 129*, 44–56.

https://doi.org/10.1016/j.advengsoft.2018.09.005

38. Miehe, C., Hofacker, M., & Welschinger, F. (2010). A phase field model for rate-independent crack propagation: Robust algorithmic implementation based on operator splits. *Computer Methods in Applied Mechanics and Engineering, 199*(45-48), 2765–2778.

39. Waseem, S., Erdogan, C., & Yalçinkaya, T. (2024). Phase field modeling of fatigue crack growth retardation under single cycle overloads. *International Journal of Fatigue, 179*, Article 108064.

https://doi.org/10.1016/j.ijfatigue.2023.108064

40. Hirshikesh, S., Natarajan, R. K., Annabattula, R. K., & Martinez-Paneda, E. (2019). Phase field modelling of crack propagation in functionally graded materials. *Composites Part B: Engineering, 169*, 239–248.

41. Klinsmann, M., Rosato, D., Kamlah, M., & McMeeking, R. M. (2015). An assessment of the phase field formulation for crack growth. *Computer Methods in Applied Mechanics and Engineering, 294*, 313–330. https://doi.org/10.1016/j.cma.2015.06.009

42. Amor, H., Marigo, J. J., & Maurini, C. (2009). Regularized formulation of the variational brittle fracture with unilateral contact: Numerical experiments. *Journal of the Mechanics and Physics of Solids, 57*(8), 1209–1229.

43. Li, J., Lotfi, N., Landers, R., & Park, J. (2017). A single particle model for lithium-ion batteries with electrolyte and stress-enhanced diffusion physics. *Journal of The Electrochemical Society, 164*(4), A874–A883.

https://doi.org/10.1149/2.1541704jes

44. Amanieu, H.-Y., Rosato, D., Sebastiani, M., Massimi, F., & Lupascu, D. C. (2014). Mechanical property measurements of heterogeneous materials by selective nanoindentation: Application to $LiMn_2O_4$ cathode. *Materials Science and Engineering: A, 593*, 92–102.

45. Zhang, X., Shyy, W., & Sastry, A. M. (2007). Numerical simulation of intercalation induced stress in Li-ion battery electrode particles. *Journal of The Electrochemical Society, 154*(10), A910–A916. https://doi.org/10.1149/1.2759840

46. Christensen, J., & Newman, J. (2006). Stress generation and fracture in lithium insertion materials. *Journal of Solid State Electrochemistry, 10*(4), 293–319. https://doi.org/10.1007/s10008-006-0095-1

47. Tangella, R. G., Kumbhar, P., & Annabattula, R. K. (2022). Hybrid phase-field modeling of thermo-elastic crack propagation. *International Journal for Computational Methods in Engineering Science and Mechanics, 23*(1), 29–44. https://doi.org/10.1080/15502287.2021.1904462

48. Miehe, C., Welschinger, F., & Hofacker, M. (2010). Thermodynamically consistent phase field models of fracture: Variational principles and multi-field FE

implementations. *International Journal for Numerical Methods in Engineering, 83*(10), 1273–1311. https://doi.org/10.1002/nme.2861

49. Ambati, M., Gerasimov, T., & De Lorenzis, L. (2015). A review on phase-field models of brittle fracture and a new fast hybrid formulation. *Computational Mechanics, 55*(2), 383–405.

50. Torayev, A., Magusin, P. C. M. M., Grey, C. P., Merlet, C., & Franco, A. A. (2018). Importance of incorporating explicit 3D-resolved electrode mesostructures in Li–O_2 battery models. *ACS Applied Energy Materials, 1*(12), 6657–6667. https://doi.org/10.1021/acsaem.8b01392

51. Quintero-Cortes, F. J. (2022). *Engineering interfaces to control phase transformations in lithium-based battery components* (Doctoral dissertation). https://core.ac.uk/download/491307978.pdf

52. Pereira, T., Guo, Z., Nieh, S., Arias, J., & Hahn, H. (2008). Embedding thin-film lithium energy cells in structural composites. *Composites Science and Technology, 68*(7-8), 1935–1941.

https://doi.org/10.1016/j.compscitech.2008.02.019

53. Li, L., & Duan, Y. (2023). Engineering polymer-based porous membrane for sustainable lithium-ion battery separators. *Polymers, 15*(18), Article 3690. https://doi.org/10.3390/polym15183690

54. Dal, H., & Miehe, C. (2015). Computational electro-chemo-mechanics of lithium-ion battery electrodes at finite strains. *Computational Mechanics, 55*(2), 303–325. https://doi.org/10.1007/s00466-014-1102-5

55. Xu, J., & Varna, J. (2019). Matrix and interface microcracking in carbon fiber/polymer structural micro-battery. *Journal of Composite Materials, 53*(14), 1941–1953. https://doi.org/10.1177/0021998319843616

56. Xu, J., & Varna, J. (2019). Matrix and interface cracking in cross-ply composite structural battery under combined electrochemical and mechanical

loading. *Composites Science and Technology, 186*, Article 107891. https://doi.org/10.1016/j.compscitech.2019.107891

57. Klinsmann, M., Rosato, D., Kamlah, M., & McMeeking, R. M. (2016). Modeling crack growth during Li insertion in storage particles using a fracture phase field approach. *Journal of the Mechanics and Physics of Solids, 92*, 313–344.

58. Uyar, İ., & Gürses, E. (2024). Modeling of coupled behavior and microcracking of multifunctional composite structures for energy storage. *Procedia Structural Integrity*, 61, 195-205. https://doi.org/10.1016/j.prostr.2024.06.026

59. Gdoutos, E. E. (2003). Dilatational, shear, and Rayleigh wave speeds. In E. E. Gdoutos, C. A. Rodopoulos, & J. R. Yates (Eds.), *Problems of fracture mechanics and fatigue* (pp. 141–156). Springer. https://doi.org/10.1007/978-94-017-2774-7_81

60. Doyle, M., Fuller, T. F., & Newman, J. (1993). Modeling of galvanostatic charge and discharge of the lithium/polymer/insertion cell. *Journal of the Electrochemical Society, 140*(6), 1526–1533.

61. Alnæs, M. S., Blechta, J., Hake, J., Johansson, A., Kehlet, B., Logg, A., Richardson, C., Ring, J., Rognes, M. E., & Wells, G. N. (2015). The FEniCS Project Version 1.5. *Archive of Numerical Software, 3*(100), Article 20553. https://doi.org/10.11588/ans.2015.100.20553

62. Logg, A., Mardal, K.-A., & Wells, G. N. (2012). *Automated solution of differential equations by the finite element method*. Springer. https://doi.org/10.1007/978-3-642-23099-8

63. Bobaru, F., & Zhang, G. (2015). Why do cracks branch? A peridynamic investigation of dynamic brittle fracture. *International Journal of Fracture, 196* (1), 1–40. https://doi.org/10.1007/s10704-015-0056-8

64. Anderson, T. L. (2017). *Fracture mechanics: Fundamentals and applications* (4th ed.). CRC Press. https://doi.org/10.1201/9781315370293

65. Pistorio, F., Clerici, D., Mocera, F., & Somà, A. (2023). Review on the numerical modeling of fracture in active materials for lithium-ion batteries. *Journal of Power Sources, 566*, Article 232875.

https://doi.org/10.1016/j.jpowsour.2023.232875

66. Broek, D. (1986). *Elementary engineering fracture mechanics* (4th ed.). Kluwer Academic Publishers.

67. Irwin, G. R., & Wells, A. A. (1965). A continuum-mechanics view of crack propagation. *Metallurgical Reviews, 10*(1), 223–270.

https://doi.org/10.1179/mtlr.1965.10.1.223

68. Kotoul, M., & Vysloužil, T. (2009). Numerical modelling of crack propagation and R-curve behaviour in layered Al_2O_3/ZrO_2 composites. *Key Engineering Materials, 417-418*, 153–156.

69. Coker, D., & Rosakis, A. J. (2001). Experimental observations of intersonic crack growth in asymmetrically loaded unidirectional composite plates. *Philosophical Magazine A, 81*(3), 571–595.

https://doi.org/10.1080/01418610108212160

70. Denli, F. A., Gültekin, O., Holzapfel, G. A., & Dal, H. (2020). A phase-field model for fracture of unidirectional fiber-reinforced polymer matrix composites. *Computational Mechanics, 65*(5), 1149–1166. https://doi.org/10.1007/s00466-019-01812-1

71. Synge, J. L. (1956).Elastic waves in anisotropic media. *Journal of Mathematics and Physics, 35*(1), 323-334 https://doi.org/10.1002/sapm1956351323

72. Wong, E. L., Baechle, D. M., Xu, K., Carter, R. H., Snyder, J. F., & Wetzel, E. D. (2007). Design and processing of structural composite batteries. In *Proceedings of SAMPE 2007* (Baltimore, MD).

73. Foo, C. C., Guo, K., Srinivasan, B. M., Sridhar, N., Joshi, K., Su, Z., Zhang, G., & Fam, D. W. H. (2023). Multiphysics modelling of structural battery composites. *Composites Science and Technology*, Article 110178.

https://doi.org/10.1016/j.compscitech.2023.110178

74. Chen, G.-J.; Chung, W.-H. Evaluation of Charging Methods for Lithium-Ion Batteries. Electronics 2023, 12, 4095. https://doi.org/10.3390/electronics12194095

75. Licht, F., Davis, M. A., & Andreas, H. A. (2020). Charge redistribution and electrode history impact galvanostatic charging/discharging and associated figures of merit. *Journal of Power Sources, 446*, 227354.

https://doi.org/10.1016/j.jpowsour.2019.227354

76. Miehe, C., Dal, H., Schänzel, L.-M., & Raina, A. (2016). A phase-field model for chemo-mechanical induced fracture in lithium-ion battery electrode particles. *International Journal of Numerical Methods in Engineering*, 106(9), 683–711. https://doi.org/10.1002/nme.5133

77. Chen, J. H., & Cao, R. (2015). *Micromechanism of cleavage fracture of metals*. Elsevier.

APPENDICES

A. CRACK TIP SPEED CALCULATIONS

The definition of material wave speeds and formulation for an isotropic elastic material is given in this section.

Dilatational Wave Speed (Longitudinal or P-Wave Speed):

Dilatational waves, also known as primary (P) waves or longitudinal waves, are compression waves that cause particles in the material to move back and forth in the same direction as the wave is traveling. The speed V_p of dilatational waves in an isotropic elastic material is given by [59,71].

$$V_p = \sqrt{\frac{E(1-\nu)}{\rho(1+\nu)(1-2\nu)}} \tag{A-1}$$

where E is the Young's modulus, ν is the Poisson's ratio, and ρ is the density of the material.

Shear Wave Speed (Transverse or S-Wave Speed):

Shear waves, also known as secondary (S) waves or transverse waves, cause particles in the material to move perpendicular to the direction of wave propagation. If the crack tip speed is near or above the shear wave speed, the material may exhibit significant shear deformation around the crack tip.

The speed V_s of shear waves in an isotropic elastic material is given by [59, 71].

$$V_s = \sqrt{\frac{E}{2\rho(1+\nu)}} \tag{A-2}$$

Rayleigh Wave Speed:

Rayleigh waves are a type of surface wave that travel along the surface of a solid material at a speed slower than both P-waves and S-waves. They cause an elliptical

motion of particles near the surface. The Rayleigh wave speed is more complex to calculate as it involves solving an equation derived from the material's elastic constants. Crack tip speeds close to or exceeding the Rayleigh wave speed suggest that the crack propagates rapidly along the surface influenced by surface stress waves.

For an isotropic material, the Rayleigh wave speed V_R can be approximated as:

$$V_R \approx 0.87 + 1.12\nu \cdot V_S \tag{A-3}$$

The **critical crack tip speed** (denoted as v_c) represents a theoretical limit for the speed at which a crack can propagate in a material under certain conditions. Understanding this critical speed is essential in fracture mechanics and dynamic crack propagation analysis. When a crack propagates at this speed, it often results in specific dynamic phenomena such as increased stress intensity and potential for crack branching [69]. The simplified form for isotropic materials is

$$v_c = \sqrt{\frac{E}{\rho(1+\nu)}} == \sqrt{2}\, V_S \tag{A-4}$$

Dynamic crack propagation is the rapid advancement of a crack within a material, often due to sudden energy release or rapid loading conditions. It is characterized by significant stress concentrations at the crack tip, which drive the crack to propagate quickly. The crack speed can be comparable to the material's elastic wave speeds. As the crack propagates, it generates elastic waves that redistribute stress within the material, either accelerating or decelerating the crack growth. This rapid energy release can lead to complex crack paths, including branching, especially when the crack speed approaches the Rayleigh wave speed.

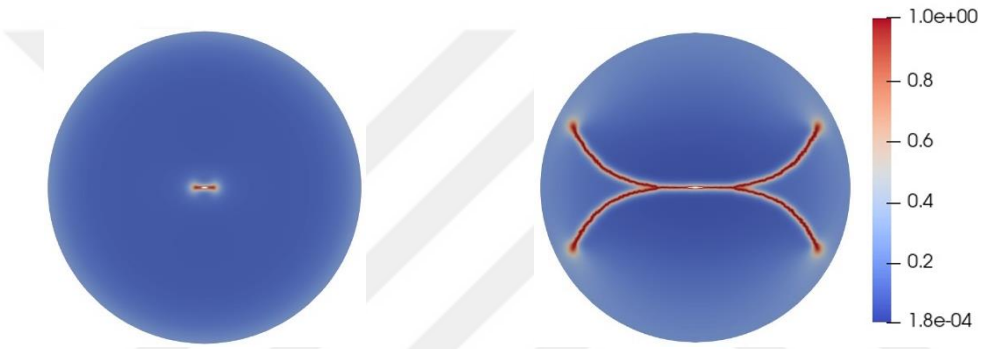
For the given material constants in Table 3.2, the wave speeds of the fiber are as follows: Dilatational (P-Wave) Speed (V_P): 4860.16 m/s, Shear (S-Wave) Speed (V_S): 2597.87 m/s, Rayleigh Wave Speed (V_R): 3133.03 m/s, and the critical crack tip speed v_c is 3675.52 m/s.

B. CRACK PROPAGATION RESULTS

Center Crack Results

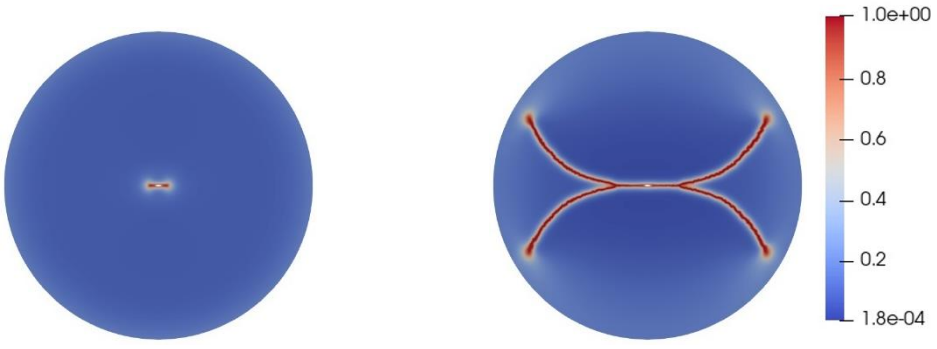
Phase field distributions during crack growth and propagation for the fiber with central cracks for the different test cases are listed below.

Test Case A* (a=0.1 m and $\dot{c} = 0.0008$ (mol/Ls)



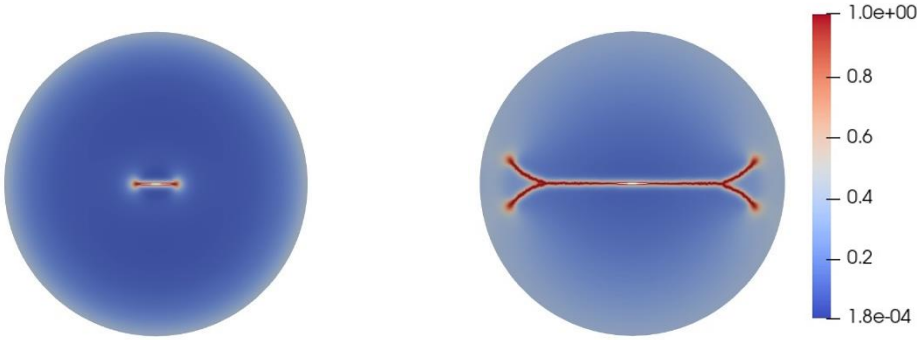
$t_n/\Delta t = 8$ $t_n/\Delta t = 9$

Test Case A4 (a=0.1 m and $\dot{c} = 0.001$ (mol/Ls)



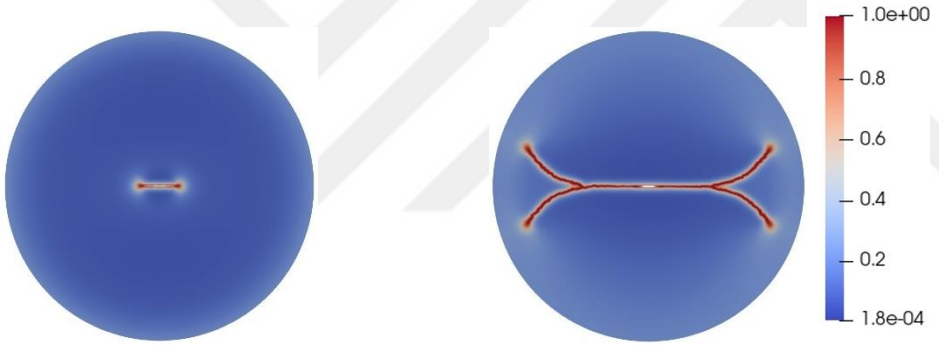
$t_n/\Delta t = 6$ $t_n/\Delta t = 7$

Test Case B2 (a=0.2 m and $\dot{c} = 0.0005$ (mol/Ls)



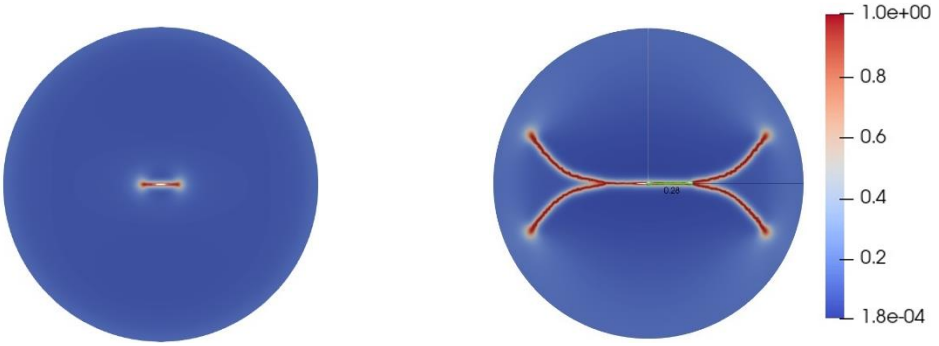
$t_n/\Delta t = 12$ $t_n/\Delta t = 13$

Test Case B3 (a=0.2 m and $\dot{c} = 0.0007$ (mol/Ls)



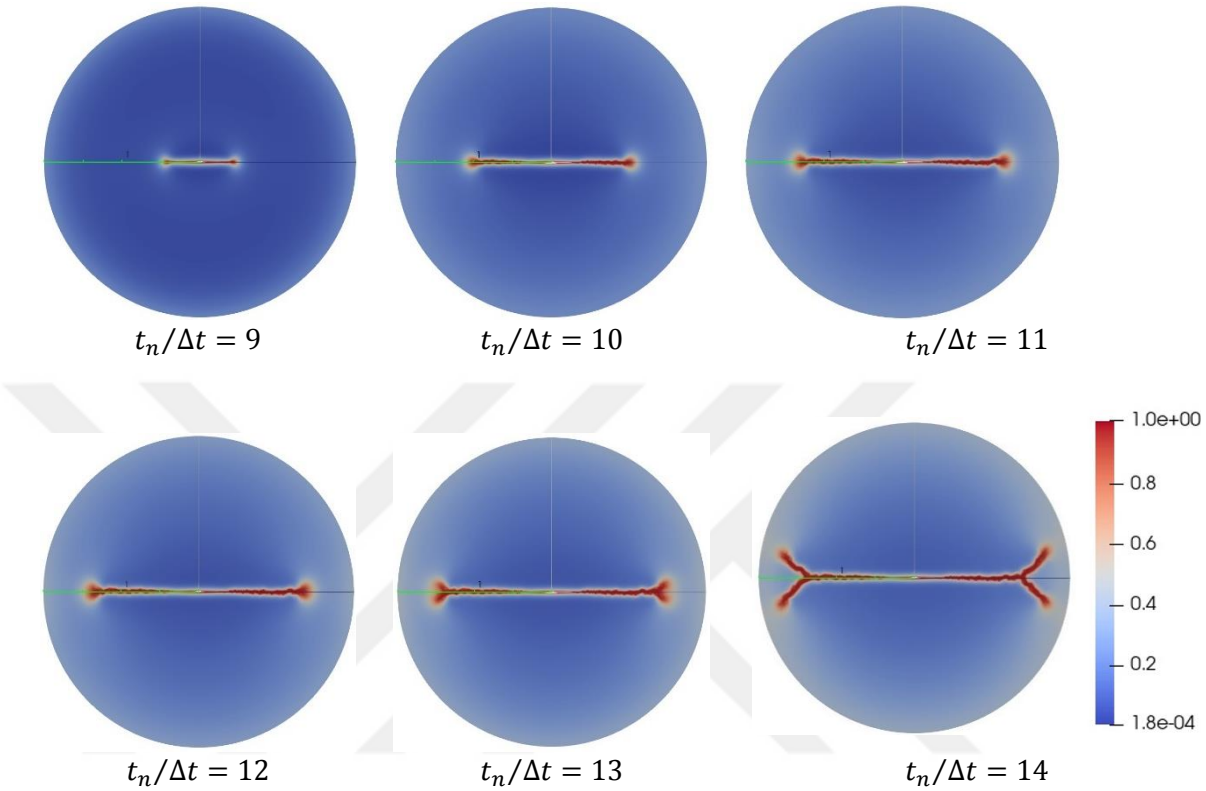
$t_n/\Delta t = 8$ $t_n/\Delta t = 9$

Test Case B4 (a=0.2 m and $\dot{c} = 0.001$ (mol/Ls)

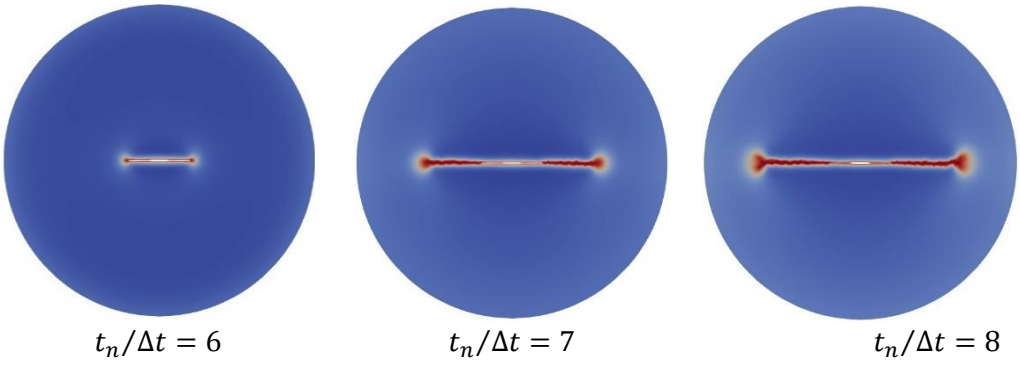


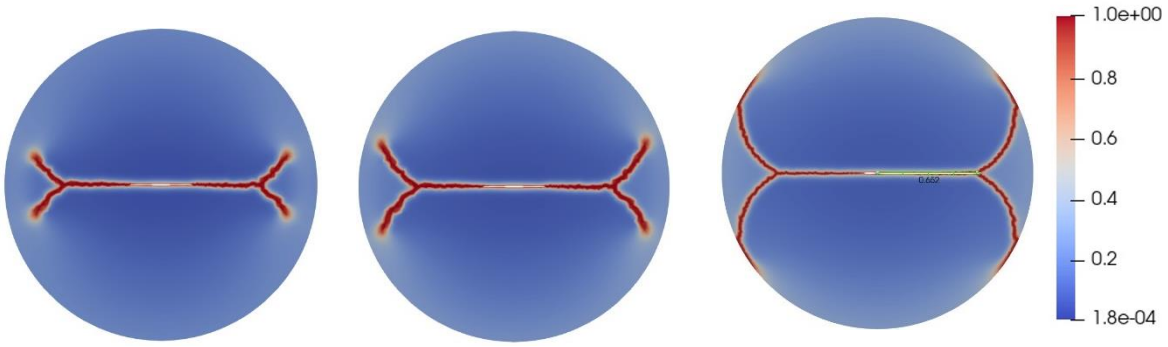
$t_n/\Delta t = 5$ $t_n/\Delta t = 6$

Test Case C2 (a=0.4 m and $\dot{c} = 0.0005$ (mol/Ls)



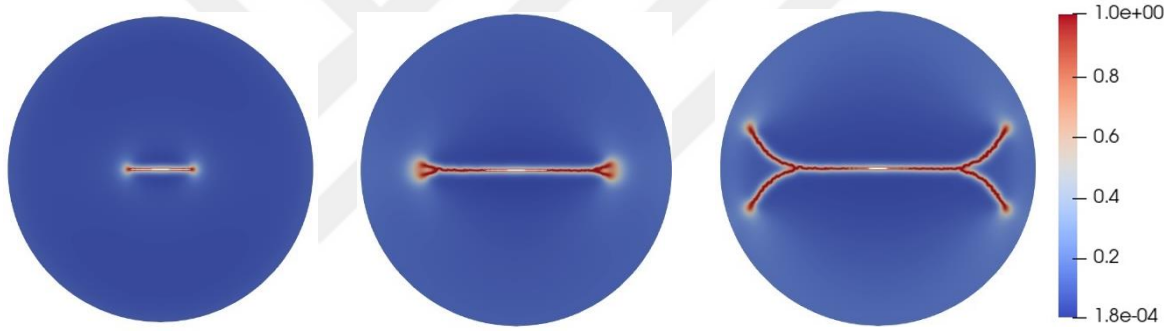
Test Case C3 (a=0.4 m and $\dot{c} = 0.0007$ (mol/Ls)





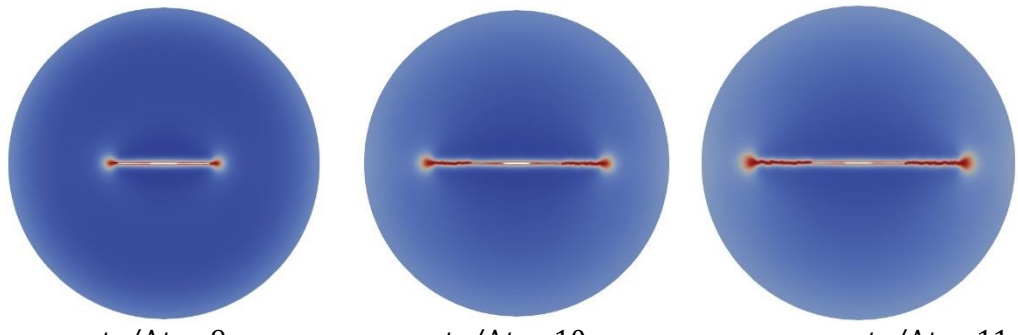
$t_n/\Delta t = 9$ $t_n/\Delta t = 10$ $t_n/\Delta t = 11$

Test Case C4 (a=0.4 m and $\dot{c} = 0.001$ (mol/Ls)

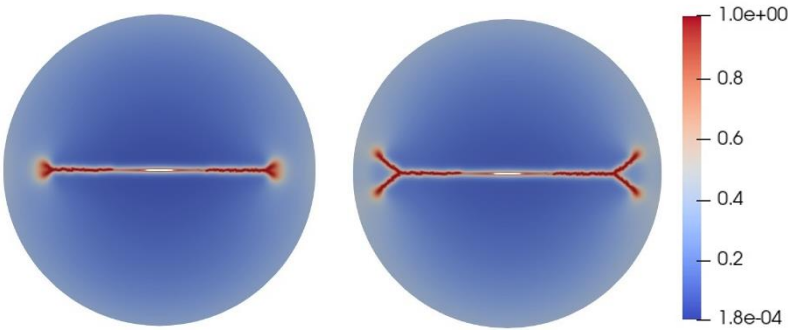


$t_n/\Delta t = 4$ $t_n/\Delta t = 5$ $t_n/\Delta t = 6$

Test Case D2 (a=0.6 m and $\dot{c} = 0.0005$ (mol/Ls)

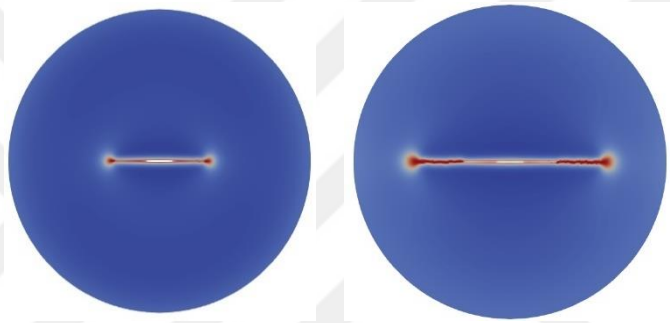


$t_n/\Delta t = 9$ $t_n/\Delta t = 10$ $t_n/\Delta t = 11$

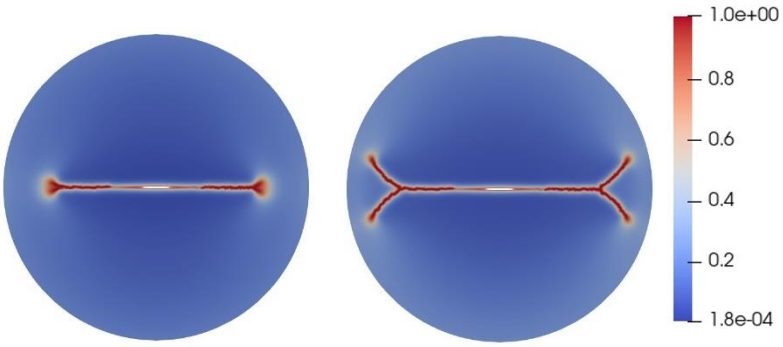


$t_n/\Delta t = 12$ $t_n/\Delta t = 13$

Test Case D3 (a=0.6 m and $\dot{c} = 0.0007$ (mol/Ls)

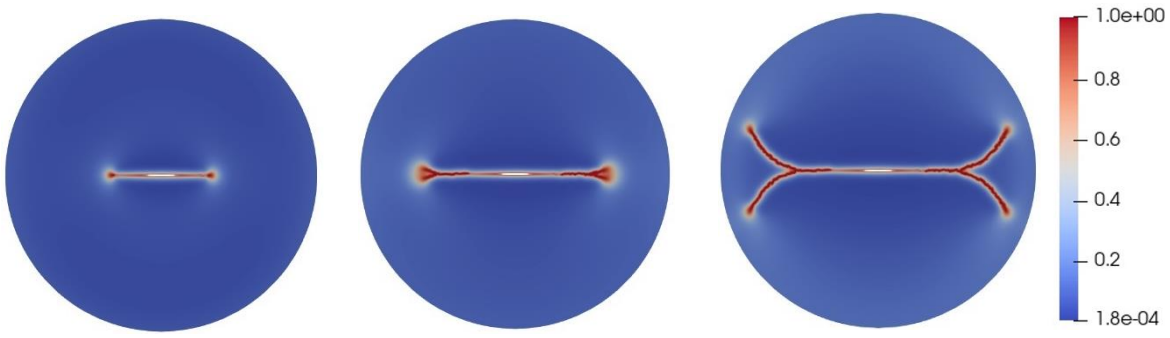


$t_n/\Delta t = 6$ $t_n/\Delta t = 7$



$t_n/\Delta t = 8$ $t_n/\Delta t = 9$

Test Case D4 (a=0.6 m and $\dot{c} = 0.001$ (mol/Ls)

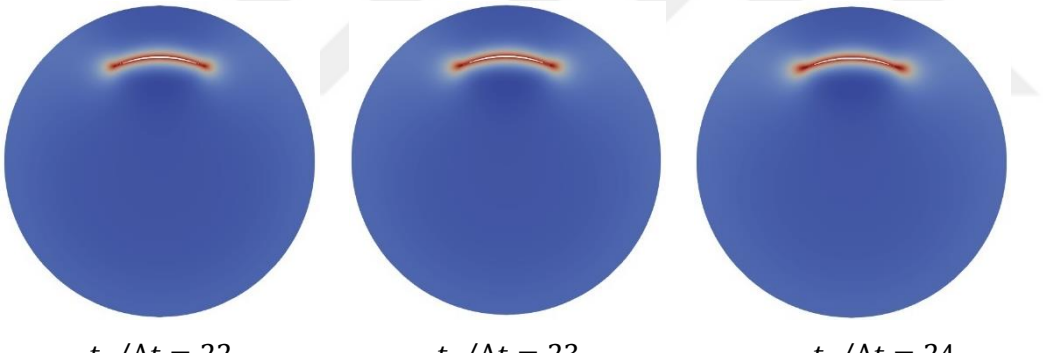


$t_n/\Delta t = 4$ $t_n/\Delta t = 5$ $t_n/\Delta t = 6$

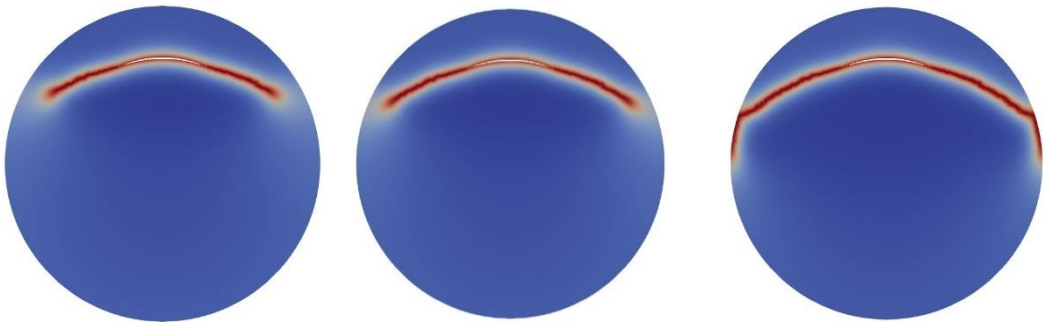
Arc Crack Results

Phase field distributions during crack growth and propagation for the fiber with arc cracks for the different test cases are listed below.

Test Case 1 ($\rho = 0.8$ m and $\theta = 50°$ and $\dot{c} = 0.0001$ (mol/Ls))

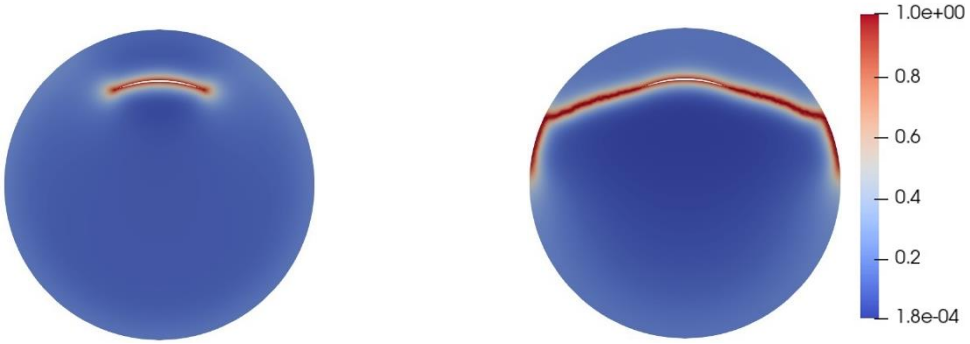


$t_n/\Delta t = 22$ $t_n/\Delta t = 23$ $t_n/\Delta t = 24$



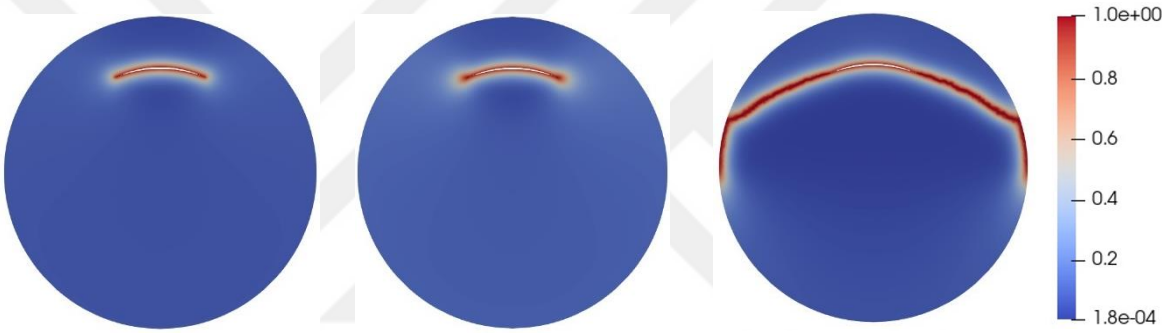
$t_n/\Delta t = 25$ $t_n/\Delta t = 26$ $t_n/\Delta t = 27$

Test Case 2 ($\rho = 0.8$ m and $\theta = 50°$ and $\dot{c} = 0.0003$ (mol/Ls))



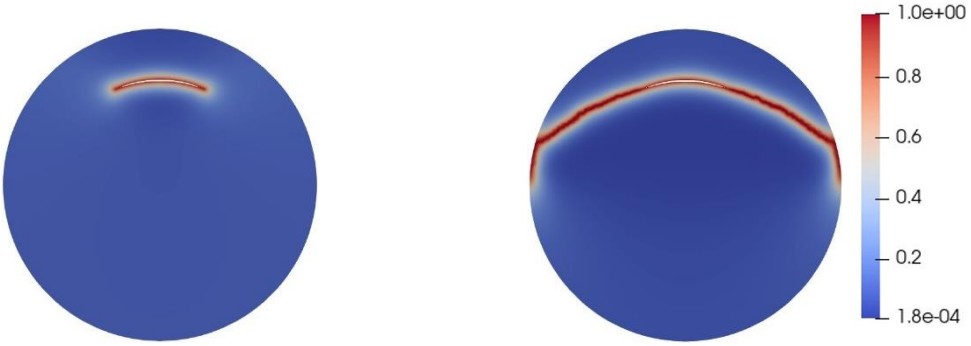
$t_n/\Delta t = 7$ $t_n/\Delta t = 8$

Test Case 3 ($\rho = 0.8$ m and $\theta = 50°$ and $\dot{c} = 0.0005$ (mol/Ls))



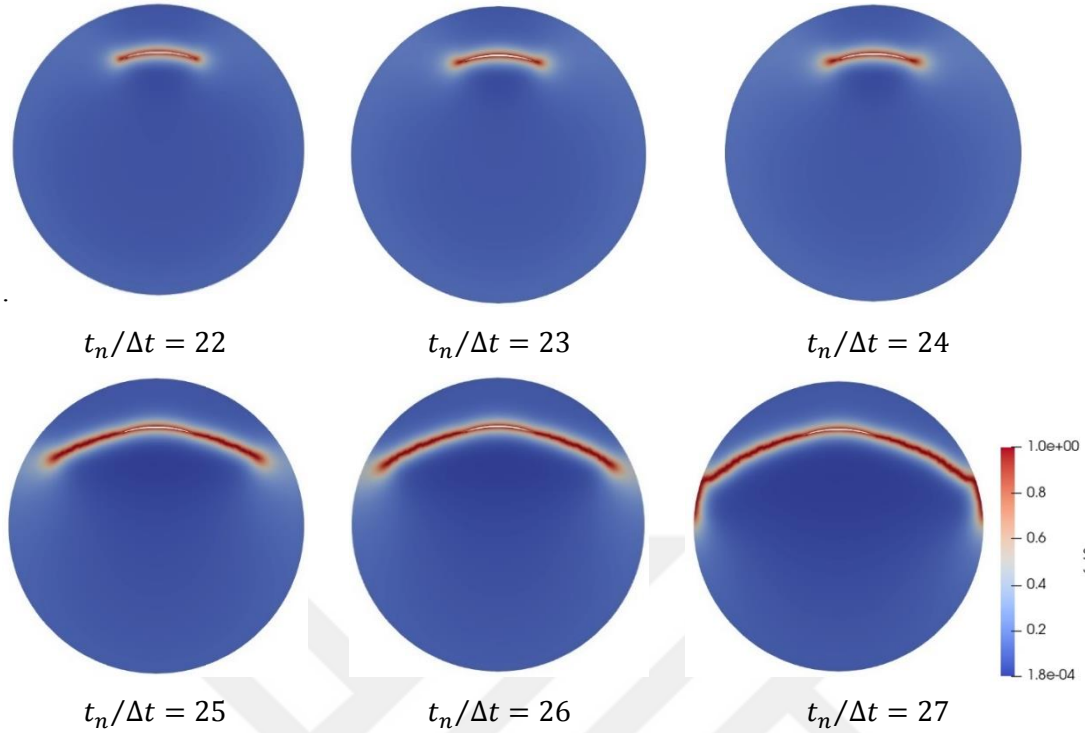
$t_n/\Delta t = 3$ $t_n/\Delta t = 4$ $t_n/\Delta t = 5$

Test Case 4 ($\rho = 0.8$ m and $\theta = 50°$ and $\dot{c} = 0.0007$ (mol/Ls))

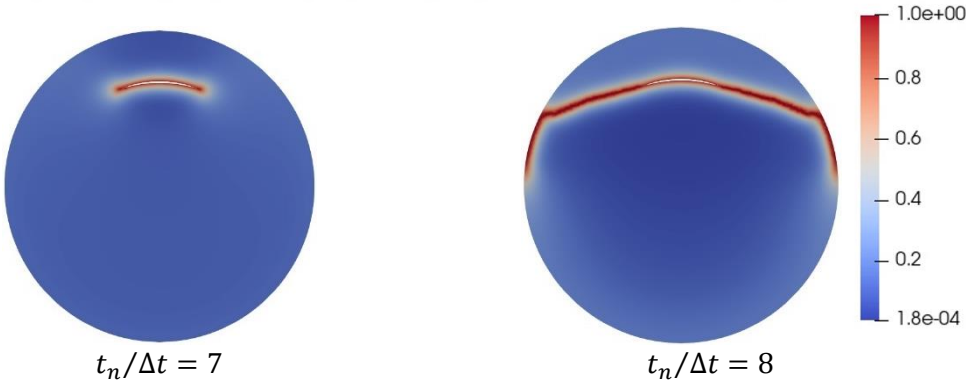


$t_n/\Delta t = 2$ $t_n/\Delta t = 3$

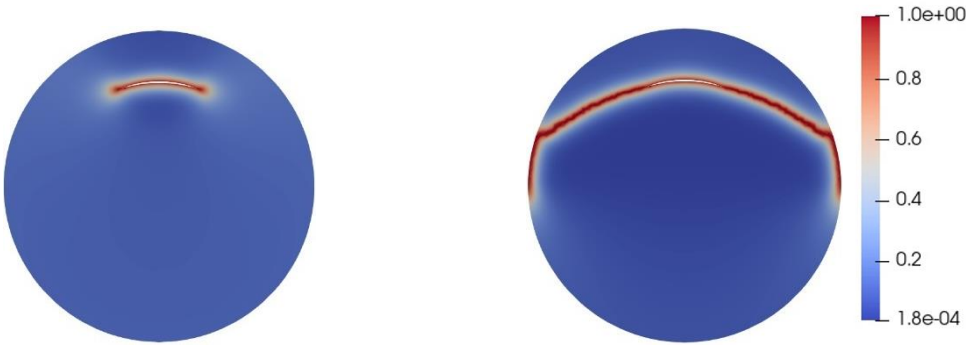
Test Case 5 ($\rho = 0.8$ m and $\theta = 45°$ and $\dot{c} = 0.0001$ (mol/Ls))



Test Case 6 ($\rho = 0.8$ m and $\theta = 45°$ and $\dot{c} = 0.0003$ (mol/Ls))

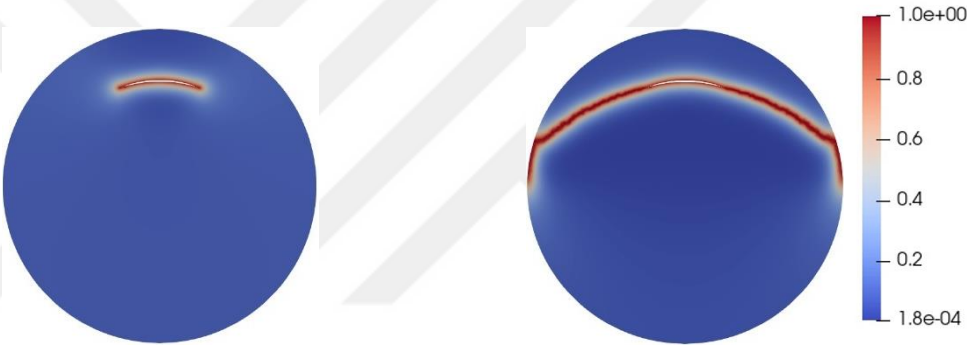


Test Case 7 ($\rho = 0.8$ m and $\theta = 45°$ and $\dot{c} = 0.0005$ (mol/Ls))



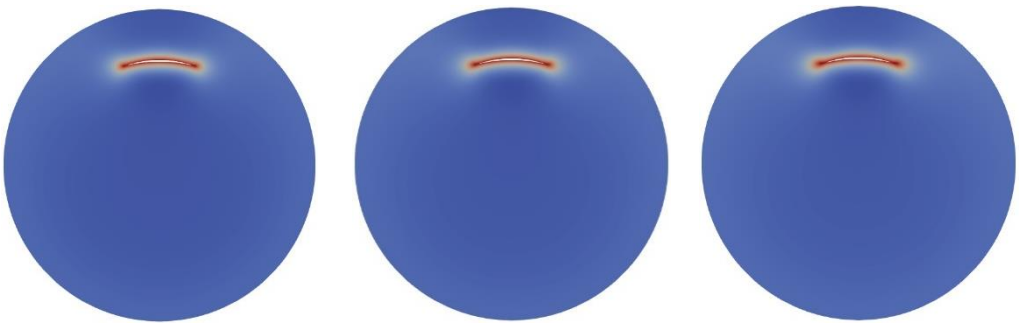
$t_n/\Delta t = 4$ $t_n/\Delta t = 5$

Test Case 8 ($\rho = 0.8$ m and $\theta = 45°$ and $\dot{c} = 0.0007$ (mol/Ls))

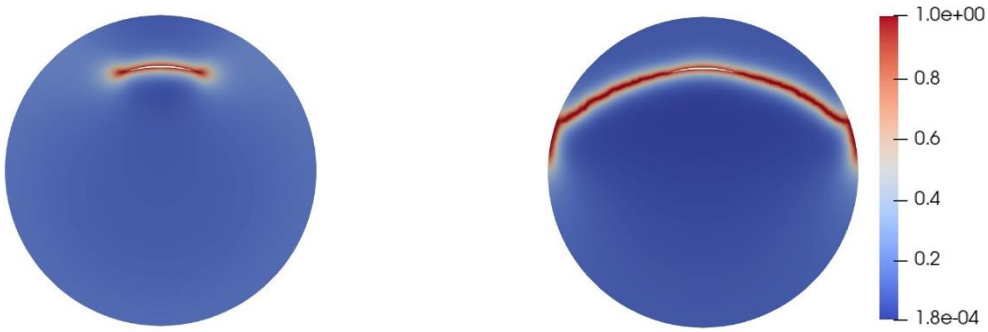


$t_n/\Delta t = 2$ $t_n/\Delta t = 3$

Test Case 9 ($\rho = 0.8$ m and $\theta = 40°$ and $\dot{c} = 0.0001$ (mol/Ls))

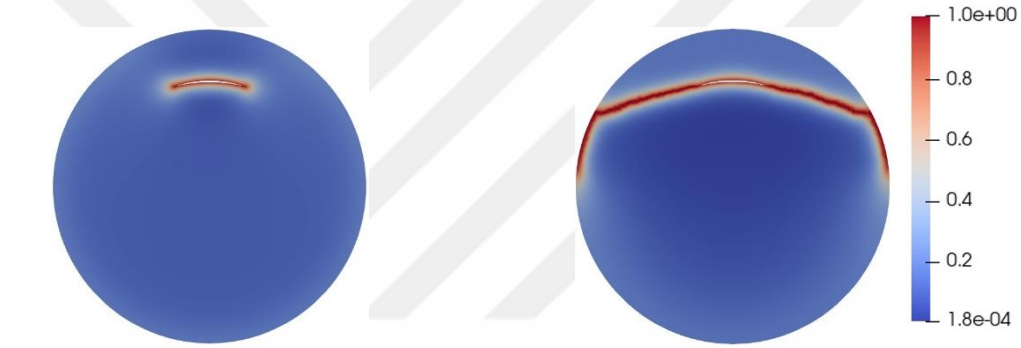


$t_n/\Delta t = 22$ $t_n/\Delta t = 23$ $t_n/\Delta t = 24$



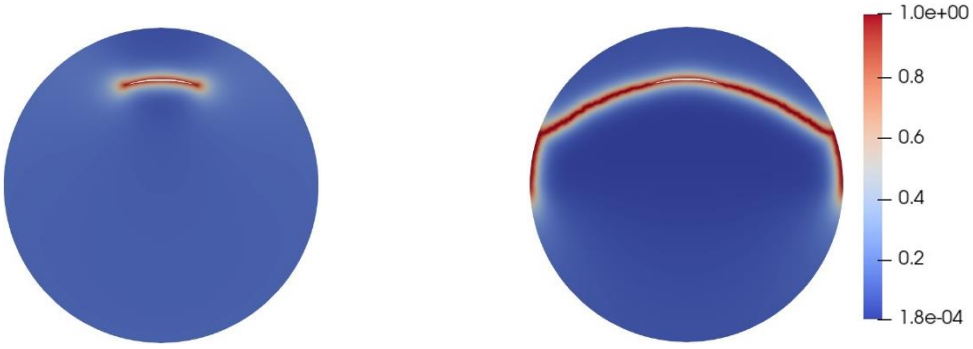
$t_n/\Delta t = 25$ $t_n/\Delta t = 26$

Test Case 10 ($\rho = 0.8$ m and $\theta = 40°$ and $\dot{c} = 0.0003$ (mol/Ls))



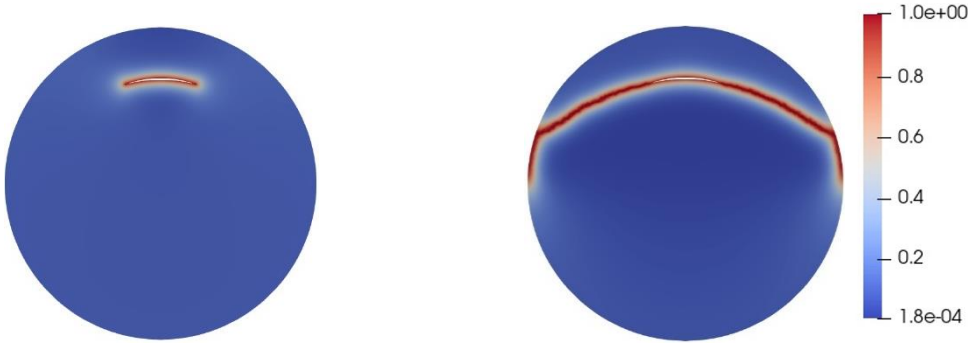
$t_n/\Delta t = 7$ $t_n/\Delta t = 8$

Test Case 11 ($\rho = 0.8$ m and $\theta = 40°$ and $\dot{c} = 0.0005$ (mol/Ls))



$t_n/\Delta t = 4$ $t_n/\Delta t = 5$

Test Case 12 ($\rho = 0.8$ m and $\theta = 40°$ and $\dot{c} = 0.0007$ (mol/Ls))

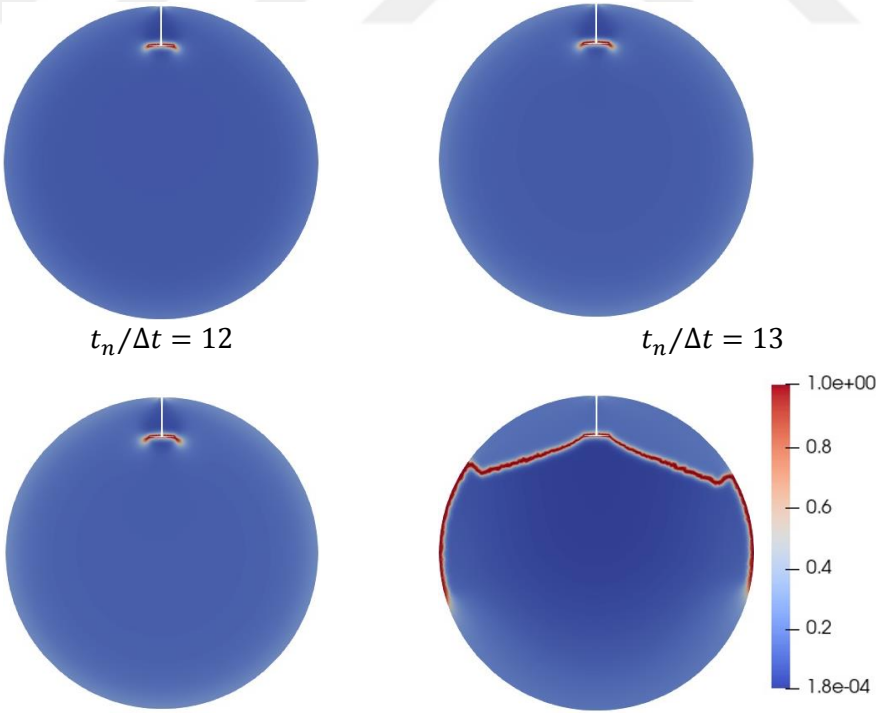


$t_n/\Delta t = 2$ $t_n/\Delta t = 3$

T- Crack Results

Below are the phase field distributions during crack growth and propagation for the fiber with T-cracks in the different test cases.

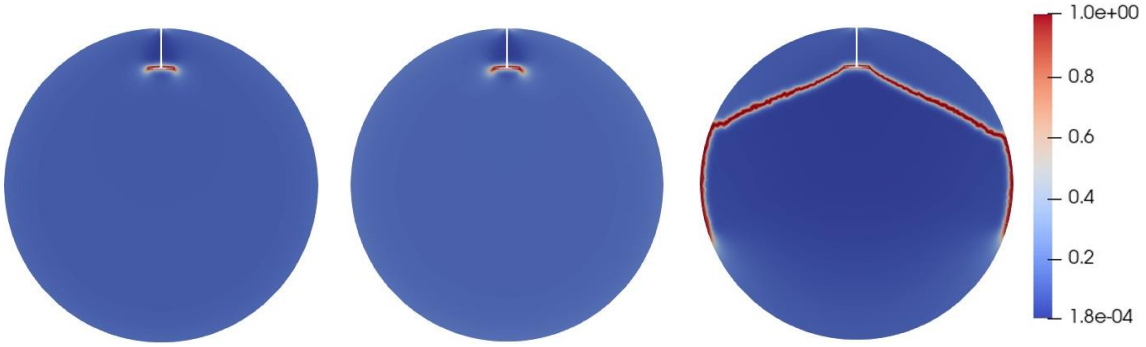
Test Case T1 ($\rho = 0.9$ m and $x_a = 0.20$ and $\dot{c} = 0.0003$ (mol/Ls))



$t_n/\Delta t = 12$ $t_n/\Delta t = 13$

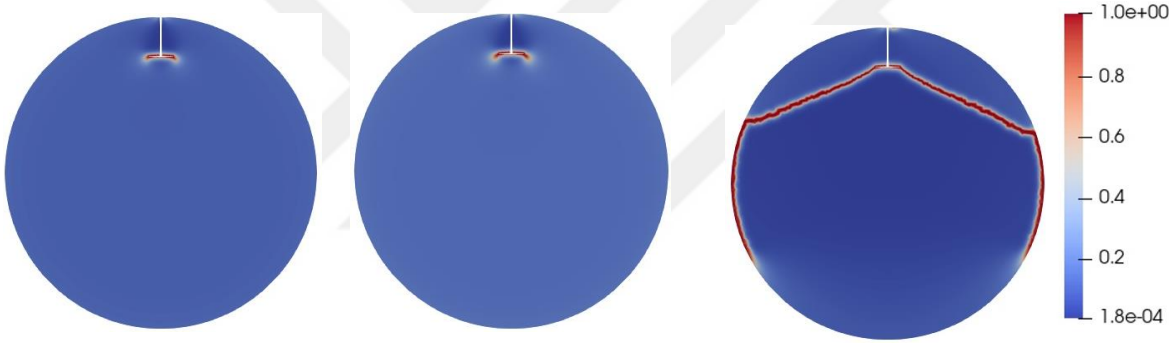
$t_n/\Delta t = 14$ $t_n/\Delta t = 15$

Test Case T2 ($\rho = 0.9$ m and $x_a = 0.20$ and $\dot{c} = 0.0005$ (mol/Ls))



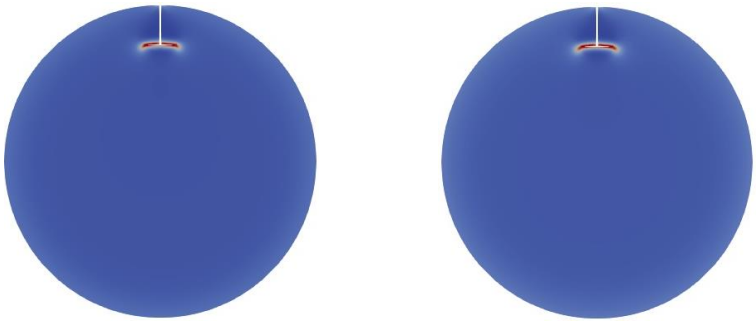
$t_n/\Delta t = 7$ $t_n/\Delta t = 8$ $t_n/\Delta t = 9$

Test Case T3 ($\rho = 0.9$ m and $x_a = 0.20$ and $\dot{c} = 0.0007$ (mol/Ls))

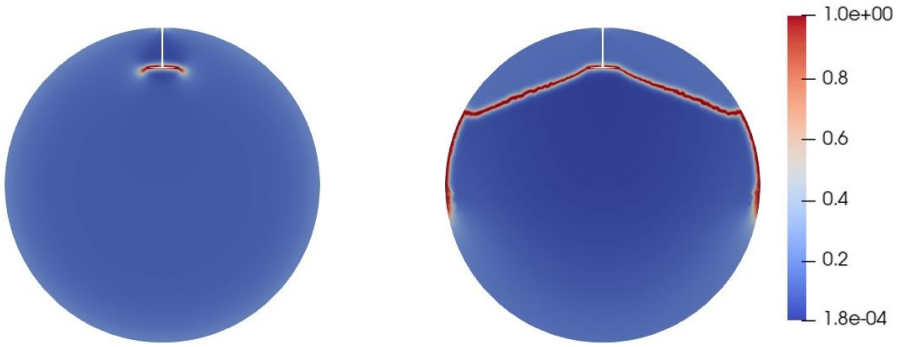


$t_n/\Delta t = 5$ $t_n/\Delta t = 6$ $t_n/\Delta t = 7$

Test Case T4 ($\rho = 0.9$ m and $x_a = 0.25$ and $\dot{c} = 0.0003$ (mol/Ls))

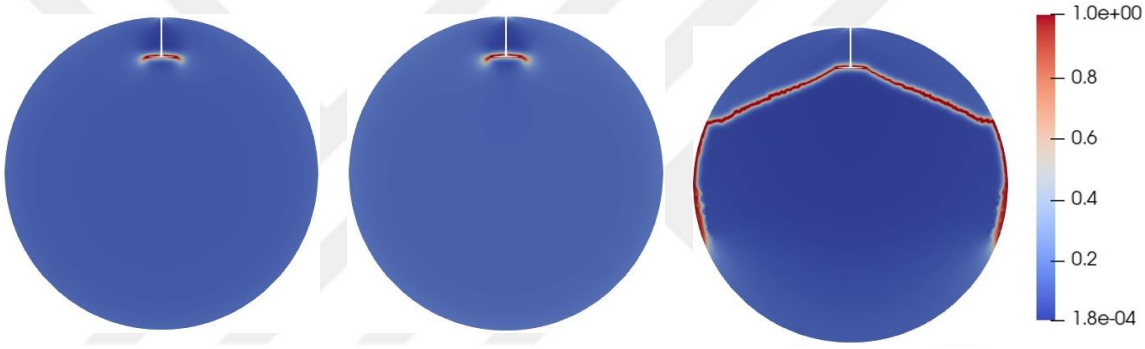


$t_n/\Delta t = 11$ $t_n/\Delta t = 12$



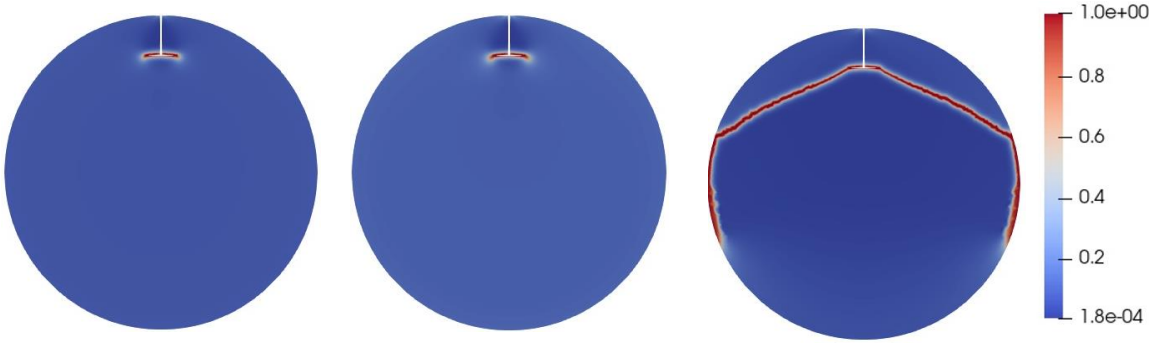
$t_n/\Delta t = 13$ $t_n/\Delta t = 14$

Test Case T5 ($\rho = 0.9$ m and $x_a = 0.25$ and $\dot{c} = 0.0005$ (mol/Ls))



$t_n/\Delta t = 5$ $t_n/\Delta t = 6$ $t_n/\Delta t = 7$

Test Case T6 ($\rho = 0.9$ m and $x_a = 0.25$ and $\dot{c} = 0.0007$ (mol/Ls))



$t_n/\Delta t = 4$ $t_n/\Delta t = 5$ $t_n/\Delta t = 6$

CURRICULUM VITAE

Surname, Name: Uyar Yazıcı, İmren

EDUCATION

Degree	Institution	Year of Graduation
MS	METU Aerospace Engineering	2014
BS	METU Aerospace Engineering	2011
High School	Güzelbahçe 60. Yil Anadolu Lisesi, İzmir	2006

FOREIGN LANGUAGES

English

PUBLICATIONS

Peer-reviewed journal articles

1. Gozluklu, B., Uyar, I., Coker, D., "Intersonic Delamination in Curved Thick Composite Laminates under Quasi-static loading", *Mechanics of Materials*, accepted, 2014. doi: 10.1016/j.mechmat.2014.07.013.

Peer-reviewed book chapters

1. Uyar, I. Arca, M. Gozluklu, B. Coker, D., "*Experimental Observations of Dynamic Delamination in Curved [0] and [0/90] Composite Laminates*", Fracture, Fatigue, Failure, and Damage Evolution, 5, Ed. G. Tandon, Conference Proceedings of the Society for Experimental Mechanics Series, doi: 10.1007/978-3-319-06992-0_22, pp. 189-196, 2015, Springer International Publishing.

2. Arca M. A., Uyar I, Coker D., **"***Experimental Investigation of the Effect of CNT Addition on the Strength of CFRP Curved Composite Beams***",** Composite, Hybrid and Multifunctional Materials, Volume 4, Ed. G. Tandon, Conference Proceedings

of the Society for Experimental Mechanics Series, doi: 10.1007/978-3-319-06992-0_22, pp. 177-184, 2015, Springer International Publishing.

3. Uyar, İ., & Gürses, E. (2024). Modeling of coupled behavior and microcracking of multifunctional composite structures for energy storage. *Procedia Structural Integrity*, 61, 195-205. https://doi.org/10.1016/j.prostr.2024.06.026

International conference presentations (*Presenter)

1. Coker, D., Gozluklu, B., **Uyar, I.***, Dynamic Delamination in Curved Composite Laminates under Quasi-static Loading, accepted by 2014 *The Science of Making Torque From Wind, Copenhagen, Denmark,* 18-20 June.

2. Uyar, I.*, Arca M., Coker, D., Experimental Observations of Dynamic Delamination Mechanisms in Curved Composite Beams, 2014 1st Mechanics of Composites Conference (MECHCOMP2014), Long Island, NY, June 8-12, 2014.

3. Uyar, I.*, Arca M., Coker, D., Experimental Observations of Delamination Mechanisms in Curved Composite Laminates, SEM Annual Conference and Exposition on Experimental and Applied Mechanics, Greenville, SC, USA, June 2-5, 2014.

4. Gozluklu, B*. Coker, D. Yavas, D. **Uyar, I**., "Effect of thickness and crack size on the dynamic delamination of L-shaped unidirectional composite laminates", Congress of American Society of Mechanical Engineers, ASME Paper No. IMECE2013-66597, San Diego, USA, 15-21 November, 2013.

5. Uyar, I., Arca M.,Yavas, D., Gozluklu, B., Coker,D.*, "Experimental investigation of delamination in L-shaped composite brackets", RUZGEM Conference on Wind Energy Science and Technology, Ankara, Turkey, 3-4 October, 2013.

6. **Uyar, I.*,** Arca M.,Yavas, D., Gozluklu, B., Coker, D., Experimental investigation of delamination in L-shaped composite brackets, SEM Annual Conference and Exposition on Experimental and Applied Mechanics, Lombard, IL, USA, June 3-5, 2013.

International conference proceedings

1. (Proceedings) Uyar, I. Gozluklu, B. Coker, D., "Dynamic delamination in curved composite laminates under quasi-static loading", *Journal of Physics: Conference Series*, 524, 2014. doi:10.1088/1742-6596/524/1/012042.

2. (Proceedings) Gozluklu, B.*, **Uyar, I.**, Coker, D., "Investigation of intersonic delamination in highly curved composite laminates under quasi-static loading", *11th World Congress of Computational Mechanics (WCCM),* Barcelona, Spain, 20-25 July, 2014.

3. (Proceedings) **Uyar, I**., Arca M.,Yavas, D., Gozluklu, B., Coker,D.*, "Experimental investigation of delamination in L-shaped composite brackets", RUZGEM Conference on Wind Energy Science and Technology, Ankara, Turkey, 3-4 October, 2013.

4. (Proceedings) Yavas, D*. Uyar, I. Gozluklu, B. Coker, D., "Experimental and Computational Investigation of Debonding at the Interface of Two L-Shaped PMMA Beams", Congress of American Society of Mechanical Engineers, ASME Paper No. IMECE2012-88425, Houston, USA, 9-15 November, 2012.

National conference proceedings and presentations

1. Uyar, I., Arca M.* Çöker, D., Bükümlü [0] ve [0/90] Kompozit Laminatlarda Dinamik Delaminasyonun Deneysel Araştırılması, V. Ulusal Havacilik Ve Uzay Konferansi 8-10 Eylül 2014, Erciyes Üniversitesi, Kayseri.

2. Uyar İ.*,Gözlüklü B., Arca M. A., Çöker D., Bükümlü Kalın Kompozit Laminatlarda Dinamik Delaminasyon Olayının İncelenmesi, SAVTEK 2014, 7. Savunma Teknolojileri Kongresi, 25-27 Haziran, Ankara.